REVIEW ARTICLE

Check for updates

Carbon capture and conversion using metal–organic frameworks and MOF-based materials

Meili Ding,†[a] Robinson W. Flaig,†[b] Hai-Long Jiang [iD] *[a] and Omar M. Yaghi [iD] *[bc]

Rapidly increasing atmospheric CO_2 concentrations threaten human society, the natural environment, and the synergy between the two. In order to ameliorate the CO_2 problem, carbon capture and conversion techniques have been proposed. Metal–organic framework (MOF)-based materials, a relatively new class of porous materials with unique structural features, high surface areas, chemical tunability and stability, have been extensively studied with respect to their applicability to such techniques. Recently, it has become apparent that the CO_2 capture capabilities of MOF-based materials significantly boost their potential toward CO_2 conversion. Furthermore, MOF-based materials' well-defined structures greatly facilitate the understanding of structure–property relationships and their roles in CO_2 capture and conversion. In this review, we provide a comprehensive account of significant progress in the design and synthesis of MOF-based materials, including MOFs, MOF composites and MOF derivatives, and their application to carbon capture and conversion. Special emphases on the relationships between CO_2 capture capacities of MOF-based materials and their catalytic CO_2 conversion performances are discussed.

[a] *Hefei National Laboratory for Physical Sciences at the Microscale, CAS Key Laboratory of Soft Matter Chemistry, Collaborative Innovation Center of Suzhou Nano Science and Technology, Department of Chemistry, University of Science and Technology of China, Hefei, Anhui 230026, P. R. China. E-mail: jianglab@ustc.edu.cn*

[b] *Department of Chemistry, University of California-Berkeley, Materials Sciences Division, Lawrence Berkeley National Laboratory, Kavli Energy NanoSciences Institute, Berkeley, California, 94720, USA. E-mail: yaghi@berkeley.edu*

[c] *UC Berkeley-KACST Joint Center of Excellence for Nanomaterials for Clean Energy Applications, King Abdulaziz City for Science and Technology, Riyadh 11442, Saudi Arabia*

† These authors contributed equally to this work.

1. Introduction

Energy demands of the global society are being met largely by combustion of fossil fuels including coal, petroleum, and natural gas. A major greenhouse gas (GHG), carbon dioxide (CO_2) is a key by-product of such combustion. The immense quantity of CO_2 emissions has resulted in serious environmental issues, such as global warming, ocean acidification, extreme weather, and species extinction.[1,2] Since the early 19th century, a steep and continuous increase has been observed in atmospheric CO_2 concentrations from approximately 280 ppm in the early 1800s to over 400 ppm in 2018. With little to no mitigative action, the Intergovernmental Panel on Climate Change (IPCC) has predicted that atmospheric

Meili Ding received her BS degree (2014) in chemistry from Anhui Normal University. She is currently a PhD student under the guidance of Prof. Hai-Long Jiang at University of Science and Technology of China (USTC). Her research focuses on metal–organic framework-based materials for CO_2 capture and conversion.
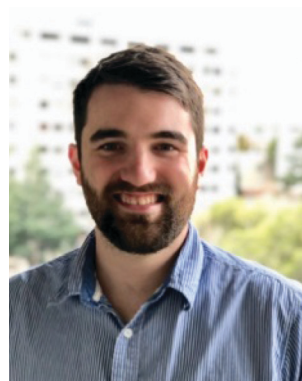
Meili Ding

Robinson W. Flaig received his BS degree (2014) in chemistry from UW-Platteville. He is currently a PhD student under the guidance of Prof. Omar Yaghi at UC Berkeley. His research focuses on the development of new MOFs and COFs for CO_2 capture and mechanistic studies of CO_2 chemisorption reactions.

Robinson W. Flaig

CO_2 concentrations could reach 950 ppm by 2100.[3–5] Elevated atmospheric CO_2 levels serve to directly increase the global mean temperature (around 1.9 °C at atmospheric CO_2 concentrations of 570 ppm) by absorbing outgoing longwave radiation (*i.e.* the greenhouse effect).[3] Therefore, decreasing emissions and mitigating atmospheric CO_2 concentrations are imperative tasks that require drastic, immediate attention. With the understanding that fossil fuels will remain a major source of energy for the foreseeable future, the most straightforward strategy to reduce anthropogenic CO_2 emissions lies in removing CO_2 from point sources, such as the flue gas from fossil-fuel burning power plants. This can be accomplished using suitable carbon capture and storage (CCS) technologies. Key drawbacks in such technologies lie in the energy consumption associated with separation, purification, compression, transportation, and storage processes.[6] This consumption is likely to be accompanied by further CO_2 emission, and thus will not adequately address the issue. Moreover, various adsorbents have been developed in order to capture and store CO_2, but their high regeneration temperatures and/or limited CO_2 adsorption capacities still hinder the development of CCS technologies.[2,6,7] Beyond CCS, another strategy involves capture and subsequent conversion of CO_2 into high value-added chemicals and fuels (*i.e.* CO_2 capture and conversion). In doing so, CO_2 capture and conversion serves as an anthropogenic carbon cycle, is more sustainable, and thus lies further within the realm of ''green chemistry''.

In the past decades, several classes of materials, including ionic liquids (ILs), zeolites, porous carbons, porous organic polymers, covalent organic frameworks (COFs) and metal–organic frameworks (MOFs), have been developed for CO_2 capture and conversion applications.[8–16] In particular, MOFs signify a relatively new class of crystalline porous materials constructed from multimetallic units called secondary building units (SBUs) and organic linkers.[17–21] By designing and functionalizing SBUs, linkers and pore environments, MOFs' physical and chemical properties can be finely tuned, making them promising materials for a variety of applications, such as gas storage and separation, heterogeneous catalysis, sensing, drug delivery, to mention a few.[14–19,22–92] With respect to CO_2 capture and conversion, MOFs serve as promising adsorbents and catalysts because of their unique advantages: (1) predicable, functionalizable structures; it is possible to predict the structures of many MOFs and the structural designability and chemical tunability of the materials allow for incorporation of different types of accessible capture and catalytically active sites. (2) Hybrid structures; MOFs are highly compatible with other materials and can serve as precursors and/or templates to afford MOF composites or MOF derivatives with extraordinary physical and chemical properties. (3) Particular strengths for catalysis; MOFs combine beneficial features of homogeneous and heterogeneous catalysts, such as high catalytic efficiency, facile separation and reusability, and stability. (4) The well-defined and tailorable structures of MOFs greatly facilitate the understanding of structure–property relationships in MOF-based catalysts. All of these attributes make MOFs ideally suited for CO_2 capture and conversion.

The employment of MOFs in CO_2 capture and conversion applications has undergone three development stages. First, the CO_2 adsorption capacity and selectivity of MOFs were tuned.[15,47,62,75,78–80] Toward this end, a variety of strategies have been investigated in order to enhance MOF–CO_2 interactions. As many MOFs exhibiting strong interactions with CO_2 were developed, they began to garner immense attention with respect to CO_2 separation applications, mainly regarding the removal of CO_2 from CO_2/H_2 (pre-combustion carbon capture) and CO_2/CH_4 gas mixtures (natural gas purification), as well as CO_2 capture from CO_2/N_2 gas mixtures (post-combustion carbon capture).[15,62,75,77,80] The second stage focused on development

Hai-Long Jiang received his PhD (2008) from Fujian Institute of Research on the Structure of Matter, CAS. He subsequently worked at the National Institute of Advanced Industrial Science and Technology (AIST, Japan), first as an AIST Fellow and later as a JSPS Fellow during 2008–2011. After a postdoctoral stint at Texas A&M University (USA), he was appointed as a full professor at USTC in 2013. He is a Fellow of the Royal Society of

Hai-Long Jiang

Chemistry (FRSC) and was recognized as a highly cited researcher (2017 & 2018) in chemistry by Clarivate Analytics. His main research interest is the development of crystalline porous and nanostructured materials, crossing coordination chemistry and nanoscience, for catalysis.

Omar M. Yaghi received his PhD from the University of Illinois-Urbana, and studied as an NSF Postdoctoral Fellow at Harvard University. He is currently the James and Neeltje Tretter Chair Professor of Chemistry at UC Berkeley and a Senior Faculty Scientist at Lawrence Berkeley National Laboratory. He is also the Founding Director of the Berkeley Global Science Institute as well as the Co-Director of the Kavli Energy NanoScience

Omar M. Yaghi

Institute and the California Research Alliance by BASF. He is interested in the science of building chemical structures from organic and inorganic molecular building blocks (Reticular Chemistry) to make extended porous structures, such as MOFs, COFs, and ZIFs.

2784 | *Chem. Soc. Rev.*, 2019, **48**, 2783–2828

This journal is © The Royal Society of Chemistry 2019

of MOF-based materials and their use for the conversion of CO_2 to organic products. Particularly, CO_2 cycloaddition with epoxides has become one of the most intensively investigated MOF-catalyzed CO_2 conversion reactions.[65–68] It is important to recognize that many MOFs have a limited variety of reactive sites, with the major examples being acidic and/or basic sites on the SBU metal centers and/or the organic linkers. With this in mind, MOF composites made by combining MOFs with other materials, and MOF derivatives afforded by chemical and/or thermal conversion of MOFs with multiple active sites and high stabilities have emerged as promising materials for CO_2 capture and separation.[74,82–85] In the third and most recent stage, attempts have been made to explore and expand the scope of possible CO_2 transformation reactions involving MOF-based materials. Additionally, optimization of the catalytic performance of such materials for practical CO_2 capture and conversion has become the main target. On the basis of their unique features, particularly stability and conductivity, and cooperativity between multiple active sites, MOF-based materials can serve as highly effective catalysts for numerous value-added CO_2 conversion reactions, specifically photocatalytic and electrocatalytic CO_2 reduction.[52,63,70,86–88,90,92] With these stages in mind, current and future development promise to target optimization of the synergistic effects of CO_2 adsorption and CO_2 conversion in MOFs and MOF-based materials. Although many challenges remain, the so-called "Holy Grail" of MOF application to carbon capture and conversion technologies lies in the development of a material that can capture CO_2 from a gas mixture such as flue gas and directly, catalytically convert it to value-added compounds.

In pursuit of this lofty goal, it is crucial to have a detailed and comprehensive overview of the work that has already been reported. Thus, herein we present a summary and assessment of the development of MOF-based materials for CO_2 capture and conversion as illustrated in Scheme 1 for a generic MOF. We start by providing an overview of the CO_2 capture strategies employed in MOFs with specific focus placed on interactions between the frameworks and CO_2. Additionally, the challenges and targets intrinsic to the development of MOFs for CO_2 capture are discussed. Next, recent advances in the field of MOF-based materials for CO_2 conversion, including heterogeneous transformation into organic products, hydrogenation, photocatalytic reduction, and electrocatalytic reduction, are comprehensively described. Thirdly, we provide insight into the relationship between CO_2 capture capacity of MOF-based materials and their catalytic CO_2 conversion performance. Finally, the existing challenges and future directions in this research field are highlighted.

2. MOFs for CO_2 capture

Since their inception over 20 years ago,[93,94] MOFs have been targeted for CO_2 adsorption and capture applications due to their high porosity and chemical tunability.[95] To date, many reports focus on the study of CO_2 capture and increasing the capacity in
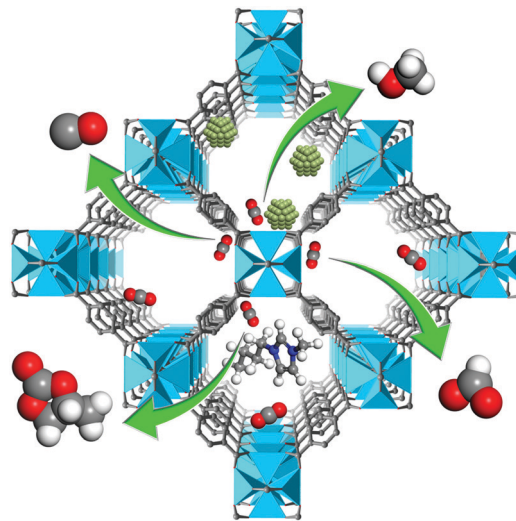
Scheme 1 An illustration of a generic MOF, composed of tetrametallic SBUs (cyan polyhedra) linked together by terephthalate (gray), with four channels shown to capture CO_2 and convert it to either CO (left), methanol using metal nanoparticles embedded in the pore (top), formate (right), or ethylene carbonate using an ionic liquid lodged in the pore (bottom).

MOFs as shown in Table 1. Generally, the interaction(s) between the framework and CO_2 adsorbate molecules play a critical role, as increasing the strength of such interactions augments the material's CO_2 uptake capacity, especially at low loading pressure. The methods employed to increase these interaction strengths stem from tailoring the frameworks' chemical and physical properties. This relies on the ability to alter the intrinsic properties of MOFs based on judicious design and synthesis of the framework *via de novo* processes or by post-synthetic modification. In each case, the goal is to leverage MOFs' chemical tunabilities and compatibilities to adjust the affinity of the framework for CO_2 molecules. Post-synthetic modification has been widely applied recently as a means of achieving this adjustment with a high degree of precision. In this section, we will explain each strategy in detail and provide examples of their employment.

2.1. CO_2 binding sites within MOFs

Traditional adsorbent materials including zeolites, silicas, polymers, activated carbons, take up CO_2 in a physisorptive manner through the use of weak interactions between CO_2 and the pore. Although MOFs also capture CO_2 by physisorption, their ultrahigh surface areas give much higher uptake capacities compared to other materials. In addition, the advantage of being able to design MOFs that possess features such as open metal sites (OMSs), Lewis basic sites (LBSs), covalently-bound polar functional groups, tunable pore sizes, framework flexibility, and hydrophobicity, provides for a better handle on their tailorability. Specifically, the interaction of CO_2 with these sites tends to result in excellent CO_2 adsorption capacity and/or preferential CO_2 adsorption over other gas molecules, such as N_2, CH_4, and H_2O. Needless to say, MOFs can employ multiple interactions in a single structure to achieve extraordinary CO_2 adsorption.

Table 1 Summary of MOF-based adsorbents and the corresponding CO_2 capture capacity for each material[a]

Adsorbent	Pressure (bar)	Temperature (K)	Capacity (mmol g^{-1})	Ref.
		MOFs with open metal sites		
HKUST-1	1	298	4.1	98
Mg$_2$(dobpdc)	0.15	298	4.9	99
	1	298	6.4	
NU-1000	40	298	46.4	100
PCN-61	35	298	23.5	101
PCN-66		298	26.3	
PCN-68		298	30.4	
MIL-96	10	303	4.4	102
SNU-5	1	195	2.6	103
		273	0.9	
MIL-102	30	304	3.1	105
Cu-BTTri	0.06	298	0.3	106
	1	298	3.2	
Fe-BTT	1	298	3.1	107
PCN-88	1	273	7.1	108
		296	4.2	
NOTT-140	20	283	20.7	111
		293	19.5	
[Cd$_2$L1(H$_2$O)]$_2$	1	195	3.3	113
		293	2.1	
[Zn$_4$(OH)$_2$(1,2,4-BTC)$_2$(H$_2$O)$_2$]	1	295	1.9	114
[(CH$_3$)NH$_2$]$_3$[(Cu$_4$Cl)$_3$(btc)$_8$]·xMeOH	1	273	5.5	115
[Mg(3,5-PDC)(H$_2$O)]	1	298	0.6	116
[NH$_2$(CH$_3$)$_2$][Zn$_3$(BTA)(BTC)$_2$(H$_2$O)]	1	273	4.6	117
[NH$_2$(CH$_3$)$_2$]$_2$[Cd$_3$(BTA)(BTC)$_2$(H$_2$O)]$_2$			3.8	
Mg-MOF-74	0.1	296	5.4	120
	1		8.0	
Zn-MOF-74	0.1		1.3	
	1		5.5	
Ni-MOF-74	0.1		2.6	
	1		5.8	
Co-MOF-74	0.1		2.7	
	1		7.0	
		MOFs with both open metal and Lewis basic sites		
FJI-H14	1	195	12.5	109
		298	6.5	
		MOFs with Lewis basic sites		
NH$_2$-MIL-53	5	303	2.3	128
NH$_2$-MIL-125	1	273	4.0	130
		298	2.2	
CAU-1	1	273	7.2	131
IRMOF-74-III-(CH$_2$NH$_2$)$_2$	1	298	3.0	132
IRMOF-74-III-CH$_2$NH$_2$	1	298	3.3	133
Bio-MOF-11	1	298	4.1	134
Cu-TDPAT	0.1	298	1.4	135
	1		5.9	
MAF-25	1	195	5.2	138
MAF-26			3.8	
IFMC-1	1	195	7.5	140
		273	4.1	
		298	2.7	
MAF-23	1	273	3.3	141
		298	2.5	
CPF-6	1	273	4.4	142
ZJNU-43	1	296	4.6	143
ZJNU-44			5.2	
ZJNU-45			4.8	
MAF-66	1	273	6.3	144
		298	4.4	
ZTF-1	1	273	5.6	145
Zn$_2$(C$_2$O$_4$)(C$_2$N$_4$H$_3$)$_2$·(H$_2$O)$_{0.5}$	1.2	273	4.4	146
[Zn(dtp)]	1	195	4.4	147
		MOFs with polar functionalities		
TMOF-1	1	200	6.8	150
		273	2.2	
		298	1.4	
		308	1.2	

Table 1 (continued)

Adsorbent	Pressure (bar)	Temperature (K)	Capacity (mmol g^{-1})	Ref.
$[Zn(L2)]_n$	1	298	2.1	151
$Zn(BPZNO_2)$	1.2	298	5.0	152
USTC-253	1	273	3.7	155
		298	2.1	
USTC-253-TFA		273	6.1	
		298	2.9	
$[Zn(BDC-OH)-(TED)_{0.5}]\cdot1.5DMF\cdot0.3H_2O$	1	298	3.0	156
$[Zn(BDC-NH_2)-(TED)_{0.5}]\cdot xDMF\cdot yH_2O$			2.2	
LIFM-26	1	273	5.4	159
		298	3.3	
ZJNU-40	1	273	7.6	160
		296	4.8	
		Microporous MOFs		
Ni-4PyC	10	298	8.2	164
SNU-71	1	195	13.2	169
		298	1.0	
SUMOF-2	1	273	4.3	170
SUMOF-3			3.4	
SUMOF-4			3.6	
NOTT-202a	1	195	20.0	171
HPYR@ZnPC-2	0.15	298	0.7	172
HPIP@ZnPC-2			1.1	
CPM-33a	1	273	6.1	175
		298	3.3	
CPM-33b		273	7.8	
		298	5.6	
		MOFs with micropores and polar functionalities		
$(choline)_3[In_3(btc)_4]\cdot2DMF$	1	273	3.2	173
		MOFs with micropores and open metal sites		
CPM-5	1	273	3.6	174
		299	2.4	
		Flexible MOFs		
$[Zn_2(2,5-BME-bdc)_2(dabco)]_n$	1	195	4.6	179
$[Zn_2(DB-bdc)_2(dabco)]_n$			2.5	
SHF-61	20	298	2.4	180
PCN-123	1	295	1.0	182
$\{[Zn_2(BME-bdc)_2-(bipy)]_n(DMF)_{2.3}(EtOH)_{0.4}\}$	1	195	7.0	185
		273	2.3	
		298	1.5	
$[Sm(HL)(DMA)_2]$	20	333	0.6	186
$[Mn(bdc)(dpe)]$	1	195	4.9	187
$[Zn_2(L3)_2(dabco)]_n$	1	195	6.3	188
$[Zn_2(L4)_2-(dabco)]_n$			8.0	
$[Zn_2(L4)_2-(dabco)]_n$			8.9	
SNU-M10	1	195	5.5	189
		273	3.3	
		298	2.1	
SNU-M11		195	5.5	
		Post-synthetically modified MOFs		
mmen-Mg$_2$(dobpdc)	0.00039	298	2.0	99
	0.15	298	3.1	
	1	298	3.9	
Cu-BTTri-en	0.06	298	0.4	106
	1	298	1.3	
$[Mg_2(dobdc)(N_2H_4)_{1.8}]$	0.0004	298	3.9	199
$Mg_2(dondc)(en)_{1.5}(H_2O)_{0.5}$	1	298	2.6	201
$Mg_2(dondc)(mmen)_{1.2}(H_2O)_{0.8}$			4.1	
$Mg_2(dondc)(ppz)_{1.1}(H_2O)_{0.9}$			3.2	
dmen-Mg$_2$(dobpdc)	1	313	4.3	202
UiO-66(Ti$_{32}$)	1	273	2.3	206
UiO-66(Ti$_{56}$)			4.0	
Cr-MIL-101-SO$_3$H-TAEA	0.15	313	2.3	208
	0.0004	293	1.1	
UiO-66-aminoalcohol	20	308	11.6	209
UiO-66-SO$_3$H-0.15	1	298	2.2	210

Table 1 (continued)

Adsorbent	Pressure (bar)	Temperature (K)	Capacity (mmol g^{-1})	Ref.
UiO-66-SO$_3$Li-0.15			3.3	
SNU-31	1	298	0.6	211
	40		2.2	
LIFM-29	1	273	2.5	212
LIFM-30			2.6	
LIFM-31			2.6	
LIFM-32			2.7	
LIFM-33			3.6	
UiO-66-AD4	1	273	3.6	213
		298	1.9	
		323	1.1	
UiO-66-AD6		273	3.8	
		298	2.6	
		323	1.7	
UiO-66-AD8		273	3.3	
		298	1.8	
		323	1.0	
UiO-66-AD10		273	1.3	
		298	0.6	
		323	0.3	
UiO-66-(COOLi)$_2$-EX	1	273	1.7	214
		298	2.4	
UiO-66-(COONa)$_2$-EX		273	2.9	
		298	2.0	
UiO-66-(COOK)$_2$-EX		273	2.0	
		298	1.3	
UiO-66-(COOH)$_4$-EX		273	2.3	
		298	1.5	
UiO-66-(COOLi)$_4$-EX		273	3.4	
		298	2.3	
UiO-66-(COONa)$_4$-EX		273	1.9	
		298	1.2	
UiO-66-(COOK)$_4$-EX		273	0.9	
		298	0.6	
Tetramethylammonium@bio-MOF-1	1	273	4.5	216
		313	1.6	
Tetraethylammonium@bio-MOF-1		273	4.2	
		313	1.7	
Tetrabutylammonium@bio-MOF-1		273	3.4	
		313	1.4	
GND@bio-MOF-1	1	273	4.8	217
		313	1.6	
AmGND@bio-MOF-1		273	4.9	
		313	1.6	
DiAmGND@bio-MOF-1		273	5.1	
		313	1.7	
SNU-100'-Li	1	298	3.5	219
SNU-100'-Mg			3.4	
SNU-100'-Ca			3.4	
SNU-100'-Co			3.8	
SNU-100'-Ni			3.8	
Li@HKUST-1	18	298	10.6	240
MOF composites				
PEI-MIL-101-100	0.15	298	4.2	223
A-PEI-300	0.15	298	3.6	224
B-PEI-300			4.1	
PN@MOF-5	1	273	3.5	225
MgCGr-2	0.15	298	4.9	227
	1		6.8	
MgCGr-5	0.15		4.8	
	1		8.4	
MgCGr-10	0.15		5.5	
	1		8.1	
NiCGr-2	0.15		2.6	
	1		4.5	
NiCGr-5	0.15		3.2	
	1		5.9	
NiCGr-10	0.15		3.3	
	1		5.7	

2788 | Chem. Soc. Rev., 2019, 48, 2783–2828

This journal is © The Royal Society of Chemistry 2019

Table 1   (continued)

Adsorbent	Pressure (bar)	Temperature (K)	Capacity (mmol g^{-1})	Ref.
CG-3	1	273	7.9	228
CG-9			8.3	
CG-15			3.0	
HKUST-1@AC-2	1	273	8.1	229
HKUST-1/GO	1	298	3.2	231
HKUST-1/GO-U1			2.2	
HKUST-1/GO-U2			3.0	
HKUST-1/GO-U3			4.7	
MIL-53(Al)/GNP 2.5%	40	298	11.8	233
MIL-53(Al)/GNP 5%			13.0	
MIL-53(Al)/GNP 10%			9.1	
F-MOF1@AC-1	1	195	6.5	234
HCM-HKUST-1-1	1	298	2.4	235
HCM-HKUST-1-2			2.4	
HCM-HKUST-1-3			2.8	
5A@ZIF-8(I)	1	298	3.0	237
5A@ZIF-8(II)			2.6	
5A@ZIF-8(III)			2.1	
ZC-1	1	273	2.2	241
ZC-2			2.2	
ZC-3			2.0	
ZC-4			2.0	
ZC-5			1.8	
ZC-6			1.6	
CNT@HKUST-1	18	298	13.5	240

[a] Reports in this table include capacities in mmol g^{-1} (some have been converted to these units from the originally reported units).

2.1.1.   Open metal sites (OMSs). Accessing OMSs on MOFs' multimetallic secondary building units (SBUs) is one of the most widely used strategies to improve their CO_2 capture properties. In general, OMSs are generated by treating a MOF with coordinated terminal ligands such as water, *N,N*-dimethyl formamide (DMF), methanol, on the SBUs, under heat and/or vacuum to remove such ligands with retention of the overall structure. This often results in improved porosity in the activated material. These OMSs commonly serve as Lewis acid sites (LASs) that have been shown to coordinate CO_2. Such behavior at Lewis acidic OMSs endows many MOFs with high CO_2 affinities, especially at low adsorbate partial pressures.

The concept of designing OMSs and its implementation was reported in 1998 and 2000.[96,97] In 2005, the CO_2 uptake of HKUST-1, a MOF with OMSs, was found to be about 10 mmol g^{-1} at 42 bar and ambient temperature.[98] In HKUST-1, the room-temperature CO_2 adsorption isotherm appears as a typical Type I isotherm in which the most gas is adsorbed at low pressures, leading to a "knee" shape, indicative of high affinity of this MOF for CO_2 at low partial pressures. These conditions are interesting with respect to practical CO_2 adsorption from gas streams as the material will have large CO_2 capture working capacity. Following this work, a wide variety of MOFs bearing OMSs have been applied as CO_2 absorbents, including NU-1000, MIL-101, and M-MOF-74.[99–118] Among these, the M-MOF-74 (M = Mg^{2+}, Ni^{2+}, Co^{2+}, Zn^{2+}) isoreticular series, composed of an array of one-dimensional hexagonal channels with OMSs at the SBUs, has become one of the most well-studied sets of MOFs for CO_2 capture due to their extraordinary CO_2 uptake capacities at low pressures.[110,119] More importantly, the CO_2 adsorption of this series can be tuned based on the

metal from which the MOF is constructed. The CO_2 uptake of Mg-MOF-74 (5.4 mmol g^{-1} at 0.1 atm) is 2–4 times higher than those of the other isoreticular M-MOF-74 compounds at the same CO_2 loading pressures.[120] The zero-coverage isosteric heats of CO_2 adsorption (Q_{st}) of the frameworks details important information regarding the affinity of frameworks for CO_2. Applying this analysis to the M-MOF-74 isoreticular series, one concludes that Mg-MOF-74 exhibits the highest CO_2 affinity (47 kJ mol^{-1}), whereas Zn-MOF-74, Ni-MOF-74 and Co-MOF-74 exhibit initial affinities of 26, 37, and 41 kJ mol^{-1}, respectively.[120] This high affinity for CO_2 in Mg-MOF-74 stems from the increased ionic character of the Mg–O bond that imparts stronger charge-quadrupole interactions between the Mg OMSs and CO_2.

To further understand the mechanism of CO_2 adsorption on MOFs' OMSs, density functional theory (DFT) calculations, neutron powder diffraction experiments, infrared and Raman spectroscopy, and *in situ* solid-state ^{13}C nuclear magnetic resonance (NMR) measurements were performed.[119,121–123] Generally, CO_2 molecules interact with OMS in an end-on fashion through lone pair electron donation.[119] These fairly strong interactions only marginally alter the intramolecular angles of adsorbed CO_2. Additionally, DFT calculations suggest that CO_2 adsorption on the OMSs in these materials is still largely physisorptive.[121] This not only reduces the energy penalty for adsorbent regeneration, a key consideration in CO_2 capture, but also accelerates the adsorptive kinetics in MOFs.

With these studies, MOFs were evaluated for potential application in selective adsorption processes. For example, temperature swing post-combustion CO_2 adsorption was studied in MOF-177 and Mg-MOF-74.[124] While MOF-177 exhibits only poor to modest selectivity, Mg-MOF-74 was marked by tremendous selectivity

with an ideal adsorbed solution theory (IAST) selectivity factor of 148.1 at a typical flue gas temperature ($\sim$50 °C). In fact, the CO_2 selectivity of Mg-MOF-74 was even greater than that of the previously most studied zeolite NaX (87.4) under the same conditions. The methods in this study were applied to five different MOFs, targeting pre-combustion CO_2 capture, namely the selective capture of CO_2 in the presence of H_2.[125] Mg-MOF-74 has the highest CO_2/H_2 selectivity (859 at 5 bar) measured from an 80:20 H_2/CO_2 mixture at 313 K because of the greater polarizability of CO_2 compared to H_2 and the high concentration of OMSs in the MOF pore.

2.1.2. Lewis basic sites (LBSs). While the use of SBU-based OMSs for CO_2 capture lead to promising results with respect to adsorption capacity and selectivity, another important component of MOFs, the organic linkers, can also augment these properties. For instance, incorporation of organic linkers bearing LBSs into MOFs has been shown to greatly enhance their CO_2 binding affinities. This strategy was inspired by the outstanding CO_2 uptake capacities of aqueous amine solutions such as industrial solutions of monoethanolamine (MEA).[126,127] As an attempt to include Lewis basic amines into a MOF, 2-amino-terephthalic acid (NH_2-H_2BDC), was utilized in the synthesis of IRMOF-3, a MOF isoreticular to MOF-5.[98] At 298 K, and over a wide pressure range (from 0 to 12.3 bar), IRMOF-3 exhibits a higher CO_2 uptake capacity (0–14.7 mmol g^{-1}) than MOF-5 (0–14.0 mmol g^{-1}). This study indicated that greater CO_2 affinities can be achieved by introducing LBSs on the organic linkers. Similar phenomena were also observed in many isoreticular MOFs, such as NH_2-MIL-53, NH_2-UiO-66, and NH_2-MIL-125.[128–131] It is important to note here that many aromatic amines that have been incorporated into MOFs do not necessarily capture CO_2 in the same chemisorptive manner as aqueous amine solutions, given that aromatic amines lack the nucleophilicity of the alkyl-amines in solution. Recently, several functionalized IRMOF-III compounds were synthesized in hopes of capturing CO_2 in the presence of water (Fig. 1).[132,133] The linker-based amine functional groups of IRMOF-74-III-CH_2NH_2 endowed the material with the highest CO_2 uptake capacity (3.2 mmol g^{-1} at 800 Torr) of the series. In contrast to the aromatic amine cases detailed above, the alkylamines in IRMOF-74-III-CH_2NH_2 chemically bind CO_2, forming new, covalent species in the MOF. Solid-state cross-polarization magic angle spinning ^{13}C NMR spectra indicated that the major chemisorption product in this material was a mixture of carbamic acid (RNHCOOH) and ammonium carbamate (RNHCOO$^-$ $^+H_3$NR). More importantly, since the CO_2 capture took place at the linker-based alkylamines instead of the OMSs, the influence of water was negligible with respect to the CO_2 adsorption performance of IRMOF-74-III-CH_2NH_2. Therefore, this MOF captured CO_2 with a high capacity and selectivity even under 65% relative humidity. Recently, this strategy has been improved by doubling the linker-based alkylamines in the framework, yielding IRMOF-74-III-$(CH_2NH_2)_2$.[132] With two alkyl-amines per organic linker, the CO_2 adsorption capacity of the framework increased by more than 100% because the arrangement of the amines in the structure allowed for the formation of only carbamic acids under dry conditions. These carbamic
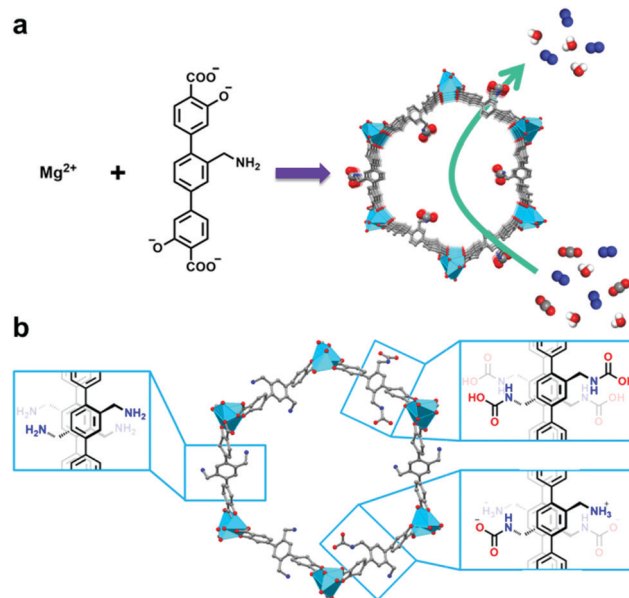

Fig. 1 (a) Synthesis of IRMOF-74-III-CH_2NH_2 from Mg^{2+} and the amine-functionalized linker (2′-(aminomethyl)-3,3″-dioxido-[1,1′:4′,1″-terphenyl]-4,4″-dicarboxylate) for selective, chemisorptive CO_2 capture from a $CO_2/N_2/H_2O$ gas mixture. (b) View of modeled IRMOF-74-III-$(CH_2NH_2)_2$ structure down the crystallographic c-axis, depicting the three pore environments before (left pore wall) and after exposure to CO_2 under dry conditions to produce carbamic acids (upper right pore wall) and 95% relative humidity (RH) to give ammonium carbamates (bottom right pore wall). Color code: C, gray; O, red; N, blue; H, white; and Mg, cyan.

acids are less stable and thus more easily removed, by vacuum or lower heat, than their ammonium carbamate counterparts which are formed when CO_2 is captured under humid conditions (Fig. 1b). Clearly, the strategy of amine-incorporation onto MOF linkers can be improved to target particular chemi-sorption products with desirable properties for specific CO_2 capture applications.

Apart from amine-functionalized linkers, other nitrogenous linkers, including pyrimidines, triazines, and azoles, have also been utilized to synthesize MOFs bearing LBSs.[134–148] In 2012, a new *rht*-type MOF, Cu-TDPAT, based on an LBS-rich hexa-carboxylate ligand (H_6TDPAT) was reported.[135] Its CO_2 adsorption capacity (5.9 mmol g^{-1} at 298 K and 1 atm, 10.1 mmol g^{-1} at 273 K and 1 atm) and isosteric heat of adsorption (42 kJ mol^{-1}) were substantially higher than many previously reported *rht*-type MOFs. To investigate the interactions between Cu-TDPAT and CO_2, room-temperature IR spectroscopy was conducted after CO_2 loading showing the evolution of a distinct band at $\nu = 2335$ cm^{-1} perhaps attributable to CO_2 adsorption at the LBSs.

While LBS incorporation strategies are effective, MOF–CO_2 interactions remain mainly single site in nature. Reliance on such interactions can result in relative weak framework affinities for CO_2 or low reversibility.[141] As an alternative approach, MOFs can be designed such that their pores are decorated with multiple LBSs. The cooperation between these can endow the resultant MOFs with high CO_2 binding affinities, high selectivities, and reversible CO_2 adsorption. A flexible framework, MAF-23, was made from a
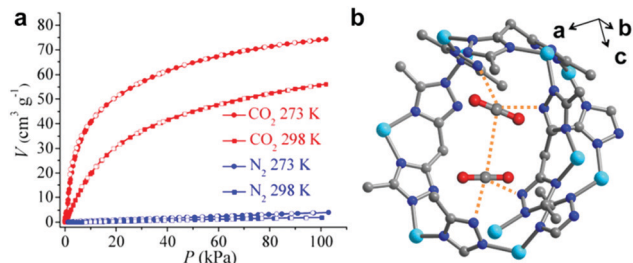
2790 | *Chem. Soc. Rev.*, 2019, **48**, 2783–2828

This journal is © The Royal Society of Chemistry 2019

Fig. 2 (a) CO_2 (red) and N_2 (blue) adsorption (solid) and desorption (open) isotherms at 273 K (circle) and 298 K (square) of MAF-23. Reproduced from ref. 141 with permission from the American Chemical Society, copyright 2012. (b) The perspective views of two CO_2 molecules adsorbed by the N···N claws of activated MAF-23. In this structure, four independent uncoordinated N atoms come from four different triazolate rings. Orange lines depict the interactions between two CO_2 molecules and the framework. H atoms are omitted for clarity. Color code: C, gray; N, blue; Zn, cyan; and O, red.

chelating-bridging ligand (bis(5-methyl-1H-1,2,4-triazol-3-yl)methane, H_2btm),[141] where the available triazolate N-donors of the organic linker acted as CO_2 chelation sites. At 1 atm, MAF-23 exhibited a CO_2 uptake capacity of 3.3 and 2.5 mmol g^{-1} at 273 and 298 K (Fig. 2a), with CO_2/N_2 selectivities calculated by Henry's law of 163 and 107 at 273 and 298 K, respectively. To elucidate the dynamic CO_2 adsorption behavior, the crystal structure of MAF-23 with different CO_2 loading levels was determined using single-crystal X-ray diffraction. From the data, two independent CO_2 molecules could be observed, located near the chelation sites of the organic linkers (Fig. 2b).

The quantity and accessibility of MOFs' LBSs also play vital roles in the tunability of CO_2 uptake capacities in MOFs. A series of isoreticular copper-based MOFs, ZJNU-43, ZJNU-44 and ZJNU-45, based on three rigid organic likers, 5,5′-(quinoline-5,8-diyl)-diisophthalate, 5,5′-(isoquinoline-5,8-diyl)-diisophthalate, and 5,5′-(quinoxaline-5,8-diyl)-diisophthalate, were constructed.[143] Although these MOFs had nearly identical surface areas, distinct differences were observed in their CO_2 uptake capacities. In ZJNU-43, the linker-based nitrogen atom is located at the α-position in the spacer of the organic linkers. Upon activation, ZJNU-43 adsorbed 4.6 mmol g^{-1} CO_2 at 1 atm and 296 K. When the LBSs were shifted to the β-position in ZJNU-44, the CO_2 uptake capacity increased significantly (to 5.2 mmol g^{-1}) under the same conditions. When the number of the LBS at the α-position was doubled, the adsorption capacity of the resulting MOF, ZJNU-45, was only 4.8 mmol g^{-1}, slightly greater than ZJNU-43. Quantum chemical calculations indicated that CO_2 in the structures of ZJNU-43 and ZJNU-45 were trapped in narrow windows, stabilized by numerous weak hydrogen bonds between CO_2 and the H, N, and O atoms of the organic linkers. In contrast, the LBSs of ZJNU-44 pointed into the pores, allowing CO_2 to bridge the organic linkers. Ultimately, the calculated binding energies of CO_2 in the series of MOFs indicated the value of ZJNU-44 (-27.6 kJ mol^{-1}) was much larger than those of other two MOFs (-18.1 and -18.7 kJ mol^{-1}), explaining the high CO_2 adsorption capacity of ZJNU-44. These examples highlight the role of LBSs' orientation in MOF pores and its impact on CO_2 capture.

2.1.3. Linkers with polar functional groups.

With respect to MOFs synthesized with linkers lacking LBSs, the introduction of alternative polar functional groups such as $-F$, $-Br$, $-Cl$, $-OH$, $-COOH$, $-NO_2$, and $-SO_3$ on the organic linkers of MOFs can also enhance CO_2 capacity. This is based on interactions between the dipole of the polar functional group and the quadrupole of CO_2. Generally, two methods have been employed toward the synthesis of MOFs bearing such polar functional groups. The first is direct synthesis of MOFs using functionalized linkers. Numerous studies indicate that incorporation of these linkers into the frameworks results in favorable CO_2 adsorption.[149–152] A representative example is found in the synthesis and study of CD-MOF-2, constructed from γ-cyclodextrin (γ-CD) and rubidium hydroxide.[153] Solid-state NMR experiments showed that the free hydroxyl groups located on γ-CD reacted with CO_2, forming carbonic acid groups in a chemisorptive fashion (Fig. 3a). This chemisorption led to a large CO_2 uptake capacity (~ 1.0 mmol g^{-1}) in the low-pressure region (<1 Torr) between 273–298 K.[149] Unfortunately, when the crystals of CD-MOF-2 were pulverized into amorphous powders, very little CO_2 was absorbed and the steep rise also disappeared from the low-pressure region of the CO_2 adsorption isotherms (Fig. 3b and c). This result highlighted the need for crystallinity and porosity in MOFs when targeting gas adsorption.

Another strategy employed to introduce polar functional groups in the pores of MOFs relies on deviating from the commonplace metal-carboxylate chemistry employed in MOF synthesis. To this end, sufficient evidence exists to suggest that organosulfonates may offer a better platform for the construction of MOFs with highly polar pore environments. A mixed-linker strategy was used to synthesize a sulfonate-based MOF (TMOF-1)[150] where the free oxygen atoms from the sulfonate groups were charged and highly polar. Therefore, the CO_2 uptake capacity of TMOF-1 at 200–308 K was 1.2–6.8 mmol g^{-1} under 1 bar with a high zero-coverage isosteric heat of adsorption of 30.9 kJ mol^{-1}, much higher than many reported organosulfonate-based MOFs. The hypothesized CO_2 "encapsulation" in which adsorbed CO_2 was surrounded by four sulfonate groups facilitated the strong CO_2 binding in the framework. Polar functional groups can also be incorporated during the synthesis of the extended structure.
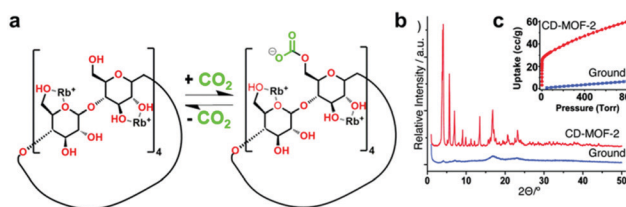

Fig. 3 (a) An illustration of the reversible carbonic acid formation during CO_2 chemisorption by free hydroxyl groups located on each individual γ-CD torus of CD-MOF-2. (b) Powder X-ray powder diffraction (PXRD) analysis of pristine CD-MOF-2 (red, top) and a sample ground in a mortar and pestle for 7 min (blue, bottom). (c) CO_2 uptake isotherms (298 K) for crystalline CD-MOF-2 (red circles) and a sample ground into an amorphous powder (blue squares). Reproduced from ref. 149 with permission from the American Chemical Society, copyright 2011.

This journal is © The Royal Society of Chemistry 2019

Chem. Soc. Rev., 2019, 48, 2783–2828 | 2791

A zinc-imidazolate-4-amide-5-imidate framework (IMOF) was synthesized by an *in situ* ligand reaction and studied for CO_2 uptake.[151] During the MOF synthesis, a new, chelating, imidazolate ligand was generated by partial hydrolysis of the original linker, eventually forming narrow channels with polar walls. The total CO_2 adsorption capacity of the resultant IMOF was 2.1 mmol g^{-1} at 298 K and 1 bar, due to the strong interactions between CO_2 and the amide and imidate functional groups.

The designability and flexibility of MOFs can also be leveraged to introduce polar functional groups into the pore structure.[154–161] Utilizing the isoreticular approach, a given MOF's pore surface functionality can be adjusted by utilizing different organic linkers, all while maintaining the underlying topology of the parent MOF. For example, seven zeolitic imidazolate frameworks (ZIFs), all with GME topology and variously controlled pore metrics and functionality were examined for their CO_2 uptake behavior.[154] The CO_2 uptake capacities of these ZIFs tracked with the expected attraction between polar functional groups in the ZIFs and CO_2. ZIF-78, bearing –NO$_2$ groups, adsorbed ~60 cm^3 cm^{-3} of CO_2 at 298 K and 800 Torr, a value much higher than the CO_2 uptake values of the other ZIFs in the series with –Cl, –CN, –Me, and –Br moieties. Another example is the stable Al-based MOF, USTC-253, constructed from Al^{3+} and dibenzo[*b*,*d*]thiophene-3,7-dicarboxylate 5,5-dioxide (Sbpdc) whose structure is isoreticular to MOF-253.[155] However, in comparing the total CO_2 uptake capacities of these two frameworks, the impact of the presence of the linker-based polar sulfone groups becomes apparent. The CO_2 uptake capacity of USTC-253 at 273 K and 1 bar is 3.7 mmol g^{-1}, 71% higher than that of MOF-253, despite the presence of bipyridine N atoms (LBSs) in the latter MOF. Moreover, when trifluoroacetic acid (TFA) was utilized as a modulator during the synthesis of USTC-253, the resultant USTC-253-TFA exhibited a higher CO_2 adsorption capacity due to the introduction of defects. Additionally, the framework adsorbed very little N$_2$ under the same conditions, yielding a CO_2/N$_2$ selectivity of 75:1. Such results highlight the importance of polar functional group incorporation in MOFs and the immense potential of application of this strategy to post-combustion CO_2 capture.

2.1.4. Pore size control. CO_2 has a relatively small kinetic diameter (3.3 Å). For this reason, micropores are typically more advantageous than mesopores and/or macropores when targeting enhanced CO_2 uptake capacity and selectivity. In the context of the application of MOFs to CO_2 capture, deliberate selection of metal salts and organic linkers can result in the formation of a variety of pore sizes. For example, by altering the length of the organic linkers in two frameworks, isoreticular series of MOF-5 and MOF-74 with pore apertures ranging from 3.8 to 28.8 Å and from 14 to 98 Å, respectively, were prepared.[162,163] With this as a backdrop, an ultra-microporous (3.5 and 4 Å) MOF, Ni-4PyC, based on a short ligand 4-pyridylcarboxylate (4Pyc) was reported.[164] Grand canonical Monte Carlo (GCMC) simulations predicted that Ni-4PyC could adsorb up to 8.2 mmol g^{-1} of CO_2 at 10 bar and 298 K.[164] The experimental CO_2 adsorption measurement result (~8.2 mmol g^{-1} at 10 bar and 298 K) was in good agreement with the simulated isotherm. In addition, simulations indicated that three main CO_2 binding locations
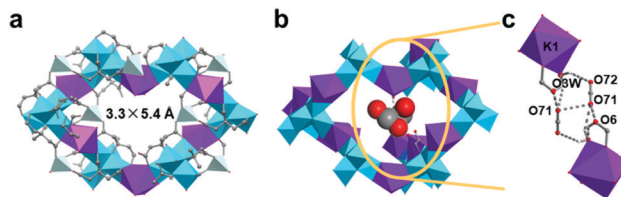

Fig. 4 (a) The diamondoid cage of UTSA-16 with a small 3.3 × 5.4 Å^2 window. All metal ions are represented as polyhedra. (b) CO_2 dimers are trapped within the cage upon gas adsorption. (c) Cyrstallographically observed cooperative interactions between CO_2 molecules and the framework (O$_{71}$(CO$_2$)···O$_{71}$(CO$_2$) and O$_{71}$(CO$_2$)···O$_6$ short contact; O$_{72}$(CO$_2$)···H−O$_{3w}$, O$_{71}$(CO$_2$)···H−O$_{3w}$ and O$_{3w}$···H−O$_6$ hydrogen-bonding interactions). Color code: C, gray; O, red; K, purple; Co1, light turquoise; Co2, cyan; and H, white.

existed in Ni-4PyC, located in the intersections of channels, 1D channels, and spherical cages. Also, cooperative binding between CO_2 molecules was proposed to play a significant role in the exceptionally high CO_2 uptake of Ni-4PyC. Unexpectedly, in contrast to the excellent CO_2 adsorption performance, Ni-4PyC adsorbed almost no H$_2$ even at very high pressure (up to 35 bar), making it an ideal candidate for pre-combustion CO_2 capture. Using a similar strategy, a microporous MOF, UTSA-16, assembled from Co(OAc)$_2$·4H$_2$O, citric acid (H$_4$cit), and KOH was prepared and studied by neutron diffraction to reveal two pairs of CO_2 molecules trapped by hydrogen-bonding in the materials' micro pores (~3.3 × 5.4 Å^2) (Fig. 4).[165] These small diamond cages and binding sites not only endowed UTSA-16 with a significantly large CO_2 uptake capacity (160 cm^3 cm^{-3} at 296 K and 1 bar) but also enhanced the MOF's CO_2/CH$_4$ (29.8 at 200 kPa and 296 K) and CO_2/N$_2$ (314.7 at 100 kPa and 296 K) separation capabilities. As an example contributing to the fundamental understanding of precise CO_2 binding modes in a given MOF, the study on UTSA-16 demonstrates that measuring capacity alone may not be sufficient to address underlying framework chemistry.

Self-interpenetration resulting in mutually interlocking frameworks is known to occur in certain MOF topologies.[166] This has a couple of effects on CO_2 capture: when interpenetration reduces surface area, this in turn reduces the overall capacity; however, when more restrictive pores result from interpenetration, it has the effect of increasing the binding energy of CO_2 and therefore giving more favorable uptake.[166] There are cases where interpenetration as well as mixed linkers in MOFs produce what has been called pore space partition (PSP), where the original pores have been segmented in a designed fashion. This also has the effect of restricting pores and increasing CO_2 uptake.[166,167] A 2-fold interpenetrated microporous MOF, Cu(FMA)(4,4′-BPE)$_{0.5}$, with a 3.6 Å pore diameter was reported and exhibited highly selective adsorption of CO_2 over CH$_4$ at 195 K.[168] Two nearly identical frameworks, SNU-70 and SNU-71, in which the only difference between the organic linkers was the discrepancy between a C=C or a C−C bond.[169] SNU-71, which is interpenetrated, exhibited high CO_2 adsorption capacities at low pressures regardless of temperature, due to the decreased pore size compared to the non-interpenetrated SNU-70. In SUMOF-*X* (*X* = 2–4), H$_2$BDC, H$_2$NDC, and H$_2$BPDC were utilized

as linkers to obtain three interpenetrated MOFs.[170] The authors speculated that the higher uptake of CO_2 in these interpenetrated MOFs compared with their non-interpenetrated counterparts could be attributed to the increased electric field gradients in the small pores of interpenetrated frameworks, enhancing the interactions between CO_2 molecules and the host framework. Apart from structures that commonly interpenetrate, an unusual partially interpenetrated MOF, NOTT-202a, formed as the result of a pronounced framework phase transition during desolvation.[171] At 195 K and 1 bar, NOTT-202a exhibited a high CO_2 storage capacity of 20 mmol g^{-1}, exceeding many previously reported values in In(III)-based MOFs.[171]

Pore space partition (PSP) serves to decrease MOFs' pore sizes by dividing large cages or channels into smaller segments by the insertion of additional organic linkers or other guest species.[79] PSP has gradually became a crucial tool to efficiently utilize the pore spaces of MOFs.[79,172] A microporous anionic framework, $[In_3(btc)_4]_n^{3n-}$, was synthesized in seven distinct chemical environments, including a variety of organic solvents, ionic liquids, and deep eutectic solvents.[173] Some of the solvents were incorporated into the resultant MOFs as extra-framework charge-balancing species. Even with the occupation of a large percentage of the pore space by charge-balancing cations like choline, the MOF, $(choline)_3[In_3(btc)_4]\cdot2DMF$, exhibited a CO_2 uptake capacity of 3.2 mmol g^{-1} at 1 atm and 273 K on account of reasonably partitioned pore spaces and hydroxyl groups on the choline cations. The same group reported an interesting cage-within-cage indium-based MOF (CPM-5) by employing In^{3+} and BTC^{3-} as metal ions and linkers, respectively.[174] In the structure of CPM-5, a small Archimedean In_{12} cage is encapsulated within a large Archimedean In_{24} cage and every two adjacent In^{3+} sites of the In_{24} cage are connected by two carboxylate groups from the BTC^{3-} linker. The remaining carboxylate group from BTC^{3-} connects the outer In_{24} cage with the inner In_{12} cage. At 273 K and 1 atm, CPM-5 adsorbed a significant amount of CO_2 (3.6 mmol g^{-1}). This was attributed to the synergy between open In^{3+} sites, charges in the framework, and the pore space partitioning effect from the cage-within-cage architecture. More recently, a symmetry-matching regulated ligand insertion strategy was developed to make crystalline porous materials with exceptional CO_2 uptake capacities.[175] To partition the pore space, organic linkers with C_3 symmetry such as 2,4,6-tri(4-pyridyl)-1,3,5-triazine (tpt) were employed to occupy the channel of MIL-88 type structures. This yielded a series of isoreticular CPM-X (X = 33a–d) structures by fragmenting the channels into numerous small segments (Fig. 5). By providing additional adsorptive surfaces upon incorporation of tpt, CPM-33b exhibited a very high CO_2 uptake capacity (7.8 and 5.6 mmol g^{-1} at 273 and 298 K, respectively, under 1 bar) and a moderate isosteric heat of adsorption (25.0 kJ mol^{-1}) even through the OMSs in the structure were coordinated by tpt ligands.

2.1.5. Flexible frameworks. Another property of MOFs is their propensity for structural flexibility. Upon exposure to external stimuli such as pressure and/or temperature, certain MOFs undergo structural change(s), resulting in "gated" CO_2 adsorption. In such cases, the CO_2 adsorption capacities of these MOFs
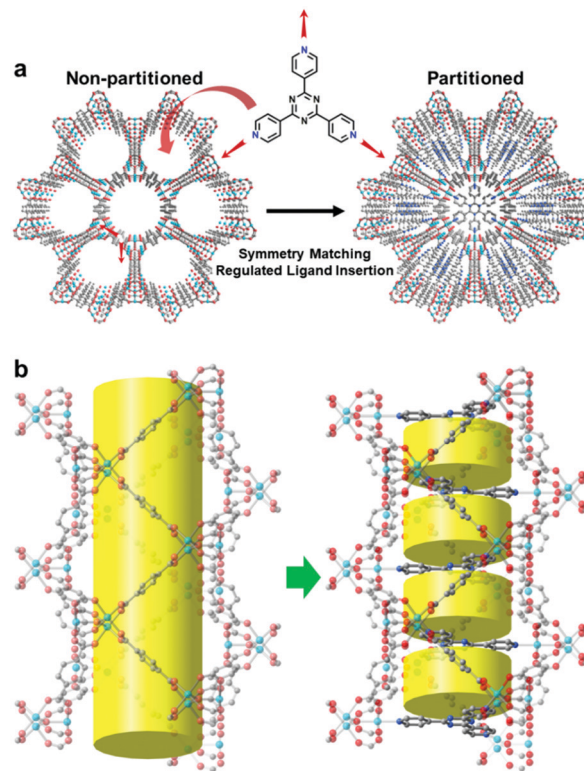

Fig. 5 Pore space partitioning through symmetry-matching regulated ligand insertion in a representative MOF (CPM-33a). (a) Viewed along c axis and (b) side view of the channels showing the cylindrical channel before and after partition using 2,4,6-tri(4-pyridyl)-1,3,5-triazine. Color code: C, gray; O, red; N, blue; and Ni, cyan. H atoms are omitted for clarity. Adapted from ref. 175 with permission from the American Chemical Society, copyright 2015.

suddenly and drastically increase at a definite relative pressure known as a gate pressure. It is generally accepted that the structural flexibility of MOFs is mainly related to the so-called soft porous crystals with a "breathing effect".[38,176,177] In a representative example, a flexible, doubly interpenetrated zinc(II) MOF was reported.[178] The CO_2 adsorption isotherm revealed a drastic adsorption step at about 10 bar and significant hysteresis during CO_2 desorption.[178] The calculated CO_2 uptake and Q_{st} were 7.1 mmol g^{-1} at 30 bar and 298 K and ~20 kcal mol^{-1}, respectively. Variable temperature and pressure PXRD measurements were performed to study the effect of CO_2 adsorption on the underlying MOF structure. The results indicated that the framework contracted upon activation accompanied by considerable changes in the powder pattern. When CO_2 was loaded into the framework, the original pattern reappeared, indicating that a reversible structural transformation or "breathing" behavior was occurring. Another interesting example of the application of "breathing" MOFs to CO_2 capture can be found in a series of flexible pillared-layered MOFs. Based on a library of variably functionalized bdc-type linkers, the dangling side chains of $[Zn_2(bdc)_2(dabco)]_n$ acted as immobilized "guests" and interacted with other guest molecules, themselves, and the framework backbone.[179] This had the effect of significantly enhancing the frameworks' flexibility. Gas sorption measurements showed

This journal is © The Royal Society of Chemistry 2019

Chem. Soc. Rev., 2019, **48**, 2783–2828 | **2793**

that each MOF could selectively adsorb CO_2 in a distinct stepwise fashion, while N_2 was almost never adsorbed in any appreciable quantity. More recently, SHF-61, a diamondoid continuous-breathing network, was synthesized from reactions between $InCl_3$ and NH_2-BDC.[180] Desolvation of the as-synthesized material led to a drastic change in not only the MOF's morphology but also its unit-cell volume ($\Delta V \approx 2000$ Å^3), as monitored by a series of single-crystal X-ray diffraction experiments. The partially solvated SHF-61-DMF exhibited the largest CO_2 uptake among those in the series (2.4 mmol g^{-1} at 20 bar and 298 K) with minor desorption hysteresis caused by a structural phase transition. An elastic layered MOF, ELM-11, displayed a gate-adsorption isotherm (195 K) with two steps at 0.2–0.4 kPa and 14–30 kPa.[181] With the aid of *in situ* synchrotron PXRD measurements, two structural transitions and one gradual deformation of ELM-11 were observed during the CO_2 adsorption process.[181]

Structural flexibility can also stem from the incorporation of organic linkers into MOFs that are sensitive to external stimuli such as light.[182,183] As an example of such behavior, we turn to a photoswitchable MOF (PCN-123) made from $Zn(NO_3)_2\cdot6H_2O$ and 2-(phenyldiazenyl)terephthalate which is isostructural to MOF-5.[182] UV irradiation and heat treatment isomerized the organic linkers in *trans*-to-*cis* and *cis*-to-*trans* fashions, respectively. Based on this isomerization, the CO_2 uptake capacity of PCN-123 could be reversibly altered with the all *trans* configuration of the organic linkers yielding the higher CO_2 adsorption capacity (Fig. 6). An example of low-energy CO_2 capture and release in a light-responsive framework, $Zn(AzDC)(4,4'$-BPE$)_{0.5}$, was also reported.[183] When the AzDC and 4,4'-BPE linkers were photoisomerized between *cis* and *trans* states upon exposure to 365 nm light, an instantaneous release of about 64% (under dynamic measurements) and 42% (under static conditions) of adsorbed CO_2 was observed. It is important to note that significant structural change in $Zn(AzDC)(4,4'$-BPE$)_{0.5}$ was not observed by synchrotron X-ray diffraction.

As has previously been discussed, gas separation and purification can be carried out by tailoring porous materials to have specific interactions with the molecule of interest. Therefore, discriminatory gate-opening can endow flexible MOFs with highly efficient CO_2 separation properties.[184–189] For instance, one can observe conventional CO_2 uptake behavior with dynamic adsorption of other species. Such a phenomenon was reported for a flexible porous coordination polymer (PCP), [Mn(bdc)(dpe)], with zero-dimensional pores.[187] In addition to the Type I CO_2 adsorption isotherm (at 195 K), Mn(bdc)(dpe) displayed gate opening adsorption behavior for acetylene (C_2H_2). Below the gate opening pressure ($P_{go} = 1.45$ kPa), negligible C_2H_2 was adsorbed by the PCP, endowing the material with highly selective adsorption of CO_2 over C_2H_2. As expected, IAST calculations indicated that the CO_2/C_2H_2 selectivity ranged from 8.8 to 13 for an equimolar CO_2/C_2H_2 gas mixture. To investigate the mechanism of selective adsorption, Mn(bdc)(dpe) was post-synthetically modified by [2+2] photodimerization of the dpe linkers yielding a new PCP, $Mn_2(bdc)_2(rctttpcb)$. In the new PCP, the CO_2 and C_2H_2 uptake capacities were nearly identical (0.6 mmol g^{-1} *vs.* 0.5 mmol g^{-1}), supporting the hypothesis that interactions between CO_2 and the linker-based phenylene rings played crucial roles in the gradual CO_2 adsorption in Mn(bdc)(dpe). It was also found that the chain length of alkyl ether groups (dangling on the benzene rings) and group substitution pattern of organic linkers had huge impacts on the structural flexibility and adsorption selectivity of MOFs.[188] $Zn_2(L^1)_2$(dabco) (L^1 = 2,5-bis(2-methoxyethoxy)benzene), which is isoreticular to $[Zn_2(bdc)_2$-(dabco)$]_n$,[190] exhibits a unique two-step CO_2 uptake isotherm due to its structural flexibility. However, negligible N_2 and CH_4 adsorption was observed at 77 and 195 K, respectively. The authors speculated that the flexible and polar alkyl ether groups served as molecular gates at the MOF's pore apertures. Therefore, polar gas molecules such as CO_2 could penetrate the molecular gates more easily than their nonpolar counterparts such as N_2.

2.1.6. Hydrophobic frameworks. It is important to recognize that all practical CO_2 adsorption must occur in the presence of water. Therefore, hydrophobic frameworks are suitable for capturing CO_2 under humid conditions. Although water's large dipole moment causes it to interact more strongly than CO_2 with most frameworks, the hydrophobicity of certain MOFs allows them to suppress competitive water adsorption.

Generally, the hydrophobicity of a given MOF stems from bulky hydrophobic organic linkers or pendant hydrophobic groups on the organic linkers. For example, a series of ZIFs of chabazite (CHA) zeolite topology were made from a mixture of linkers.[191] The entire series displayed negligible water uptake and were able to separate CO_2 from mixed gas streams without any loss of uptake capacity over three cycles under dry or humid conditions. Additionally, hydrophobic MOFs can employ the strategies we have previously outlined. For example, the CO_2 adsorption properties of a flexible and superhydrophobic MOF, FMOF-1, were modeled under humid conditions using quantum mechanical simulations.[192] With many CF_3 groups lining the pores, FMOF-1 exhibited superhydrophobicity as indicated by its high contact angle with water (158°). Simulated mixed-gas isotherms of CO_2 and water demonstrated that the
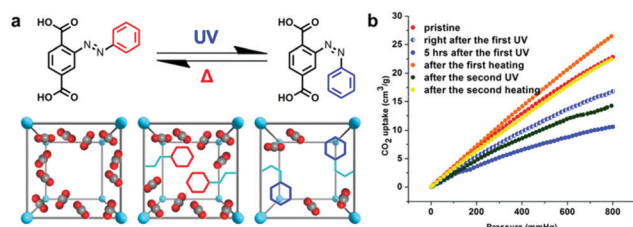

Fig. 6 (a) (top) *trans*-to-*cis* isomerization of the ligand (2-styrylterephthalic acid) of PCN-123 (PCN = porous coordination networks) induced by UV irradiation and the *cis*-to-*trans* isomerization induced by heat treatment. (bottom) Suggested CO_2 uptake in MOF-5 (left), PCN-123 *trans* (middle), and PCN-123 *cis* (right). Each MOF is composed of Zn-oxo clusters (cyan balls) linked together by organic linkers (gray lines). The benzene rings in the azo functional group are highlighted in red and blue lines in PCN-123 *trans* and PCN-123 *cis*, respectively. (b) CO_2 adsorption isotherms (at 295 K) of PCN-123 indicating altered adsorption behavior as the result of reversible linker conformational change of organic linkers. Reproduced from ref. 182 with permission from the American Chemical Society, copyright 2012.

2794 | *Chem. Soc. Rev.*, 2019, **48**, 2783–2828

This journal is © The Royal Society of Chemistry 2019

CO_2 adsorption capacity of FMOF-1 was not influenced by water even at 80% relative humidity. Analogously, a family of iso-structural MOFs was made by employing bi-functional organic linkers with both basic azolyl and chelating carboxylate groups.[193] The basic azolyl functional groups interacted with CO_2 and the $-OCH_3$ groups from acetate moieties on the pore surface provided a hydrophobic lining to the pore-walls, allowing the MOF to maintain approximately 80% of its CO_2 adsorption capacity upon exposure to 75% relative humidity.

2.2. Crafting MOFs' interiors through post-synthetic modification

The intrinsic features of MOFs provide favorable conditions for CO_2 capture and separation. Nevertheless, in the *de novo* synthesis of MOFs, the introduction of certain specific adsorption sites or functional groups can be challenging due to poor solubility of the organic linkers, competitive reactions between functional groups and the target frameworks, or the sensitivity of frameworks to the alteration of either the metal ions/ligands or their coordination environment(s). In this context, post-synthetic strategies for the incorporation of desired functionalities into MOFs have been developed. In general, post-synthetic approaches to improve MOFs' CO_2 capture capabilities can be classified into two broad categories: post-synthetic modification, and the formation of MOF composites.

2.2.1. Post-synthetic modification.
Post-synthetic modification (PSM) can serve as a facile technique to introduce new CO_2 adsorptive sites into MOFs without significantly altering or damaging the underlying structure.[194] Specifically, PSM has been employed to accomplish the following: (1) introduction of additional functional groups, such as amine groups, or exchange of metals in the SBUs, (2) modification, insertion, or exchange of organic linkers, and (3) cation exchange in anionic MOFs.

In the case of SBU PSM, grafting alkylamine moieties onto OMSs serves as an effective means of improving the CO_2 uptake performances of MOFs based on the aforementioned strong affinities of alkylamines for Lewis acidic CO_2 molecules. As an example, the coordinatively unsaturated Cu^{II} sites in a water stable and trizolate-bridged MOF (Cu-BTT) were capped with ethylenediamine (en).[106] Although the pores of resultant material were occluded leading to relatively low CO_2 uptake at relatively high pressures, the CO_2 uptake at low pressures, CO_2/N_2 selectivity, and Q_{st} values dramatically increased compared to those associated with the pristine MOF. This technique was also successfully extended to other MOF systems.[99,195–204] Among these, Mg-MOF-74, with a high concentration of OMSs and one of the highest CO_2 adsorption capacities at low CO_2 pressures (6.1 mmol g^{-1} at 298 K and 0.15 bar),[120] has been identified as an ideal platform for post-synthetic amine functionalization. Unfortunately, its relatively narrow, one-dimensional channels ($\sim$11 Å) hinder effective diffusion of sterically bulky amines into the pores. For this reason, extended MOF-74-type structures such as Mg_2(dobpdc), Mg_2(dotpdc) and Mg_2(dondc) were utilized as substitutes for post-synthetic amine incorporation. All of the diamine-appended MOFs exhibited not only exceptional CO_2 adsorption capacities but also high CO_2 adsorption selectivity.[99,196–198,201–204]

Additionally, the thermal and chemical stabilities under humid condition of the resultant materials were markedly enhanced, despite reduction of their Brunauer–Emmett–Teller (BET) surface areas and pore volumes.[99,198–200] As an alternative to pore-expansion, the OMSs of Mg-MOF-74 were capped with a much smaller amine (hydrazine), yielding Mg-MOF-74$(N_2H_4)_{1.8}$.[199] The authors assumed that hydrazine would promote effective CO_2 adsorption in the MOF after PSM due to its small size, yet similar chemistry to other amines. Additionally, the distances between two adjacent amines were quite large. This inhibited the formation of weak hydrogen bonds and greatly enhanced the utility and availability of the grafted amines. Ultimately, the CO_2 uptake of Mg-MOF-74$(N_2H_4)_{1.8}$ at 298 K and 0.4 mbar, the partial pressure of CO_2 in air, was 3.9 mmol g^{-1} due to the high concentration (6.0 mmol g^{-1}) of surface-appended hydrazines. The Q_{st} calculated by the Clausius–Clapeyron equation and the Virial fitting method gave near zero-coverage values of 118 and 90 kJ mol^{-1}, respectively. These high heats of adsorption necessitate relatively high regeneration temperatures for such adsorbents. This interplay is an outstanding challenge in CO_2 capture; one desires strong chemical bonds between CO_2 molecules and the adsorbent to achieve selectivity, but strong bonds also typically require high adsorbent regeneration temperatures. As such, investigations into the modification of MOF SBUs with other CO_2-philic moieties were carried out. For example, a new functionalization technique, solvent assisted ligand incorporation (SALI) was developed with the goal of introducing perfluorinated chains onto the Zr_6 SBU of NU-1000. In this case, the technique relied on acid–base chemistry between the hydroxyl groups on the Zr_6 SBU and the carboxylate group of the fluoroalkyl linker (Fig. 7).[205] All the fluoroalkane-functionalized samples had higher CO_2 adsorption capacities and zero-uptake limit (Q_{st}^0) than those of the parent NU-1000, which can be attributed to the interactions between the C–F dipoles and the quadrupole of CO_2. More importantly, the Q_{st}^0 value for each sample was no greater than 35 kJ mol^{-1}, implying that these adsorbents could be easily regenerated.

Post-synthetic modification for enhanced CO_2 capture in MOFs is not limited to the modification of the metals' coordination environments. Post-synthetic exchange (PSE) of metal atoms in SBUs is also a promising approach and can improve the CO_2 uptake capabilities and/or selectivities of MOFs.
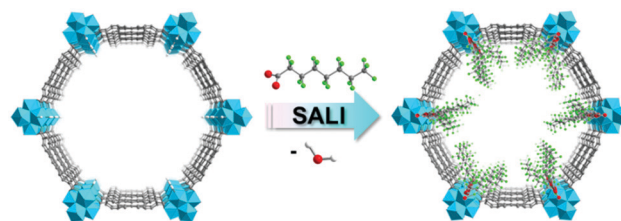

Fig. 7 Solvent-assisted ligand incorporation (SALI) on NU-1000 as a result of the reaction between the hydroxyl groups on the Zr_6 SBU (turquoise polyhedra) and the carboxylate groups bearing the perfluorinated chain (2,2,3,3,4,4,5,5,6,6,7,7,8,8,8-pentadecafluorooctanoate). Color code: C, gray; O, red; F, green; H, white; and Zr, cyan.

The Zr(IV) ions of UiO-66 can be exchanged with Ti(IV) ions by immersing UiO-66(Zr$_{100}$) in a DMF solution of TiCl$_4$(THF)$_2$ for various lengths of time at 368 K to give UiO-66(Zr/Ti) with progressively higher Ti loadings.[206] The pore size distributions of the resultant frameworks as measured by N$_2$ adsorption experiments demonstrated that the size of the octahedral pores dramatically decreased as a result of the shorter Ti–O bonds compared to Zr–O bonds. The CO$_2$ adsorption capacity of UiO-66(Zr/Ti) increased from 2.2 (UiO-66(Zr$_{100}$)) to 4.0 mmol g^{-1} (UiO-66(Ti$_{56}$)), which was ascribed to synergistic effects between the reduced pore size and framework density of the Ti-exchanged UiO-66. The highest Q_{st} value of the frameworks in this report was only about 38 kJ mol^{-1}, significantly lower than those of most amine-decorated MOFs. Though not mentioned in the original report, the working capacity of such materials might improve as their heats of adsorption are lower, but it comes at the cost of diminished framework CO$_2$ capacity. In order to stoichiometrically load new metal cations in MOFs, a new PSM strategy to exchange metal ions in a chromium-based MOF, porph@MOM-11 was devised. In porph@MOM-11, cationic porphyrin linkers serve as the pore walls.[207] Simple immersion of porph@MOM-11 into methanol (MeOH) solutions of different metal chlorides gave four PSM derivatives with different metal site occupancies. Due to the reduced pore sizes and the introduction of Cl$^-$ and metal ions, the CO$_2$ volumetric uptake capacities (at 273 K and 1 atm) and Q_{st} values of each of the PSM variants were improved by 3.1–14.5% and 6.6–36.0%, respectively, in comparison to those of porph@MOM-11.

Apart from modification and exchange of metal centers, modification, insertion and exchange of the organic linkers in MOFs can also enhance the interactions between frameworks and CO$_2$. Organic linkers can be post-synthetically modified to introduce diverse CO$_2$-philic moieties.[208–210] For example, alkylamines were tethered to Cr-MIL-101-SO$_3$H through a simple Brønsted acid–base reaction.[208] The resultant Cr-MIL-101-SO$_3$H-TAEA (TAEA = tris(2-aminoethyl)amine) had a high CO$_2$ uptake capacity of 2.3 mmol g^{-1} at 150 mbar and 313 K, and 1.1 mmol g^{-1} at 0.4 mbar and 293 K. The Q_{st} value as calculated from a triple-site Langmuir model was 87 kJ mol^{-1} at zero coverage, indicating strong chemisorption of CO$_2$ in Cr-MIL-101-SO$_3$H-TAEA. UiO-66-allyl was also subjected to a plethora of post-synthetic functionalization reactions.[209] Amongst the modified UiO-66 analogues, the amino alcohol-decorated MOF (UiO-66-aminoalcohol) exhibited the highest CO$_2$ uptake capacity (11.6 mmol g^{-1} at 308 k and 20 bar), while only a negligible amount of N$_2$ was adsorbed under the same conditions, suggesting that UiO-66-aminoalcohol could be a promising candidate for CO$_2$/N$_2$ gas separation.

Insertion of organic linkers emerged as the second PSM technique with a goal of incorporating new organic linkers of similar or identical length, but bearing CO$_2$-phillic moieties in MOFs.[211,212] A bridging linker was post-synthetically incorporated into a MOF by a single crystal to single crystal (SCSC) transformation.[211] By inserting a 3,6-di(4-pyridyl)-1,2,4,5-tetrazine (bpta) linker into the zinc-based MOF, SNU-30, the honeycomb-like pores were divided into smaller channels along the *ab* plane of the framework, yielding SNU-31. This PSM
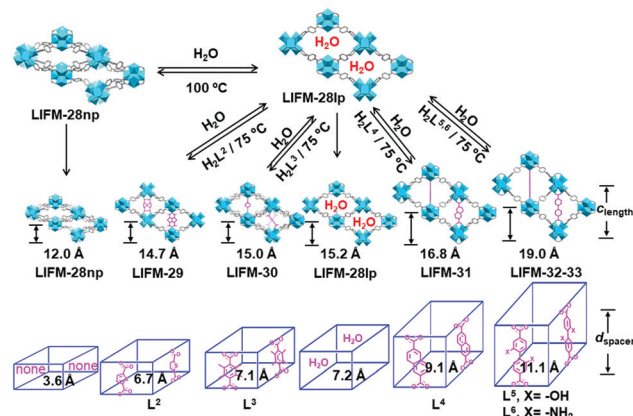

Fig. 8 (top) Reversible breathing behavior of LIFM-28 (LIFM-28np ↔ LIFM-28lp), and (middle) stepwise installation/removal of spacers (L^2–L^6) in an increasing expansion sequence to give LIFM-29–33. Each MOF in the series is composed of Zr SBUs (cyan polyhedra) linked together by organic linkers (gray lines). The spacers are highlighted in pink lines. (bottom) Simplified MOF structures for this series highlighting the role of organic spacers. Color code: C, gray; O, red; and Zr, cyan. H and F atoms are omitted for clarity.

slightly decreased the framework's void volume from 82.1% to 76.1%. Gas adsorption isotherms showed that N$_2$, H$_2$, CH$_4$ and CO$_2$ capacity of SNU-30 could reach up to 7.04 mmol g^{-1} (77 K, 1 bar), 16.2 mmol g^{-1} (77 K, 61 bar), 0.23 mmol g^{-1} (298 K, 1 bar), and 1.16 mmol g^{-1} (298 K, 1 bar), respectively. In contrast to SNU-30, SNU-31 displayed almost no adsorption capacity for N$_2$, H$_2$, and CH$_4$, whereas it exhibited moderate CO$_2$ uptake (0.6 mmol g^{-1} at 1 bar) at 298 K. Another interesting example was found in the incorporation of five distinct linkers into a flexible MOF using a post-synthetic variable-spacer installation strategy (Fig. 8).[212] Unlike the effects observed in rigid frameworks, the structural flexibility of LIFM-28 enabled the material's pore size to be finely tuned by the insertion of organic linkers with various lengths and substituents.[212] The resultant MOFs had functionalized pore environments, and improved thermal stabilities and BET surface areas. Due to these alterations, the CO$_2$ adsorption capacity and selectivity were greatly enhanced. The –NH$_2$ groups in LIFM-33 endowed it with the highest CO$_2$ uptake capacity (3.6 mmol g^{-1}) with a high Q_{st} of about 40 kJ mol^{-1} based on the presence of strong NH$_2$–CO$_2$ interactions. The IAST calculation revealed that the CO$_2$/N$_2$ adsorption selectivity in LIFM-33 was about 30, demonstrably higher than that of parent MOF.

Linker exchange can also regulate MOFs' CO$_2$ capture performance while maintaining their crystallinity, stability, and porosity.[213–215] A family of water-stable UiO-66-AD$_n$ frameworks modified by diverse flexible alkanedioic acids ((HO$_2$C(CH$_2$)$_{n-2}$CO$_2$H), n = 4, 6, 8 and 10) was reported.[213] ^{1}H NMR spectra of digested MOFs demonstrated that the degree of linker substitution increased as the hydrocarbon chain in the substituting organic linker was elongated. Each terephthalate ligand of UiO-66 was substituted by two alkanedioic acid. Among the investigated frameworks, UiO-66-AD6 had the highest CO$_2$ uptake capacity and CO$_2$ desorption free energy due to the relatively strong

2796 | Chem. Soc. Rev., 2019, 48, 2783–2828

This journal is © The Royal Society of Chemistry 2019

interactions between CO_2 and the carboxyl groups of the flexible alkanedioic acid linker which was similar in length to the BDC linker of UiO-66. In this case, the linkers could also be replaced by metalated-ligands.[214] The exchange process was carried out by incubating UiO-66 in aqueous solutions of 1,2,4,5-benzenetetracarboxylic acid (BTEC) or mellitic acid (MA) and various alkaline hydroxides, including LiOH, NaOH, and KOH. UiO-66-(COONa)$_2$-EX exhibited the highest CO_2/N_2 selectivity (33.3) while UiO-66-(COOLi)$_4$-EX had the highest CO_2 adsorption capacity (0.7 mmol g^{-1} at 0.15 bar and 298 K). The authors attributed these effects to the mutual influence of the cations' polarizing abilities and reduced pore sizes.

With respect to ionic MOFs, CO_2 adsorption properties can be regulated by cation exchange.[216–219] A series of cation-exchanged ionic MOFs were prepared by soaking Bio-MOF-1 in DMF solutions of tetramethylammonium, tetraethylammonium, or tetrabutylammonium.[216] Despite the observation of decreased BET surface areas and pore volumes in each cation-exchanged MOF, their CO_2 capacities and Q_{st} values improved compared to the parent Bio-MOF-1. This was attributed to strong interactions between CO_2 and the newly-inserted ammonium cations. The same team also exchanged the cations of Bio-MOF-1 with a series of guanidinium derivatives.[217] When a guanidinium derivative with a high population of LBSs, diaminoguanidinium (DiAmGND$^+$), was exchanged into bio-MOF-1, the MOF's CO_2 adsorption capacity and Q_{st} increased to 5.1 mmol g^{-1} (at 273 K and 1 bar) and 29.4 kJ mol^{-1}, respectively. This was accompanied by only a slight decrease in both the pore volume and BET surface area of DiAmGND@bio-MOF-1. The authors speculated that the enhanced CO_2 uptake performance could be ascribed to the CO_2 affinity of aminated cations rather than the decreased pore size. It was demonstrated that Li$^+$ exchange in an anionic MOF, [H$_2$N(Me)$_2$]$_2$[Zn$_5$(L)$_3$]·5.5DMF·3.5H$_2$O (L = 3,3′,5,5′-biphenyl-tetracarboxylic acid), can be accomplished by SCSC transformation.[218] Impressively, both the guest H$_2$N(Me)$_2^+$ counterions located in the pores and some coordinated metal ions (Zn^{2+}) of the MOF were replaced by Li$^+$, resulting in a greatly increased BET surface area (from 342 to 1664 m^2 g^{-1}) and CO_2 adsorption capacity (from 1.7 to 6.6 mmol g^{-1} at 273 K and 1 bar).

2.2.2. MOF composites. Although a demonstrably powerful technique, post-synthetic modification of MOFs requires OMSs, specific functional groups on the organic linkers, and/or sufficiently large pore apertures to allow for guest or reagent diffusion. The question then becomes, how can one improve the CO_2 capture performance of MOFs lacking these features? An alternative strategy, the formation of MOF composites by accommodating various guest species or combining with other materials such as polymers or ILs can enhance the CO_2 adsorption capabilities of MOFs lacking such features. The CO_2 uptake capacities of the resultant MOF composites are typically significantly greater than those of the parent MOFs due to the generation of new pore environment(s), additional interactions at the interface between phases, and/or affinity of CO_2 to the guest(s). Moreover, the plasticity and chemical stability of certain compounds utilized in the formation of MOF composites can lead to enhanced stabilities and mechanical properties of the

resultant materials, expanding the range of practical applications. To date, four classes of materials, including small molecules,[220–222] polymers,[223–226] two-dimensional (2D) materials,[227–234] and three-dimensional (3D) materials,[235–237] have combined with MOFs in order to tune their CO_2 adsorption properties.

CO_2 is highly soluble in many liquid-phase small molecules, including ILs. Therefore, many experiments and computational simulations have been conducted to explore the applicability of IL-MOF composites to CO_2 capture, separation and purification.[220–222,238,239] For example, the theoretical CO_2 separation performance of several room temperature ionic liquid (RTIL)–MOF composites was evaluated. In the study, 1-ethyl-3-methylimidazolium [EMIM$^+$] salts were incorporated in HKUST-1.[239] At low pressures, the CO_2 uptake capacities, CO_2/CH_4 and CO_2/N_2 selectivities were significantly enhanced upon incorporation of RTILs due to the strong chemisorption of "dissolution" of CO_2 in such compounds. The successful incorporation of 1-n-butyl-3-methylimidazolium hexafluorophosphate ([BMIM][PF$_6$]) into a zeolitic imidazolate framework, ZIF-8, led to a [BMIM][PF$_6$]/ZIF-8 composite.[220] The researchers then investigated the composite's gas adsorption performance using a wide array of experiments, atomically detailed simulations, and DFT calculations. Although the gas adsorption capacity of [BMIM][PF$_6$]/ZIF-8 was attenuated compared to the pristine ZIF-8, the selectivities (CO_2/CH_4 and CO_2/N_2, in 50/50 v/v mixtures) of the composite were more than twice as high than those of the parent ZIF-8 at low pressures. Such work indicated that incorporation of ILs in MOFs can yield materials that exhibit strong, preferential interactions with CO_2.

In the context of MOF composite formation, polymers possess various unique attributes such as softness and high stability. These properties facilitate integration with MOFs. Among them, polyethyleneimine (PEI), a polymer with repeating amine groups and two aliphatic carbon (CH_2CH_2) spacers, has been incorporated in MOFs to augment both the strength and number of adsorbent–CO_2 interactions. The numerous amine sites, commercial availability, and low volatility relative to low-molecular weight amines such as monoethanolamine make PEI an ideal candidate for MOF composite formation. A series of PEI-decorated MOFs were prepared with various amounts of PEI using a wet impregnation method.[223] In the resultant composites, low molecular-weight linear PEI was tethered onto the exposed Cr^{3+} centers of MIL-101. This left other amine groups available to interact with CO_2. As expected, the BET surface areas and pore volumes of the MOF composites dramatically decreased compared to the parent MIL-101 due to pore occlusion. However, the CO_2 adsorption capacities of the PEI-MIL-101 samples were significantly enhanced between 0–2 bar. When the PEI loading was increased to 100 wt%, the CO_2 uptake capacity of the resultant composite (PEI-MIL-101-100) was over 12 times greater (4.2 mmol g^{-1} at 298 K and 0.15 bar) than that of pristine MIL-101. Additionally, the CO_2/N_2 selectivities (in a 15/75 v/v mixture) of PEIMIL-101-100 and PEI-MIL-101-125, with 100 and 125 wt% PEI loading, respectively, at 25 °C were as high as 120 and 150, respectively. Given the ease with which small MOF particles can be loaded with PEI and the fact that branched PEI possesses more-nucleophilic
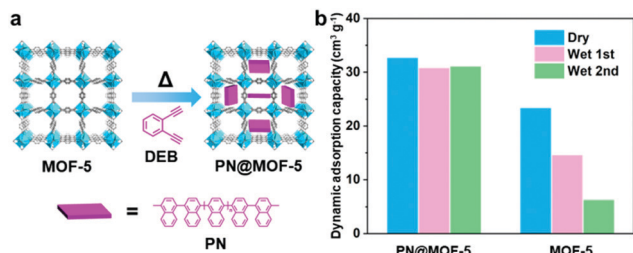
This journal is © The Royal Society of Chemistry 2019

Chem. Soc. Rev., 2019, **48**, 2783–2828 | 2797

Fig. 9 (a) Polymerization of 1,2-diethynylbenzene (DEB) in the pores of MOF-5 to give PN@MOF-5 (PN = polynaphthylene, pink plate). Color code: C, gray; O, red; and Zn, cyan. H atoms are omitted for clarity. (b) Dynamic CO_2 adsorption capacities of PN@MOF-5 and MOF-5 under dry conditions and in the presence of water (RH = 65%).

Fig. 10 Synthesis of covalently-linked MCGr-*X* composites (M = Mg^{2+}, Ni^{2+} or Co^{2+}, X = 0, 2, 5, and 10 wt%). (I) Benzoic acid functionalized graphene (BFG). (II) *In situ* growth of M-MOF-74 (M = Mg^{2+}, Ni^{2+} or Co^{2+}) crystals on the graphene basal plane. (III) Graphene reinforced MCGr-*X* composites. (IV) Hexagonal (*ca.* 1.1 × 1.1 nm²) 1D channels of M-MOF-74. Color code: C, red; O, blue; H, white; and M (Mg^{2+}, Ni^{2+} or Co^{2+}), cyan. Adapted from ref. 227 with permission from Wiley-VCH, copyright 2016.

primary amines (–NH₂) as opposed to the secondary amine groups (–NH–) present in linear PEI, the former was impregnated into MIL-101 crystals about 150 and 300 nm in size.[224] Each composite exhibited an exceptionally high CO_2 uptake capacity at 0.15 bar and 298 K. However, the performances of the small MOF composites (with higher PEI loadings) were slightly worse than those of the large one, likely due to inner pore inaccessibility.

Polymers trapped within the channels of MOFs can also serve to partition the pore spaces. Recently, a hydrophobic MOF–polymer composite, PN@MOF-5 (PN = polynaphthylene), was fabricated (Fig. 9a).[225] As the PN loading increased, the number of 0.6 nm diameter pores drastically increased with a simultaneous decrease in the amount of 1.2 nm pores (the pore size of MOF-5). This indicated that the channels of MOF-5 were partitioned by incorporation of the PN polymer. As expected, the CO_2 uptake increased from 1.7 mmol g⁻¹ (MOF-5) to 3.5 mmol g⁻¹ (PN@MO-5) at 273 K and 760 Torr. Most importantly, the stability of PN@MOF-5 under humid conditions was significantly greater than that of MOF-5, which is typically unstable in water or humid air. The dynamic CO_2 adsorption capacity of the hydrophobic composite under humid conditions was nearly identical to that of the composite under dry conditions (Fig. 9b).

MOF composites can also be prepared by growing MOFs on the surface or within the pores of other materials. Some 2D materials such as graphene, graphene oxide, layered double hydroxides and aminoclays can be used as substrates for the growth of MOF composites because their surfaces can be functionalized and/or they frequently possess diverse, reactive functional groups. Several benzoic acid-functionalized graphene/M-MOF-74 composites, MCGr-*X* (M = Mg^{2+}, Ni^{2+} or Co^{2+}, X = 0, 2, 5, and 10 wt%), were synthesized in which the graphene basal planes acted as supports to reinforce the MOF matrices (Fig. 10).[227] Interestingly, the CO_2 adsorption capacity of each MCGr-*X* composite was enhanced relative to that of the corresponding pristine MOF. As the most striking example, MgCGr-10 adsorbed 8.1 mmol g⁻¹ CO_2 at 1 atm and 298 K. Since the composite exhibited similar BET surface areas and pore volumes to the pristine MOF, the increased CO_2 uptake capacity and selectivity of the composite were attributed to dispersive forces between the π electron cloud of graphene and quadrupole moment of CO_2. Moreover, mechanical property

measurements such as nanoindentation revealed that both the hardness and elastic modulus of each MOF increased upon graphene introduction, which would undoubtedly be favorable with respect to practical technological application of MOFs and MOF-based materials. Two-dimensional (2D) materials can also act as substrates or templates during the construction of MOF composites. For example, an HKUST-1–graphene oxide composite in which the oxygen-containing functional groups from the graphene oxide (GO) acted as seed sites for crystallization and dispersion of HKUST-1 nanocrystals.[228] Interestingly, the defects in the GO layers inhibited the growth of the MOF nanoparticles (NPs). As such, the HKUST-1 crystallites were relatively small (10–40 nm). Although GO is not intrinsically porous, the composite exhibited both an augmented porosity (BET surface area, 1532 m² g⁻¹) and CO_2 uptake (8.3 mmol g⁻¹ at 273 K and 1 atm) compared to the original HKUST-1 (BET surface area of 1305 m² g⁻¹, CO_2 uptake of 6.4 mmol g⁻¹ at 273 K and 1 atm). The authors attributed this to the improved gas accessibility of the well-dispersed nano-MOF crystallites. Another example of 2D material MOF composite templation was reported in the application of highly water-dispersible aminoclay (AC) sheets to the synthesis of HKUST-1–AC composites.[229] The amine functional groups in the AC served as metal binding sites for the stabilization of Cu^{2+} ions, which lead to decreased aggregation of HKUST-1 crystallites during the growth process. Therefore, the resultant MOF composites were decorated with ultra-small (2–3 nm) HKUST-1 NPs. The BET surface area and CO_2 uptake capacity values for the HKUST-1–AC composite were 1381 m² g⁻¹ and 8.1 mmol g⁻¹ (at 273 K and 1 bar), respectively, representing increases of 70% and 39%, respectively, over the reported values for HKUST-1. These enhancements could potentially stem from the formation of new voids at the interface of HKUST-1 NPs and the AC layers. This strategy was adapted to other systems, including aminated graphite oxide,[230,231] suggesting its potential universality.

It is important to note, however, that many 2D materials do not exhibit high surface areas. As an alternative, many three dimensional (3D) materials (and even some one dimensional [1D] materials) have moderate to high porosities and can be beneficial for MOF composite formation based on their potential miscibility with MOFs. A representative example is found in the incorporation of carbon nanotubes (CNTs) into HKUST-1 to give a CNT hybrid composite CNT@HKUST-1.[240] The carboxylate groups of the CNTs acted as nucleation sites to support continuous growth of HKUST-1. This crystal growth was beneficial for thorough removal of guest molecules during activation, leading to an enhanced composite pore volume (from 0.73 to 0.87 cm^3 g^{-1}). The CO_2 isotherm revealed that the adsorption capacity of CNT@HKUST-1 was 13.5 mmol g^{-1} at 298 K and 18 bar, about twice as high as that of HKUST-1 under the same conditions. Additionally, crystal growth confinement in the mesopores or macropores of templates can lead to smaller MOF particle sizes than those of MOFs synthesized *via* the *de novo* process.[235,236] Typically, smaller MOF crystals can be more easily and efficiently activated, which is naturally beneficial with respect to gas adsorption as active sites and pore volumes are more easily accessible in properly evacuated materials. Finally, due to the discrepancies between the pore diameters of MOFs and other materials, the pore size distributions of composite materials can fall within a wide range, thus potentially improving CO_2 adsorption and selectivity.[241]

2.3. Challenges and opportunities in developing MOFs for CO_2 capture

Remarkable advances have been made toward CO_2 capture and separation in MOFs and MOF-based materials. In contrast to many other porous materials, MOFs have both high CO_2 capacities and outstanding CO_2 selectivities for capture in the presence of other gasses. This largely stems from MOFs' unique properties such as structural flexibility, the potential for framework post-synthetic modification, and relatively facile composite formation. Many of these strategies have only recently been developed and further optimization promises to improve MOFs' CO_2 capture properties as more work is performed. However, many challenges regarding the preparation and application of MOFs with high CO_2 capture capacities remain unaddressed. For example, many MOFs still have low CO_2 selectivities in the presence of moisture/water/acidic gasses, even if their overall adsorption capacities are high. Additionally, under these conditions, many MOFs chosen for studies lack the requisite stability for practical application. In the future, it would be necessary to choose MOFs which are known to have high chemical and thermal stability, as found for MOF-808.[242,243] In this context, it is important to recall that CO_2 capture from large stationary sources such as the flue gas of power plants is regarded as one of the most promising avenues to mitigate rising atmospheric CO_2 concentrations. Generally, flue gas from power plants (CO_2 point sources) is composed of 15–16% carbon dioxide, 5–7% water vapor, 73–77% nitrogen, 3–4% oxygen and traces of acidic gasses such as H_2S, NO_x, SO_x.[109] Consequently, during adsorption, gasses with higher polarities and/or binding energies such as H_2O or acidic gasses are preferentially adsorbed over CO_2 on the OMSs

of MOFs. This has to be considered when selecting a MOF for CO_2 capture in the presence of water. Many pre- and post-synthetic strategies have been developed for improving the water and acid stabilities of those MOFs already under consideration.[34,225,243–246] Nevertheless, there are suites of MOFs as yet uninvestigated which may well be more appropriate for this application. Additionally, certain strategies can be accompanied by new issues such as dramatic reduction of the materials' specific surface areas and/or pore volumes. These issues are beginning to be addressed as we learn how to balance functionalization with maintaining crystallinity and porosity. Finally, for many MOFs, direct capture of CO_2 at low partial pressures remains a challenge due to relatively weak CO_2-framework interactions. Although CO_2 adsorption capacities at low partial pressures can be improved by introducing CO_2-philic moieties on MOFs' organic linkers, adsorbent regeneration energies also typically sharply increase.[199,208] This can, of course be overcome by precisely tuning the chemistry between the frameworks and CO_2. In the future, it is likely that high stability and high CO_2 adsorption capacity will be targeted in order to position MOFs as the next-generation of materials for practical CO_2 capture.
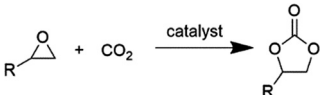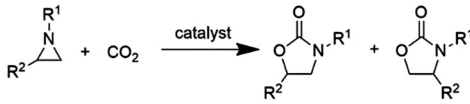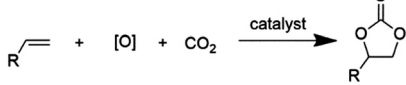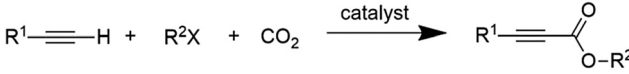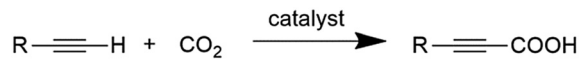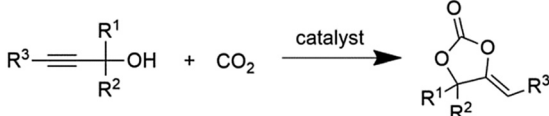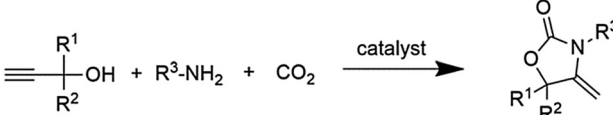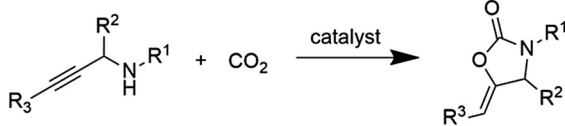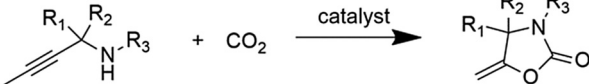
3. MOFs for catalytic CO_2 conversion

The modular, tunable, and porous nature of MOFs make them ideal candidates for heterogeneous catalysis. In particular, catalytic CO_2 conversion has been a target. In addition to MOFs, many MOF composites and MOF derivatives have been reported as efficient CO_2 conversion catalysts. In MOF composites, additional components are hypothesized to serve as new active sites and/or cooperative agents. This chemically emphasizes the respective functional advantages of both MOFs and the added components. MOF composites are typically more stable than the parent MOF(s), leading to improved recyclability and turnover. This area of CO_2 conversion using MOFs is nascent and requires more fundamental studies dealing with reactivity, optimization of performance, study of the long-term properties of the materials, and cyclability. When utilized as templates or precursors, stable MOF derivatives can be obtained. To a large degree, MOF-derived porous materials are able to inherit the salient properties of pristine MOFs, such as high surface area, tailorable porosity, adjustable morphology, and compositional diversity. Additionally, the process of pyrolyzing MOF composites has the potential to create additional active sites, improved conductivity and other important structural and chemical features which are not present in the parent frameworks. Therefore, many MOF-derived porous materials have the potential to affect enhanced CO_2 transformation in comparison to their parent MOF analogues. In this section, we describe CO_2 conversion reactions performed using MOF-based catalysts, mainly focusing on CO_2 organic transformation into organic products, CO_2 hydrogenation, photocatalytic CO_2 reduction, and electrocatalytic CO_2 reduction.

### 3.1. Heterogeneous CO_2 organic transformation

A variety of MOF-based materials have been reported for CO_2 organic transformation. The scope of catalytic CO_2 conversions to organic products has been summarized in Table 2.

Table 2 Summary of CO_2 organic transformation in MOF-based materials

Reaction	Equation	Active site(s)	Ref.
Cycloaddition		Lewis acid, Lewis base, Brønsted acid, organic salt, organic base, *etc.*	109, 150, 155, 247–293 and 311–322
			272, 294 and 295
Olefin oxidative carboxylation		Oxidant, Lewis acid, Lewis base, halide	291–293 and 296
Terminal alkyne carboxylation		Cu(I)	297
		Ag, Pd–Cu NPs	306–310
Propargylic alcohol carboxylic cyclization		Ag(I), Cu(I)	298–300
Three-component carboxylic cyclization of propargyl alcohols, CO_2, and primary amines		Ag(I)	299
Propargyl amine carboxylic cyclization		Ag(I)	299
Terminal propargylamine oxidative cyclization		Amidogen	323

3.1.1. Conversion of CO_2 into organic products using MOFs. MOFs have high CO_2 adsorption capacities and adjustable pore apertures and cavities. Many of the same active sites applied to CO_2 capture, including OMSs or LASs, Brønsted acid sites (BASs) and LBSs, can convert CO_2 into chemical products by organic transformation. This is frequently analogous to the transformations performed by numerous conventional homogeneous and heterogeneous catalysts. The utilization of MOFs' intrinsic functionalities for CO_2–epoxide cycloaddition reactions has been widely explored. This class of reactions can yield products with a variety of applications. Specifically, cyclic carbonates, the major product of many CO_2 cycloaddition reactions, have been widely applied as intermediates for the production of engineering plastics, electrolyte solvents for lithium-ion batteries, polar aprotic solvents, degreasers, and fuel additives.[301,302]

Generally, the mechanism of MOF-based CO_2 epoxide cycloaddition involves coordination of an epoxide oxygen atom with a LAS and/or a BAS in a MOF-based material (Scheme 2). This coordination polarizes the C–O bond which is then heterolytically cleaved with concurrent nucleophilic attack of the less
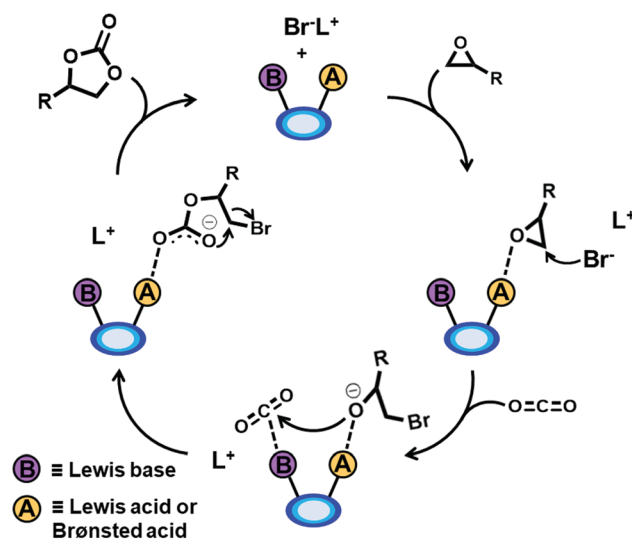
Scheme 2 Proposed mechanism for CO_2–epoxide cycloaddition in MOFs and related materials involving Lewis acidic, Brønsted acidic, and/or Lewis basic sites, in the presence of cocatalytic TBAB (Br^-L^+).

2800 | *Chem. Soc. Rev.*, 2019, **48**, 2783–2828

This journal is © The Royal Society of Chemistry 2019

sterically hindered carbon atom of the epoxide by a co-catalyst-based halide anion (a typical co-catalyst is tetrabutylammonium bromide, TBAB) to form a halo-alkoxide intermediate. Subsequently, the CO_2 carbon atom, which is frequently activated by LBSs through dipolar interactions, is nucleophilically attacked by the ring-opened alkoxide intermediate and the cyclic carbonate is obtained by intramolecular ring-closure, regenerating the catalyst and co-catalyst. Interestingly, some MOFs can exhibit excellent catalytic activities in the absence of co-catalyst.[247–255] Unfortunately, on account of the limited types and relatively low activities of active sites in the MOFs studied for this application, as well as the intrinsic inertness of CO_2, high temperatures and/or pressures must inevitably be applied in these cases. In this context, several strategies for improving the catalytic activities of MOFs towards CO_2 cycloaddition reactions have been developed. Above all, it is inferred that the natures, quantities and locations of the active sites have enormous impacts on the catalytic efficiencies of the materials.

To support this inference, numerous reports exist. In one case, a porous 3D framework, $[(Zn_4O)_2(Zn_2)_{1.5}(L)_6(H_2O)_3]$ (H_3L = 10-(4-carboxy-phenyl)-10H-phenoxazine-3,6-dicarboxylic acid) in which the parent Zn(II) ions could be partially exchanged by Cu(II) and Co(II) ions was reported (Fig. 11a).[256] Upon post synthetic exchange, no obvious enhancement was observed in any of the frameworks' BET surface areas, pore volumes, or CO_2 adsorption capacities. However, the yield of the propylene oxide–CO_2 cycloaddition product, propylene carbonate, was dramatically reduced from 99% in the zinc MOF to 50% in the cobalt analogue and 32% in the copper MOF (Fig. 11b).
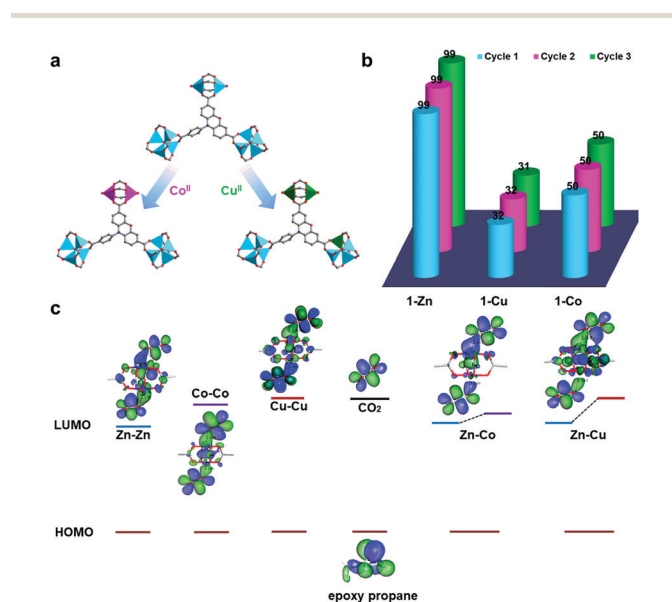

Fig. 11 (a) Illustration of fragmental cluster change via metal cation exchange in the Zn clusters (cyan polyhedra) of $[(Zn_4O)_2(Zn_2)_{1.5}(L)_6(H_2O)_3]$ (H_3L = 10-(4-carboxy-phenyl)-10H-phenoxazine-3,6-dicarboxylic acid). Color code: C, gray; O, red; N, blue; Zn, cyan; Cu, green; and Co, pink. H atoms are omitted for clarity. (b) Comparison of propylene carbonate yields using different MOF catalysts for up to three cycles. (c) LUMO orbital of CO_2 adsorbed on MOFs with different metal centers during the catalytic process. Adapted from ref. 256 with permission from Wiley-VCH, copyright 2016.

Since the post-synthetic metal exchange process mainly occurred at the dimeric paddlewheel ($Zn_2(COO)_4$) SBUs, the tremendous difference between the catalytic activities of these MOFs was mainly attributed to the presence or absence of various metal species. Molecular dynamics (MD) simulations indicated that CO_2 cycloaddition reactions are limited by the energy gap between the highest occupied molecular orbital (HOMO) of the epoxides and the lowest unoccupied molecular orbital (LUMO) of CO_2. Upon CO_2 binding to an OMS, a decrease of LUMO energy is observed, reducing the energy gap and accelerating the reaction. The simulations ultimately demonstrated that the energy gap between the LUMO of CO_2 and the epoxide's HOMO increases in the order of Zn–Zn < Zn–Co < Zn–Cu < Co–Co < Cu–Cu (Fig. 11c), which was in accordance with experimental results and reflected the effect of the nature of the active sites on the catalytic capabilities of MOFs. As further evidence, it was discovered that the catalytic efficiency of a Hf-based MOF (Hf-NU-1000) for the cycloaddition reaction of CO_2 with styrene oxide (SO) was superior to that of the Zr-based NU-1000 under the same reaction conditions.[257] The typical dissociation enthalpy of typical Zr–O bonds in NU-1000 is 776 kJ mol^{-1}. In contrast, the dissociation enthalpy of Hf–O bonds of Hf-NU-1000 is relatively high (802 kJ mol^{-1}), leading to the higher oxophilicity of Hf in NU-1000's SBUs, enhancing the Brønsted acidity and thus the catalytic activity of Hf-NU-1000.

With respect to the quantity and position of active sites, an interesting example is found in the *nbo* framework MMCF-2. This compound, which is isoreticular to MOF-505, was synthesized from 1,4,7,10-tetrazacyclododecane-N,N',N'',N'''-tetra-p-methylbenzoic acid (H_4tactmb), yielding a framework containing a high density of well-oriented LASs.[258] In contrast to MOF-505's [1,1′-biphenyl]-3,3′,5,5′-tetracarboxylic acid (H_4bptc) linker, the azo macrocycles of H_4tactmb acted as copper chelating agents. Therefore, six center-oriented copper sites were added within the cuboctahedral cage of MMCF-2, resulting in a 50% increase of the amount of LASs in MMCF-2. Based on this increase in the quantity of active sites, MMCF-2 displayed a remarkably increased catalytic activity (95.4% yield) for the cycloaddition of propylene oxide (PO) and CO_2 in the presence of a co-catalyst under mild reaction conditions (room temperature and 1 atm CO_2 pressure). This activity surpassed both MOF-505 (48.0%) and HKUST-1 (49.2%) and was mainly attributed to the higher density of preferentially-oriented active sites (LASs) in the framework that promoted interactions with substrates (PO). To improve MOFs' reactivities for CO_2 cycloaddition reactions, salen-, porphyrin- and 2,2′-bipyridine-containing organic linkers can also serve as metal chelating agents to diversify and increase the quantities of metal active sites in MOFs.[259–261,286] As an example, a multi-component MOF, PCN-900(Eu), fabricated from a combination of Eu_6 clusters, tetratopic porphyrinic linkers, and linear linkers can be modified by post-synthetic exchange of the latter and/or metalation of the former linkers to form three isoreticular compounds, PCN-900(Eu)-BPYDC, PCN-900(Eu)-CoTCPP, and PCN-900(Eu)-CoTCPP-CoBPYDC.[261] With the highest density of LASs (Eu^{3+} and Co^{2+} ions), PCN-900(Eu)-CoTCPP-CoBPYDC exhibited the highest catalytic activity for the

CO$_2$–PO cycloaddition reaction under mild conditions, surpassing that of the non-metalated counterpart (PCN-900(Eu)-BPYDC) or the partially metalated framework (PCN-900(Eu)-CoTCPP).

Taking advantage of synergetic effects between multiple active sites can also boost the catalytic efficiencies of MOF catalysts for CO$_2$ cycloaddition reactions. Specifically, Lewis acid–Lewis base synergy,[109,249,253,255,272,279,280] Lewis acid–Brønsted acid synergy,[155,264–268,291] Lewis acid–Lewis acid synergy,[256,261,286] and Lewis acid–Brønsted acid–Lewis base synergy[270] have been studied for this series of reactions. Employing 2,4-bis(3,5-dicarboxyphenylamino)-6-ol triazine (H$_4$BDPO) as an organic linker has led to the synthesis of a stable Cu(II)-based MOF, JUC-1000, in which the phenol, amino, and triazine groups serve as weak acids and/or bases. This combination of acidic and basic moieties in one material improved the MOF's chemical stability due to the presence of –O$^-$/–OH, –NH–/–NH$^+$– and –N$=$/–NH$^+$$=$ pairs facilitating a so-called "buffering effect".[270] The synergy between multiple catalytic sites in JUC-1000, including open Cu(II) metal sites (LASs), phenol hydroxyl groups (BASs), and the LBSs from both the –NH– and triazine groups, allowed the system to produce propylene carbonate in 96% yield under ambient conditions with the aid of a co-catalyst. The authors speculated that the epoxides were synergistically activated by the open Cu(II) Lewis site, and the –OH and –NH– functional groups from the organic linkers by dipolar interactions and/or hydrogen bonding. Additionally, the CO$_2$ molecules were activated upon adsorption, as facilitated by the LBSs located in the pores.

Nevertheless, high-densities of active sites and synergetic behavior between them doesn't always translate to excellent catalytic performance in MOFs. Interactions between the substrates and active sites as well as the facile transport of reactants and products also play crucial roles in epoxide conversion reactions. A combination of Ni(NO$_3$)$_2$·6H$_2$O, tetrakis(4-carboxyphenyl)ethylene (H$_4$TCPE), and L-proline (L-Pro) was used to form two new (4,4)-network, Ni(II)-based MOFs, Ni-TCPE1 and Ni-TCPE2, that were hypothesized to catalyze CO$_2$–epoxide cycloaddition.[271] In contrast to the 1D quadrilateral channels (17.9 × 17.9 Å^2) present in Ni-TCPE2, Ni-TCPE1 possesses large single-walled nanotubes (exterior wall diameter: 3.6 nm; interior channel diameter: 2.1 nm), liberating active sites within the framework and facilitating the transfer of both substrates and products. In this context, although both MOFs possessed an identical amount of OMSs, a total turnover number (TON) of 17 500 per mole of catalyst after 10 repetitions of the reaction (32.5 h) was obtained when using Ni-TCPE1, whereas it took over 70 h for Ni-TCPE2 to achieve the same value. As an unfortunate drawback, the utilization of a homogeneous halide co-catalyst cannot be avoided in most of the approaches detailed above. This serves to complicate the implementation, and increase the costs of these catalytic systems.[254] As an alternative approach, such co-catalysts can be immobilized onto MOFs' backbones using pre- or post-synthetic modification, opening new pathways toward the realization of truly heterogeneous catalytic systems. As a very early example of such tethering, a co-catalyst-functionalized MOF (F-IRMOF-3) was made by nucleophilic substitution of the amine groups of IRMOF-3 using methyl iodide.[249] The yield
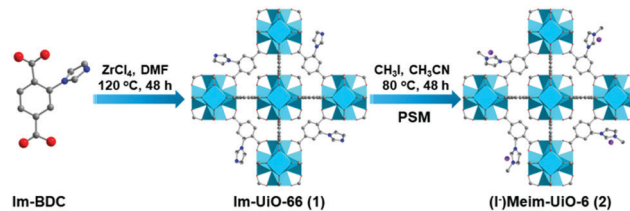

Fig. 12 Solvothermal synthesis of Im-UiO-66 (1, middle) composed of Zr$_6$ clusters (turquoise polyhedra) and Im-BDC linkers (left) followed by subsequent PSM using CH$_3$I to give (I$^-$)Meim-UiO-66 (2, right). Color code: C, gray; O, red; N, blue; Zr, cyan; and I, purple. H atoms are omitted for clarity.

of propylene carbonate (PC) produced by F-IRMOF-3 quickly increased to 98% in 1.5 h from 2% in unfunctionalized IRMOF-3 (5 h). Also, a similar process was used to synthesize a bifunctional imidazolium decorated UiO-66 variant, (I$^-$)Meim-UiO-66, (Fig. 12).[254] Taking advantage of the coexistence of BASs (Zr-OH/Zr-OH$_2$) and LBSs (I$^-$), (I$^-$)Meim-UiO-66 exhibited fantastic catalytic activity for the cycloaddition of epichlorohydrin (ECH) and CO$_2$ under relatively mild conditions (120 °C and 1 atm CO$_2$), with a yield of 93%. Furthermore, due to the heterogeneous nature of the catalyst, no significant loss of catalytic activity was observed during six sequential reaction trials. Most significantly, each subsequent trial could be conducted without the addition of any halide co-catalyst. Therefore, one can conclude that in order to achieve efficient catalytic CO$_2$ cycloaddition under mild conditions, it is desirable to construct MOFs possessing a large number of accessible active sites, large pores, synergistic effects between multiple active sites, and organic linker-tethered halide ions.

As analogues to epoxides, aziridines, a class of three-membered heterocyclic compounds with one amine group, can be converted to oxazolidinones, a versatile class of compounds commonly applied as antimicrobial agents. Such a reaction was reported in a 3D Zn(II)-MOF (ZnGlu) synthesized from glutamate and zinc sulfate heptahydrate.[272] Utilizing LASs (Zn^{2+}), LBSs (–NH$_2$), and a TBAB co-catalyst, about 90% of 2-methylaziridine was converted to 4-methyloxazolidin-2-one at room temperature under 1 MPa of CO$_2$, with a high selectivity of 99%. As an additional example, tetrakis-3,5-bis[(4-carboxy)phenyl]phenyl porphine (H$_{10}$TBCPPP) was used as an organic linker to synthesize a copper porphyrin-based MOF.[294] At room temperature, under 1 bar of CO$_2$ pressure, the MOF converted 1-methyl-2-phenylaziridine to 3-methyl-5-phenyl-2-oxazolidinone with a moderate yield of 63%, higher than that of HKUST-1 (47%) under similar reaction conditions. The amplified catalytic performance of the copper porphyrin based MOF in this study was attributed to the increased accessibility of Lewis-acidic Cu(II) sites.

An alternative CO$_2$ conversion route is found in the oxidative carboxylation of olefins following a two-step process involving the epoxidation of olefins and subsequent epoxide–CO$_2$ cycloaddition. The development of such tandem reactivity in one material is highly desirable and economical due to the availability and potential complexity of the olefin substrates. Unfortunately, oxidative carboxylation of olefins generally requires high CO$_2$ pressures and yields numerous byproducts with low carbonate yields.[292] A zirconium-based MOF, MOF-892, with dual acidic sites
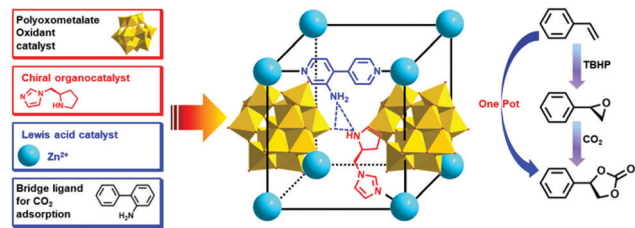
Fig. 13 (left) Synthetic procedure used to form a polyoxometalate-based MOF highlighting the materials' constituents, including the polyoxometalate oxidant catalyst (gold polyhedra), chiral organocatalyst, Lewis acid catalyst (Zn^{2+}, cyan ball), and bridging ligand used to adsorb CO_2. The organic linkers (NH_2-bipyridine) in the MOF are represented as black lines. (right) One pot asymmetric cyclic carbonate formation from the olefin and CO_2 achieved by tandem catalysis.

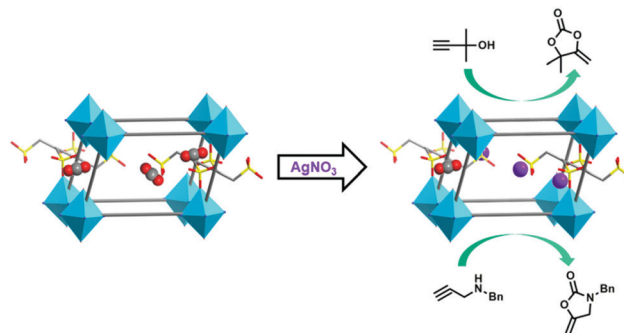**Fig. 14** The Ag(I) metalation of TMOF-3 composed of Zn clusters (cyan polyhedra) and organic linkers (grey lines). (Right, top and bottom) Carboxylic cyclization of propargylic alcohols and propargyl amine using CO_2. The reactions are catalyzed by the Ag(I)-decorated sulfonate-MOF. Color code: C, gray; O, red; N, blue; Zn, cyan S, yellow; and Ag, purple. H atoms are omitted for clarity.

(LASs from Zr(IV) and BASs from uncoordinated carboxylates) was utilized as a catalyst for the one-pot synthesis of styrene carbonate (SC) from styrene and CO_2.[291] Remarkably, in the presence of *tert*-butyl hydroperoxide (TBHP) and TBAB, styrene was completely converted in MOF-892 at 80 °C and 1 atm CO_2 in only 9 h. Furthermore, the reaction was 80% selective for SC with *t*-butanol and benzaldehyde as the major byproducts. Targeting synergistic effects between multiple components, Keggin-type $[ZnW_{12}O_{40}]^{6-}$ anions (oxidant), zinc(II) ions (LASs), NH_2-BPY (LBSs) and pyrrolidine-2-yl-imidazole (PYI, asymmetric organocatalytic groups) were incorporated within a single MOF (Fig. 13).[293] The resultant polyoxometalate-based MOFs exhibited not only excellent CO_2 cycloaddition catalytic efficiency (>99% yield) and high enantioselectivity (90–96% ee) with (R) or (S)-styrene oxide (SO) but could also convert SO into phenyl(ethylene carbonate) in ~4 days with high yield (90–92%) and ee (77–80%) at 50 °C and 0.5 MPa CO_2.

Carboxylation of terminal alkynes, yielding alkynyl carboxylic acids or esters, is also a sought-after CO_2 conversion reaction to which MOF-based materials have been applied. These products are highly significant to pharmaceutical and fine chemical applications.[303,304] Indeed, many catalytic systems have been developed for these reactions.[305] However, most of these systems feature nonporous materials, dramatically hindering mass transport and active site accessibility. Under the assumption that they can more competently affect these terminal alkyne carboxylations, MOFs have been investigated for such reactions. For instance, inspired by the excellent terminal alkyne carboxylation catalytic performance of CuI and the facile conversion of CuI to $[Cu_xI_y]$ under solvothermal conditions, a pair of two cluster-based MOFs assembled from multinuclear Gd-clusters and Cu-clusters ($[Cu_{12}I_{12}]$ or $[Cu_3I_2]$) were made.[297] Both MOFs afforded encouraging yields of *n*-butyl 2-alkynoate (74–80%) as the product of phenylacetylene carboxylation at 80 °C and 1 atm CO_2 pressure in the presence of Cs_2CO_3 and *n*-BuI.

More recently, based on the specific alkynophilicity of silver complexes, a porous silver coordination polymer was synthesized, in which the decentralized silver(I) chains were shown to activate the C≡C bonds of propargylic alcohols and subsequently cyclize them with CO_2.[298] In the presence of this Ag(I)-based MOF and triphenylphosphine (Ph_3P), propargylic alcohols were

converted to the target products ((Z)-5-benzylidene-4,4-dimethyl-1,3-dioxolan-2-one) with excellent yields (>89%) under 0.5 MPa CO_2 and 50 °C within 36 h. Another exciting example is found in the application of an organosulfonate-based MOF, TMOF-3, with a defective *pcu* topology.[299] In this MOF, the missing linker defects were ordered, providing an array of linker-pendant sulfonate groups for post-synthetic Ag(I) metalation (Fig. 14). In the post-synthetically modified material, the sulfonate groups on the organic linkers had a high CO_2 affinity and the Ag(I) ions could activate alkynes. Therefore, the synergy in the resultant framework allowed it to catalyze the carboxylic cyclization of propargylic alcohols in the presence of 1,8-diazabicyclo-[5.4.0]underc-7-ene (DBU) under 0.1 MPa CO_2 pressure at room temperature, with satisfying yields (>86%) for most substrates. Encouraged by the high catalytic performance of the Ag(I) ions towards propargylic alcohol cyclization, the Ag(I)-decorated sulfonate-MOF was also employed to catalyze other two CO_2 conversion reaction, including three-component reactions between propargyl alcohols, CO_2 and primary amines, as well as carboxylic cyclization of propargyl amines with CO_2, yielding oxazolidinones which are significant components of antibiotics. After 15 hours, the Ag(I)-decorated sulfonate-MOF converted propargyl alcohols into oxazolidinone derivatives with high yields (>97%) in the present of Ph_3P under mild reaction conditions. Additionally, upon DBU addition, carboxylic propargyl amine cyclization was achieved under extremely mild conditions (1 atm CO_2 and room temperature) after 6 h, with high yield (>89%). Notably, all these catalytic results were determined by ^1H NMR, as an average value of three runs, indicating their reliability and repeatability.

As previously mentioned, copper based MOFs also show great potential for alkyne activation.[297] By employing 5-amino-nicotinic acid (L5) as the organic linker, a unique, three dimensional, anionic framework, $\{(NH_2C_2H_6)_{0.75}[Cu_4I_4 \cdot (L5)_3 \cdot (In)_{0.75}] \cdot DMF \cdot H_2O\}$, was constructed and applied to the catalysis of carboxylic cyclization of various propargylic alcohols.[300] With the addition of trace triethylamine (TEA), various propargylic alchohols were smoothly converted to the corresponding

This journal is © The Royal Society of Chemistry 2019

Chem. Soc. Rev., 2019, **48**, 2783–2828 | **2803**

products in this MOF without addition of solvent based on the synergistic effect between Cu(I) and In(III) in this heterometallic framework. Not limited to these metal centers, the Lewis basic sites on the organic linkers can also affect chemical transformation of CO_2. As a example, the reaction of an amino tripodal imidazole ligand (N^1-(4-(1H-imidazol-1-yl)benzyl)-N^1-(2-aminoethyl) ethane-1,2-diamine) with Cd(II) ions gave a flexible MOF decorated with $-NH_2$ groups, which exhibited decent catalytic performance for the carboxylative cyclization of propargylamines with CO_2 with desirable TON (9300).[323] The authors speculated that the amidogen ligand played an important role in facilitating ring closure to yield the oxazolidinone derivatives, which was fairly stable under the reaction conditions.

3.1.2. Conversion of CO_2 to organic products using MOF composites. MOFs impregnated with metal oxides, noble metal NPs, and other catalytically active species, also known as MOF composites, have been studied as CO_2 conversion catalysts. As a representative example, $\sim$1.4 nm Ag NPs were incorporated into the cavities of MIL-101 using a liquid impregnation-reduction method to obtain a series of Ag@MIL-101 composites.[306] The resultant materials had excellent CO_2 adsorption capacities and were decorated with unsaturated Cr(III) sites and highly active Ag NPs that were stabilized by MIL-101. The resultant Ag@MIL-101 (4.16 wt% Ag) exhibited remarkable catalytic activity (96.5% yield) and excellent stability over 5 runs of terminal alkyne carboxylation reactions utilizing CO_2 under extremely mild conditions (1 atm CO_2, 50 °C). By employing similar processes, Ag NPs were encapsulated in the pores of MIL-100(Fe) and UiO-66 to give Ag@MIL-100(Fe) and Ag@UIO-66.[307] In the presence of Cs_2CO_3 (base) and DMF (solvent), each MOF composite carboxylated terminal alkynes in good yield (>94%) at 50 °C after 15 h.

MOFs' surfaces can also serve as supports for pre-synthesized metal nanoparticles (MNPs).[69] As examples of this application, monometallic Ag NPs and bimetallic Pd–Cu NPs were separately loaded on the surface of two different MOFs (Co-MOF and MIL-101) for carbon dioxide fixation via terminal alkyne carboxylation.[308,309] Using Cs_2CO_3 as a base, both resultant MOF composites (Ag/Co-MOF and Pd–Cu/MIL-101) displayed high catalytic activities (yield >96%) at room temperature. More recently, an electrostatic attraction strategy was applied to incorporate atomically precise nanoclusters (APNCs) into MOFs.[310] The resultant composite, $Au_{12}Ag_{32}(SR)_{30}$@ZIF-8, not only adsorbed CO_2 but also activated terminal alkynes. Therefore, outstanding catalytic performance in the synthesis of phenylpropiolic acid from CO_2 and phenyl-acetylene under mild conditions (1 atm CO_2 pressure, 50 °C) with a high TON of 18 164 and good recyclability was observed.

MOF composites also play unique roles in CO_2–epoxide cycloaddition reactions.[311–315] Recently, a new strategy to imprison chiral salen(Co(III)) complexes within the pores of IRMOF-3 was developed.[311] The (R,R)-salen(Co(III)) complexes were adsorbed in the pores of IRMOF-3, followed by decoration of the organic linkers with acetic anhydride by PSM. The chiral composite ((R,R)-Salen(Co)@IRMOF-3-AM) gave an acceptable PO conversion of 25% and a PC ee of 21%. Following this, two Salen-Cu(II) complexes (Salen-tBu-Cu(II) and Salen-H_2-Cu(II)) were encapsulated inside the pores of MIL-101 using a "ship in a bottle" approach
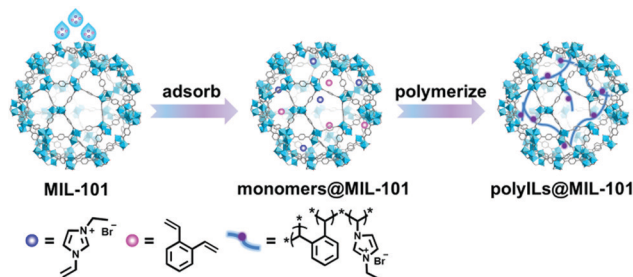

Fig. 15 Preparation of polyILs@MIL-101 involving the adsorption of monomers (3-ethyl-1-vinyl-1H-imidazol-3-ium bromide [blue balls] and 1,2-divinylbenzene [pink balls]) within the cavity of MIL-101 (middle) followed by the in situ polymerization of imidazolium-based poly(ionic liquid)s (dark blue lines with purple balls). Color code: C, gray; O, red; and Cr, cyan. H atoms are omitted for clarity. Adapted from ref. 313 with permission from the American Chemical Society, copyright 2018.

to obtain bifunctional catalysts for CO_2 epoxide cycloaddition.[312] Salen-tBu-Cu(II)@MIL-101 with 0.3 g g^{-1} Salen-tBu-Cu(II) loading gave the highest catalytic conversion (87.8%) of PO in the presence of TBAB under extremely mild conditions (25 °C, 1 atm CO_2 pressure).

As with MOFs, a goal of heterogeneous catalysis in MOF composites is to avoid the use of a co-catalyst. Toward this end, imidazolium-based poly(ionic liquid)s (polyILs) were confined in the cavities of MIL-101 using an in situ polymerization strategy (Fig. 15).[313] In the absence of co-catalyst, 94% of ECH was converted into the targeted product with high selectivity (>99%) in polyILs@MIL-101 at 70 °C and 1 bar of CO_2 after 24 h, with no significant decrease in catalytic performance after ten reactions. Similarly, a linear ionic polymer was inserted into the pores of MIL-101 to give a composite (MIL-101-IP).[314] With respect to CO_2–ECH cycloaddition, the authors found that MIL-101-IP (99% yield) outperformed the ionic polymer (3% yield), MIL-101 (32% yield), and the physical mixture of the two individual components (80% yield) under the same conditions. Kinetic studies indicated that the reaction's rate constant doubled in MIL-101-IP compared to that of the physical mixture at room temperature. Such work demonstrates a depleted energy requirement to obtain the similar conversion results in MIL-101-IP.

New components can also endow the corresponding composites with emergent functions/properties.[315] For example, templated growth and anchoring of ZIF-8 crystals on carbon nitrides (CNs), which possess micrometer-sized pores and high nitrogen contents, gave ZIF-8/CN foams with hierarchical porosities.[315] The composites were highly hydrophobic as evidenced by their water contact angles in excess of 135°. The 24 h conversion of ECH under 1 MPa of CO_2 and 80 °C was greatly improved in the ZIF-8/CN foam (100% with 100% selectivity to chloropropene carbonate) compared to that of the pristine ZIF-8 (conversion: 84.1%; selectivity: 52%). The significantly increased catalytic performance was mainly ascribed to the hydrophobicity and hierarchical porosity of the ZIF-8/CN foam which effectively improved the transport of reactants to the catalytically active sites.

3.1.3. Conversion of CO_2 into organic products using MOF derivatives. Pyrolysis of MOFs containing transition metals and

organic linkers especially those with O, N, and S produces a class of very interesting materials known as MOF derivatives. In such derivatives, a diverse array of active sites can be observed that are not typically found in MOFs.[88]

As an example of the use of MOF derivatives for these reactions, several zeolitic imidazolate frameworks (ZIFs; ZIF-7, -8, -9, and -67) were used as precursors to develop a series of N-doped, metal-containing nanoporous carbons, which were applied as catalysts for cyclic carbonate synthesis from epoxides and CO_2.[317] Among the obtained carbons, a bifunctional acid–base porous carbon synthesized by pyrolysis of ZIF-9 at 600 °C under an Ar stream exhibited the best catalytic activity (90% yield) under 0.6 MPa of CO_2 and 80 °C. The authors attributed the high activity to uniformly distributed, partly oxidized cobalt NPs and nitrogenous species, which acted as acidic and basic sites, respectively. Recently, employing ZIF-8 as a template and sodium hypochlorite (NaClO) as an oxidant, an oxidized porous carbon was synthesized.[318] Upon moderate oxidation, several oxygen-containing functional groups, including carboxyl, lactone and alkoxy, were introduced onto the surface of the N-doped porous carbon without any loss of the original active sites including ZnO and pyridinic nitrogen atoms. On the basis of the porosity inherited from ZIF-8, the synergistic effects between the multiple catalytic sites and the aid of TBAB, the optimized catalyst, ZnO@NPC-Ox-700 (NPC: N-doped porous carbon), exhibited high catalytic conversion, selectivity and recyclability for CO_2 cycloaddition with diverse epoxides under mild conditions (25–60 °C, 1 atm of CO_2).

These two reports demonstrate the potential for high activity and stability in MOF derivative-catalyzed CO_2 conversion. It is likely that the approach can be extended to other MOFs, opening new avenues to catalysts with enhanced activities, stabilities, and selectivities for CO_2 organic transformation.

3.2. Heterogeneous hydrogenation of CO_2

CO_2 hydrogenation produces feedstock chemicals such as methane, methanol, alkyl formates and formic acid. Such reactions have been extensively studied in recent years.[324,325] Homogeneous catalysts frequently show satisfactory activity but need to be utilized under very high total pressures (20–200 bar)

and are difficult to separate from catalytic systems.[325] As an alternative, heterogeneous catalysts such as the industrially-applied ternary $Cu/ZnO/Al_2O_3$ are desirable in terms of catalyst separability, stability, and applicability. Unfortunately, reactions utilizing such systems always employ high temperatures (200–300 °C) and pressures (50–100 bar) as heterogeneous catalytic reactions have higher activation barriers than their homogeneous counterparts.[326] In contrast, regarding heterogeneous CO_2 hydrogenation, MOFs possess the following advantages: (1) structural designability; MOFs can incorporate highly reactive frustrated Lewis pairs (LASs and LBSs) in a single material.[327–329] (2) porosity and availability of organic coordinating groups; classical catalysts such as metals, metal oxides, metal complexes, and metal clusters can be confined and/or stabilized in MOFs, and can cooperate with MOFs to augment their respective strengths and offset their respective drawbacks.[330–340] (3) certain MOFs can be thermally decomposed; a thermally converted MOF yields metal/metal oxide nanoparticles in a porous carbon matrix with uniform dispersion of active sites and enhanced thermal and chemical stability, resulting in highly efficient conversion of CO_2 under a variety of reaction conditions.[341–348] As summarized in Table 3, some MOF-based materials have been reported to catalyze CO_2 hydrogenation reactions under various conditions.

As an example of heterogeneous CO_2 hydrogenation achieved by a MOF, DFT calculations were used to study the catalytic behavior of UiO-66 functionalized with frustrated Lewis pairs (FLPs).[327] The calculated reaction mechanism involved first heterolytic dissociation of H_2 by the FLPs, then, in the second step a hydride and a proton were added to CO_2 in a concerted fashion, producing formic acid (HCOOH).[327,328] Through the studies, it was determined that H_2 heterolysis was the critical step in the catalytic reaction. The drawback in such a mechanism, however, was that the MOF must preferentially bind H_2 over CO_2. To this end, the same researchers developed a new catalyst for CO_2 reduction based on the expanded, isoreticular framework, UiO-67.[329] In UiO-67, more FLPs could be introduced without being quenched by adjacent FLP moieties. Furthermore, in the material, $UiO-67(NBF_2)_4$, heterolytic dissociation of H_2 was found to be much easier than CO_2 chemisorption due to

Table 3 Summary of CO_2 hydrogenation reactions in MOF-based materials[a]

Catalyst	Product	Temp. (°C)	Pressure (bar)	TOF (h^{-1})	Ref.
mbpyOH-IrCl$_3$-UiO	HCOOH	85	1 ($H_2/CO_2 = 1$)	36 ± 2	330
mbpy-IrCl$_3$-UiO				1.5 ± 0.2	
mbpyOH-[Ir^{III}]-UiO				410 ± 3	
mbpy-[Ir^{III}]-UiO				28 ± 2	
Cu⊂UiO-66	CH$_3$OH	175	10 ($H_2/CO_2 = 3$)	13.3	331
20Ni@MIL-101(DSM)	CH$_4$	300	$H_2/CO_2 = 4$ (GHSV^b = 3000 h^{-1})	5.9	332
20Ni@MIL-101(IM)		320		5.1	
Ni@UiO-66	CH$_4$	320	10 ($H_2/CO_2 = 3$)	154.8	333
Au&Pt@ZIF	CH$_3$OH + HCOOH	150	32 ($H_2/CO_2 = 3$)	1522	335
(Pt$_2^0$)$_{0.5}$-(Pt^{II}Cl$_2$)@{Ca^{II}Cu$_6^{II}$[(S,S)-methox]$_3$(OH)$_2$(H$_2$O)}·15H$_2$O	CH$_4$	140	6 ($H_2/CO_2/N_2 = 4:1:1$)	1.1	339
PZ8-400	CH$_3$OH	270	45 ($H_2/CO_2 = 3$)	972	342

^{a} The reports in this table include TOF values in h^{-1} (some have been converted to these units from the originally reported units). ^{b} Gas hourly space velocity.

This journal is © The Royal Society of Chemistry 2019

Chem. Soc. Rev., 2019, 48, 2783–2828 | 2805

the stronger binding of H_2 over CO_2 with adsorption energies of -0.22 and -0.50 eV for CO_2 and H_2, respectively. This dramatically reduced each activation energy for carbon dioxide methanolization. These calculated results suggested that MOFs could be adept CO_2 hydrogenation catalysts. Recently, molecular iridium catalysts were incorporated into two UiO-type MOFs by anchoring Ir^{3+} to the N atoms of bpydc linkers.[330] The resultant catalysts were placed in the condensing chamber of a Soxhlet extractor for hydrogenation of CO_2 to formate. This special reaction device maximized contact between the two reaction gases (CO_2 and H_2) and solvent (H_2O), and neutralized the solution using sodium bicarbonate (Na_2HCO_3) efficiently shifting the reaction $H_2(g) + CO_2(g) \rightleftharpoons HCO_2H(aq)$ toward formic acid formation. Moreover, the ligand's hydroxyl group acted as an electron-donating group and a hydrogen-bonding site, further facilitating the conversion of CO_2, resulting in a high TOF of 410 ± 3 h^{-1} under 1 MPa H_2/CO_2 (H_2 : CO_2 = 1 : 1) and 85 °C.

Various metal catalysts can be combined with MOFs, yielding hybrid materials designed to catalyze CO_2 hydrogenation reactions. As an example of such material, Cu nanocrystals ($\sim$18 nm) were encapsulated within UiO-66 to yield a composite catalyst ($Cu \subset UiO$-66) for highly selective CO_2 hydrogenation to methanol (Fig. 16a).[331] The catalytic performance of $Cu \subset UiO$-66 was investigated under a 10 bar gas mixture (CO_2 : H_2 = 1 : 3) at 175 °C. The initial turnover frequency (TOF) of MeOH formation was 3.7×10^{-3} s^{-1}, more than 8 times greater than that of the conventional $Cu/ZnO/Al_2O_3$ catalyst. More importantly, no byproducts were detected at any reaction temperature in the range of 175–250 °C. X-ray photoelectron spectroscopy (XPS) suggested that the Zr(IV) atoms in UiO-66

Fig. 16 (a) CO_2 hydrogenation using $Cu \subset UiO$-66 to give CH_3OH. (b) Preparation of $Cu/ZnO_x@UiO$-bpy (Cu/ZnO_x nanoparticles are represented as green and yellow balls) by in situ reduction of post-synthetically metalated UiO-bpy (left) for selective MeOH synthesis as the product of catalytic CO_2 hydrogenation. All MOFs are composed by Zr SBUs (cyan balls or polyhedra) and BDC and bpydc linkers (gray lines). Color code: C, gray; O, red; Zr, cyan. H atoms are omitted for clarity.

were reduced upon coming into contact with the Cu nanocrystals. This indicated that the improved TOF and selectivity of $Cu \subset UiO$-66 over $Cu/ZnO/Al_2O_3$ were caused by the increased contact area between the SBUs and the Cu nanocrystals. Different sized Ni NPs incorporated in MOFs also resulted in varied catalysts for CO_2 hydrogenation to methane.[332–334]

Integrating MOFs with two or more metal components may lead to unexpected CO_2 hydrogenation catalytic activity.[335,336] In order to hydrogenate CO_2 to MeOH, both Pt nanocubes ($\sim$6 nm) and Au nanocages ($\sim$31 nm) were embedded within ZIF-8 to form a composite, Au&Pt@ZIF.[335] Under irradiation by a Xe lamp, the heat generated by the photothermal effects of Au nanocages was insulated by ZIF-8. This improved the catalytic activity of the Pt nanocubes. The resultant catalytic CO_2 hydrogenation reaction had a high TOF number of 1522 h^{-1}. In fact, even at 60 °C, the Au&Pt@ZIF CO_2 hydrogenation catalyst was still active.

Although the noble MNPs in the abovementioned materials exhibit desirable CO_2 hydrogenation catalytic efficiencies, non-noble metal oxide catalysts are more economical and thus may be a better option for such conversions. Toward this end, a series of α-Fe_2O_3/ZIF-8 catalysts were assembled in which $\sim$30 nm α-Fe_2O_3 NPs were dispersed on the ZIF-8 supports.[337] Under a 3 MPa (CO_2 : H_2 = 1 : 3) pressure at 573 K, α-Fe_2O_3/ZIF-8 supported on 150 nm ZIF-8 crystals displayed considerable CO_2 conversion and light olefin (C1–C4) selectivity. More recently, a novel composite catalyst, $Cu/ZnO_x@UiO$-bpy with <1 nm Cu/ZnO_x NPs, was made by two post-synthetic metalations of UiO-bpy with Cu^{2+} and Zn^{2+}, respectively, and subsequent in situ reduction at 250 °C using a binary H_2/CO_2 mixture (total pressure: 4 MPa; H_2 : CO_2 = 3 : 1) (Fig. 16b).[338] In comparison with the industrial ternary $Cu/ZnO/Al_2O_3$ catalyst, the strong metal–support interactions (SMSIs) and confinement effects from UiO-bpy effectively prevented Cu NP aggregation. The phase separation between Cu and ZnO_x preserved the number of active interfaces. At 250 °C and under a constant flow of H_2/CO_2 (3/1) at 4 MPa, $Cu/ZnO_x@MOF$ presented a high space-time yield of 2.59 g_{MeOH} kg_{Cu}^{-1} h^{-1} with 100% MeOH selectivity, as well as high stability over 100 h. However, for the $Cu/ZnO/Al_2O_3$ catalyst, only 0.83 g_{MeOH} kg_{Cu}^{-1} h^{-1} was obtained with low MeOH selectivity of 54.8% under the same conditions, possibly caused by competing catalytic reactions such as reverse water gas shift (RWGS).

In addition to metal/metal oxide NPs, other highly active metal species can also be incorporated within MOFs in order to hydrogenate CO_2. For example, dinuclear Pt_2^0 clusters were homogenously incorporated into a bimetallic MOF ($\{Ca^{II}Cu_6^{II}[(S,S)\text{-methox}]_3(OH)_2(H_2O)\} \cdot 16H_2O$).[339] Under a gas mixture (CO_2 : N_2 : H_2 = 1 : 1 : 4) at 4 bar and 140 °C, the composite had a CO_2 methanation TOF of 3.1×10^{-4} s^{-1}, outperforming several industrial catalysts such as Ru–Al_2O_3. Recently, a facile method to immobilize a homogenous CO_2 hydrogenation catalyst, ($^{tBu}PNP)Ru(CO)HCl$, in the pores of UiO-66 was developed.[340] The process was based on the relative size of the catalyst with respect to the MOF's pore metrics as the catalyst is larger than the pore apertures of UiO-66 but smaller than the pore size (Fig. 17).
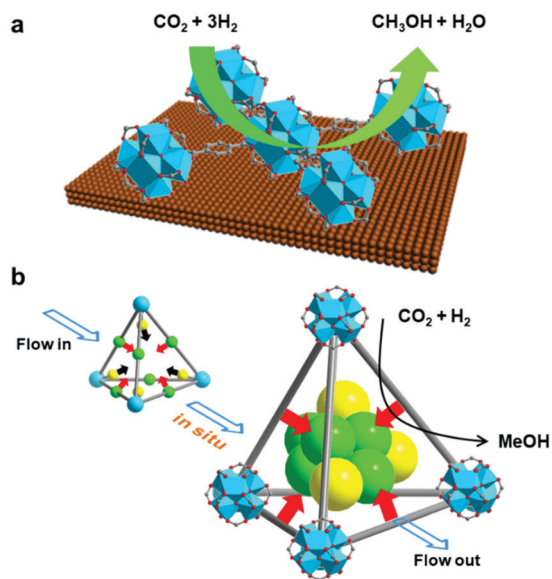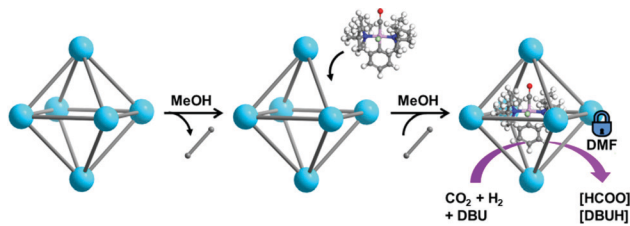
2806 | Chem. Soc. Rev., 2019, 48, 2783–2828

This journal is © The Royal Society of Chemistry 2019

Fig. 17 Encapsulation of the transition metal catalyst, (^{tBu}PNP)Ru(CO)HCl, in UiO-66 by terephthalate linker–SBU dissociation and catalyst incorporation in protic solvent (MeOH). This compound was applied to the hydrogenation of CO_2 to formate. UiO-66 is composed of Zr clusters (cyan balls) and BDC linkers (gray lines). Color code: C, gray; O, red; N, blue; Ru, pink; Cl, yellow-green; and H, white.

In the hybrid material, catalytic hydrogenation of CO_2 to formate was investigated in a DMF solution under 3 bar CO_2 and 12 bar H_2 at 300 K. The TON of the hybrid catalyst was comparable to that of the molecular catalyst and the catalytic activity was retained after 5 subsequent reactions. The authors attributed the prolonged activity of the catalyst to impediment of bimolecular catalyst deactivation as is common in heterogeneous catalysis.

Although many MOFs display excellent catalytic CO_2 hydrogenation performance, some are unstable at high temperature, preventing practical application. To remedy this drawback, MOF-derived materials were studied and applied.[341–348] A highly-active CO_2 methanation catalyst was generated by *in situ* pyrolysis of ruthenium (Ru)-impregnated UiO-66 during the catalytic methanation reaction.[341] The resultant catalysts were composed of a mixture of Ru^0 NPs (2–5 nm) supported by ZrO_2 NPs (10–20 nm) with two crystal forms (tetragonal and monoclinic). In the composites, the Ru^0 NPs served as active sites and the oxygen vacancies of the ZrO_2 NPs served as CO_2 adsorption sites. The composites with different Ru loadings (0.75–2 wt%) exhibited high CO_2 conversion efficiencies ($>90\%$) with exceptional methane selectivities (nearly 100%) at 350 °C and under a 5 bar gas mixture ($H_2:CO_2 = 4:1$). More importantly, the remarkable catalytic performance of 1Ru/UiO-66-derived catalyst (1 wt% of Ru loading) was maintained in excess of 160 h, demonstrating the catalyst's high stability.

It should be noted that reports of *in situ* catalyst preparation are very rare. Instead, most MOF-derived materials are formed by calcination at high temperatures, and only after this calcination can each catalyst's performance be evaluated.[342–346] For example, in a two-step process, presynthesized Pd@ZIF-8 was pyrolyzed in air and the products were then reduced by H_2 to afford a PdZn alloy catalyst supported on ZnO.[342] The catalyst was applied to CO_2 hydrogenation reactions targeting methanol as the product. After the two-step process, nearly 50% of the surface Pd atoms in the Pd NPs were substituted by Zn atoms, forming 3.7–5.8 nm PdZn alloy NPs. The highest methanol yield over the PdZn alloy catalysts was 0.65 g g_{cat}^{-1} h^{-1} at 270 °C and a total pressure of 4.5 MPa ($H_2:CO_2 = 3:1$). The excellent catalytic activity was attributed to the small size of the PdZn alloy NPs and abundant oxygen defects on the surface of the ZnO. Also, Cu/Zn nanoparticles in a carbon matrix can be prepared as exemplified by the calcination of Zn-doped HKUST-1 at 500 °C

under an argon atmosphere.[343] In this case, the metals did not sinter, nor did the bimetallic catalyst phase separate, leaving pyrolyzed 15–25 nm Cu/Zn NPs. The authors attributed this to protection of the metals by the carbon matrix. The Cu/Zn@C catalysts were subsequently applied to the RWGS reaction. A submillimeter-sized Cu/Zn@C sample exhibited the highest CO_2 conversion (5.0%) and CO selectivity (100%) at 500 °C and 1 bar ($H_2:CO_2 = 3:1$). Additionally, the catalyst remained active for over 20 hours. When using MIL-101(Fe) as both the template and self-sacrificing precursor, a core–shell Fe@C photocatalyst was formed by a two-step calcination approach. The material was then applied to solar-powered CO_2 conversion using H_2 (Fig. 18).[344] The pyrolysis process effectively prevented the generation of large Fe NPs at higher temperatures, resulting in the formation of ultrafine Fe NPs (~ 9.7 nm). Upon irradiation with UV-light, the Fe NP excitation was amplified by the plasmon–photon coupling effect on the surface of the Fe@C. This facilitated the formation of energetic hot electrons that activated CO_2. Accordingly, Fe@C produced 2196.17 μmol of CO after light irradiation for 2 h, outperforming both Fe/SiO$_2$ (1963.3 μmol) and Fe/CNT (1453.2 μmol) under the same reaction conditions. More importantly, the ultrathin carbon layers (1–3 layers) on the Fe NPs significantly facilitated the desorption of CO from the catalyst's surface of catalyst, leading to high CO selectivity ($>99.9\%$).

Though MOF-derived materials' sizes clearly play important roles in their catalytic activities, it was also determined that this activity could be regulated by tailoring a MOF's morphology.[345] By utilizing an ionic surfactant, cetyltrimethylammonium bromide (CTAB), the morphology of ZIF-67 crystals was transitioned from cubic to rhombic dodecahedron while the particle size increased from 150 nm to 1 μm. Upon pyrolysis in a N_2 atmosphere, Co-based porous carbon catalysts with Co NPs (7–20 nm in size)
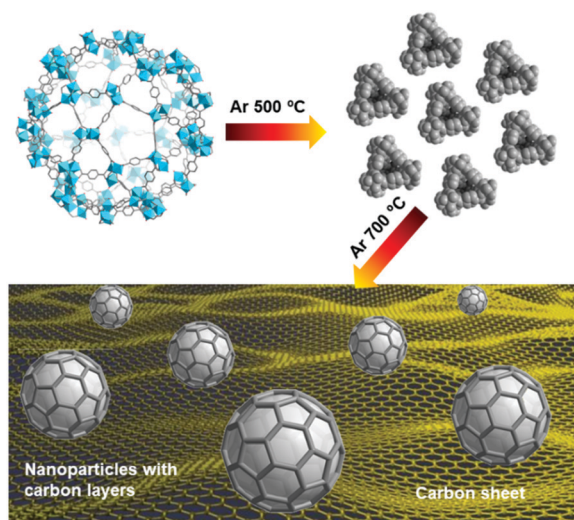

Fig. 18 The two-step preparation of core–shell Fe@C hybrids (bottom) from MIL-101(Fe) (upper left) with intermediate formation of Fe$_3$C and Fe$_3$O$_4$ (upper right) at 500 °C in Ar gas, and subsequent conversion to the final nanoparticles. Color code: C, gray; O, red; and Fe, cyan. H atoms are omitted for clarity.

were obtained while the original morphology of the MOF was preserved. Additionally, these Co NPs were well separated by the graphite-like carbon of the resultant catalyst, which effectively prevented metal sintering. When 0.01 wt% of CTAB was added, the resultant Co-based porous carbon catalyst exhibited a high BET surface area (346 $m^2 g^{-1}$), CO_2 adsorption capacity, CO_2 conversion efficiency (52.5%) and CH_4 selectivity (>99.2%) under 3 MPa of gas (H_2:CO_2 = 4:1) at 270 °C. Additionally, the catalytic performance of MOF derivatives for the hydrogenation of CO_2 can be promoted by loading a MOF (Basolite F300) with metals (0.75 wt%) using a well-established catalyst preparation method, namely incipient wetness impregnation.[346] Specifically, upon potassium loading, the catalyst exhibited improved olefin selectivity with C_2–C_4 olefin space time yields of 33.6 mmol g_{cat}^{-1} h^{-1}, on account of the increased CO_2 and CO affinity, while decreasing H_2 uptake and the balance between different active phases in the resultant K-doped catalysts.

As an alternative strategy, MOF derivatives for catalytic CO_2 conversion can be synthesized without thermal treatment.

Recently, a water-soaking process created a ZIF-67-derived (ZIF-67 is unstable in water) nanoreactor taking advantage of the phase transitions of ZIF-67@Pt@mSiO$_2$ (mSiO$_2$ = mesoporous silica) nanocubes.[347] During this phase transition, ZIF-67 acted as both a morphological template and a sacrificial cobalt source to react with the silicic acid from SiO_2 hydrolysis, yielding a

cobalt silicate. The CO_2 methanation was catalyzed by the final catalyst, Pt@CSN (cobalt silicate nanocubes). The two-step reaction mechanism involves (i) CO intermediate formation as the result of RWGS reaction on Pt sites, and (ii) CO methanation over Co sites. The shell structure of the Pt@CSN nanoreactor not only immobilized the Pt NPs but also offered additional diffusion pathways for reaction gasses and intermediates, prolonging their retention times and eventually boosting the CO_2 conversion and the selectivity toward CH_4 (41.8 and 94%, respectively at 30 bar [CO_2:H_2:N_2 = 6:18:1] and 320 °C).

3.3. Photocatalytic CO_2 reduction

One envisions a carbon-neutral energy cycle where any produced CO_2 can be converted to useful fuels and/or commodity chemicals with minimal energy input. To accomplish this, the importance of the application of solar energy to CO_2 conversion is paramount. Although semiconductor materials represent the state-of-the-art with respect to photocatalysis, they are plagued by rapid hole–electron recombination and poor CO_2 adsorption capacity, restricting their photocatalytic CO_2 reduction efficiencies. On the other hand, MOF-based materials have been identified as a new class of CO_2 reduction photocatalysts.[45,63,86,90] Their CO_2 capture performances are summarized in Table 1. The photocatalytic performances for CO_2 reduction in MOF-based materials are summarized in Table 4.

Table 4 Summary of photocatalytic CO_2 reduction reactions in a selection of MOF-based materials[a]

Catalyst	Electron donor	Light irradiation	Product	Photocatalytic efficiency (μmol g^{-1} h^{-1})	Ref.
(Y[Ir(ppy)$_2$(dcbpy)]$_2$[OH])	TEOA	Visible-light	$HCOO^-$	158.3	349
ZrPP-1-Co	TEOA	Visible-light	CO + CH_4	14.5	351
NH_2-MIL-125	TEOA	Visible-light	$HCOO^-$	16.3	352
PCN-222	TEOA	Visible-light	$HCOO^-$	60.0	353
Eu-Ru(phen)$_3$-MOF	TEOA	Visible-light	$HCOO^-$	94.0	354
NH_2-UiO-66	TEOA	Visible-light	$HCOO^-$	26.4	355
mixed NH_2-UiO-66				41.4	
MOF-253-Ru(CO)$_2$Cl$_2$	TEOA	Visible-light	CO + $HCOO^-$ + H_2	65.5	357
NH_2-MIL-101(Fe)	TEOA	Visible-light	$HCOO^-$	445.0	358
MIL-101(Fe)				147.5	
NH_2-MIL-53(Fe)				116.3	
MIL-53(Fe)				74.3	
NH_2-MIL-88(Fe)				75.0	
MIL-88(Fe)				22.5	
NNU-28	TEOA	Visible-light	$HCOO^-$	52.8	359
MOF-525-Co	TEOA	Visible-light	CO + CH_4	237.4	360
UiO-66-CrCAT	BNAH + TEOA	Visible-light	HCOOH	1724.3 ± 88	361
UiO-66-GaCAT				959.3 ± 84	
HKUST-1@TiO$_2$	—	UV	CH_4	2.6	376
UiO-66/CNNS	TEOA	Visible-light	CO	9.9	377
BIF-20@g-C_3N_4(20 wt%)	TEOA	Visible-light	CH_4 + CO	69.4	378
CdS/UiO-bpy/Co	TEOA	Visible-light	CO + H_2	276.0	379
CZS@UN20	—	Visible-light	CH_3OH	6.8	380
Au/NH_2-MIL-125(Ti)	TEOA	Visible-light	H_2 + $HCOO^-$	123.2	383
Pt/NH_2-MIL-125(Ti)				619.9	
ZIF0.03/T	—	UV-visible	CO + CH_4 + H_2	22.2	387
TiMOF-2	—	UV	CO + CH_4	0.71	388
Mg-MOF-74/TiO$_2$	—	365 nm UV	CO + CH_4 + O_2	12.7	390
TCNZ8	—	UV-visible	CH_3OH	0.75	394
Au@NENU-10	H_2O	Visible-light	CO + H_2 + CH_4	17.5	397
NH_2-rGO (5 wt%)/Al-PMOF	TEOA	Visible-light	$HCOO^-$	685.6	398
C-Cu$_{2-x}$S@g-C_3N_4-2	—	Visible-light	CO + H_2	90.75	403

[a] The reports in this table include photocatalytic efficiencies in μmol g^{-1} h^{-1} (some have been converted to these units from the originally reported units).

2808 | *Chem. Soc. Rev.*, 2019, **48**, 2783–2828

This journal is © The Royal Society of Chemistry 2019

3.3.1. MOFs for photocatalytic CO_2 reduction. The unique properties of MOFs position them as ideal platforms for the integration of photosensitizers, catalytic centers and CO_2 adsorption sites in a single material to target photocatalytic CO_2 reduction.[52,63,86,90]

As an example of photosensitizer and photocatalyst incorporation in a MOF, BPDC and $[Re^I(CO)_3(bpydc)Cl]$ were used as the organic linkers in the synthesis of a UiO-67 variant.[46] In the resultant framework, $[Re^I(CO)_3(bpydc)Cl]$ served as both the photoactive and catalytically active unit, leading to high catalytic activity. With TEA as a sacrificial reducing agent, the resulting mixed-linker UiO-67 exhibited a total CO-TON of 10.9 after a 20 h reaction, three times higher than that of the homogeneous $[Re^I(CO)_3(bpydc)Cl]$ catalyst. Such work demonstrates the utility of MOFs' porous natures. Photocatalysts do not have to be incorporated using a mixed-linker approach, however. In fact, $Ir(ppy)_2(Hdcbpy)$ was used as the organic linker to directly incorporate a photoactive catalyst into a MOF (Ir-CP) to achieve visible-light mediated CO_2 reduction.[349] The Ir-CP exhibited remarkable catalytic performance in the conversion of CO_2 to formate using triethanolamine (TEOA) as a sacrificial electron donating agent. Transition metal porphyrins can also be similarly useful in MOFs.[350,351] A metalloporphyrinic MOF (ZrPP-1-Co) was applied to CO_2-to-CO photoreduction.[351] The uniformly distributed porphyrinic Co^{2+} ions not only adsorbed CO_2, enhancing the MOF's uptake capacity (~ 4.0 mmol g^{-1} at 1 atm and 273 K), but also functioned as mediators, promoting electron transfer from linker-based benzene rings to the porphyrin cores to afford Co^0 in the presence of TEOA. The Co^0 species then activated and converted CO_2 to CO and hydrogenated CO to CH_4 with the aid of protonated TEOA.

The photocatalytic CO_2 reduction activities of MOFs can also be improved by combining photosensitizers and catalytically active sites within a single framework.[352–357] A titanium-based MOF, NH_2-MIL-125, was applied to CO_2 capture and subsequent photocatalytic reduction to formate under visible-light irradiation.[352] In this compound, the light was absorbed by the NH_2-BDC linkers, generating photoelectrons that were then transferred to the Ti centers in the SBUs by a ligand-to-metal charge transfer (LMCT) process. The metals then acted as active sites for CO_2 reduction and the Ti^{4+} ions were reduced to Ti^{3+} in the presence of TEOA. After 10 h, the material produced 8.14 mmol of $HCOO^-$ without significant degradation of the MOF's crystalline structure. Using a similar strategy, the photocatalytic activity of a porphyrin-based MOF (PCN-222), greatly extended the light harvesting capability of NH_2-MIL-125 such that it could absorb light from the entire visible spectrum (Fig. 19).[353] PCN-222 adsorbed CO_2 adeptly (2.6 mmol g^{-1} at 273 K and 1 atm) and electron–hole recombination in the material was dramatically suppressed as the photoelectrons were generated by electron transfer from the organic linkers to the Zr–oxo clusters. Such suppression of electron–hole recombination clearly demonstrates a potential advantage of MOF application to photocatalytic redox reactions. All of these advantages led to a considerable yield of formate (30 μmol in 10 h) as the product of photocatalytic CO_2 reduction.
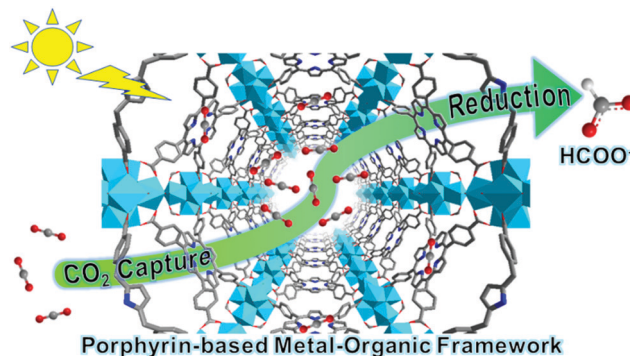

Fig. 19 Idealized scheme representing CO_2 capture and photocatalytic reduction to formate in PCN-222 which is composed of Zr_6 clusters and porphyrin linkers. Color code: C, gray; O, red; N, blue; H, white; and Zr, cyan. Adapted from ref. 353 with permission from the American Chemical Society, copyright 2015.

Time-resolved photoluminescence (PL) spectroscopy and ultrafast transient absorption spectroscopy confirmed that an extremely long-lived electron trap state existed in PCN-222. A photosensitizing MOF featuring dinuclear $Eu(III)_2$ clusters and $Ru(phen)_3$-derived organic linkers for visible-light-driven CO_2 reduction was also reported.[354] Calculations and characterization by ultrafast transient absorption, and EPR spectroscopy indicated that, upon visible light irradiation, the $Ru(phen)_3$ linkers were excited to triplet MLCT excited states, initiating electron injection into the Eu SBUs, which then became catalytically active. In this catalytic system, CO_2 was converted to formate with a fantastic rate of 321.9 μmol h^{-1} mmol MOF^{-1}, far exceeding many previous MOF catalysts under similar conditions.

In some cases, both the SBUs and organic linkers of MOFs can be simultaneously photoexcited, leading to dual photocatalytic excitation pathways in a single material.[358,359] This phenomenon was reported in some amine-functionalized MOFs including NH_2-MIL-101(Fe), NH_2-MIL-53(Fe), and NH_2-MIL-88B(Fe).[358] Upon exposure to visible light, the NH_2-BDC linkers were excited followed by electron transfer to the Fe–oxo clusters in a process analogous to the one detailed above. In addition, the Fe–oxo SBUs were directly excited, greatly enhancing the MOFs' photocatalytic activities (Fig. 20). Without amine functionalities, a zirconium-based MOF was synthesized using an anthracene-based organic linker.[359] The linker was an effective visible light harvester, transferring photogenerated electrons to the Zr–oxo SBU by LMCT. Meanwhile, photoinduced charges were generated on the linker by radical formation. The dual excitation routes simultaneously contributed to the photocatalytic CO_2 reduction activity, yielding formate and boosting the CO_2 conversion efficiency.

It should be noted that each photocatalytic MOF system detailed above was synthesized in a traditional, one-pot, solvothermal manner. As an alternative, post-synthetic modification (PSM) can expand the scope of available materials to achieve effective photocatalytic CO_2 reduction.[356,357,360–364] For instance, a metalloporphyrin zirconium-based MOF, MOF-525-Co, was

This journal is © The Royal Society of Chemistry 2019

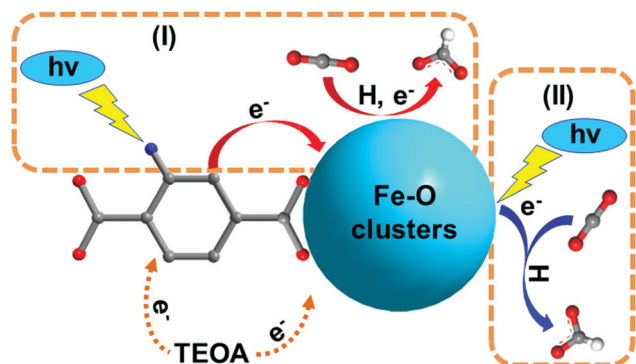Chem. Soc. Rev., 2019, **48**, 2783–2828 | **2809**

Fig. 20 Dual excitation pathways in a series of amine-functionalized Fe-based MOFs allowing for the conversion of CO_2 to formate. (I) The NH_2-BDC linkers were excited followed by electron transfer to the Fe–oxo clusters (turquoise polyhedra). (II) Direct excitation of Fe–oxo SBUs. Color code: C, gray; O, red; N, blue; Fe, cyan; and H, white.

Fig. 21 Preparation of Hf_{12}–Ru–M (M = Re or Mn) (upper right) *via* monocarboxylic acid exchange of Hf_{12}–Ru (upper left) and sunlight-driven CO_2 reduction using Hf_{12}–Ru–Re (bottom). Color code: C, gray; O, red; N, blue; Hf, cyan; Ru, pink; Re, orange; and Cl, green. H atoms are omitted for clarity.

synthesized by post-synthetic metalation of the porphyrin rings in MOF-525.[360] Upon irradiation with visible light, MOF-525-Co exhibited a drastically enhanced activity compared to that of pristine MOF-525. Photoluminescent (PL) quenching measurements of MOF-525-Co demonstrated that photogenerated excitons could directionally migrate from the organic porphyrin backbone to the core (*i.e.* the catalytic Co center). This extended the lifetime of the photoelectrons and allowed them to react with CO_2 in a reductive fashion. In another report, two Ru complexes, $Ru(CO)_2Cl_2$ and $Ru(bpy)_2Cl_2$, were tethered to the open N,N′-chelating sites in MOF-253.[357] In this case, $Ru(CO)_2Cl_2$ and $Ru(bpy)_2Cl_2$ served as the active site and photosensitizer, respectively and the total TON of the resultant catalyst was 55 after 8 h of visible light irradiation, about ten times higher than that of the homogenous $Ru(CO)_2Cl_2$ catalyst.

These strategies are clearly powerful, but they are marred by the fact that many organic linkers can not be easily functionalized using PSM. To address this, postsynthetic linker exchange was employed to synthesize a photoactive UiO-66 variant.[361] In the report, the BDC linkers of UiO-66 were exchanged with their catechol-functionalized counterparts (catbdc). The catechol groups were subsequently metalated with Cr^{3+} and Ga^{3+}, leading to the formation of metal-monocatecholato species within UiO-66. With the aid of 1-benzyl-1,4-dihydronicotinamide (BNAH) and TEOA, both functionalized UiO-66 frameworks displayed decent catalytic activity (6.14–11.22 TON after 13 h) for photocatalytic CO_2 reduction to formic acid. The Hf_{12} SBU surface of a two-dimensional MOF, Hf_{12}–Ru, with $M(bpy)(CO)_3X$ (M = Re and X = Cl or M = Mn and X = Br) was modified by carboxylate exchange to afford two photosensitizing metal–organic layers (MOLs, Hf_{12}–Ru–Re and Hf_{12}–Ru–Mn) for photocatalytic CO_2 reduction (Fig. 21).[362] The MOL combined $[Ru(bpy)_3]^{2+}$ photosensitizers and $M(bpy)(CO)_3X$ catalysts, in order to target synergistic effects between the two species. In particular, the proximity of the MOL skeleton to the capping molecules (1–2 nm) facilitated electron transfer from the reduced photosensitizer ($[Ru$-$(bpy)_3]^+$) to the catalytic centers ($M^I(bpy)(CO)_3X$ (M = Re, X = Cl or M = Mn, X = Br)), leading to high CO_2 reduction TONs of 3849 and 1347, respectively, after 12 h of visible light irradiation. Remarkably, when irradiated with natural sunlight, Hf_{12}–Ru–Re catalyzed CO_2 reduction with extraordinary efficiency, achieving a TON of 670 in 6 h. All of these catalytic performances were evaluated by several runs with low standard deviation, indicating the reliability of catalytic activities. In addition to the organic linkers, metal atoms in MOF SBUs can also be substituted. For example, a Ti-substituted NH_2-UiO-66(Zr/Ti) was synthesized and used as a visible-light-responsive photocatalyst for CO_2 reduction.[363] After metal substitution, the CO_2 uptake capacity and the photocatalytic formate yield were improved compared to NH_2-UiO-66. In contrast to the simple LMCT mechanism postulated to occur in NH_2-UiO-66, the authors speculated that the excited NH_2-BDC linkers of NH_2-UiO-66(Zr/Ti) would be inclined to transfer electrons to the Ti ions in the SBUs of $(Ti^{3+}/Zr^{4+})_6O_4(OH)_4$ and the reduced Ti^{3+} functioned as electron mediators donating electrons to Zr^4.
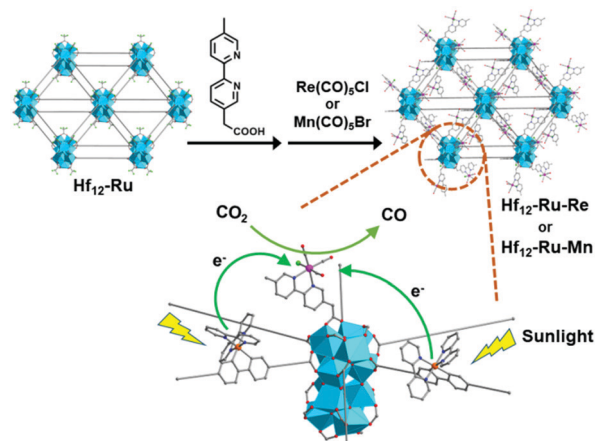
In addition, MOFs can behave solely as CO_2 photoreduction cocatalysts, achieving high photocatalytic activities in the resultant systems.[365–374] For instance, a visible-light-driven catalytic system employing ZIF-9, $[Ru(bpy)_3]Cl_2\cdot6H_2O$ and TEOA as cocatalyst, photosensitizer and electron donor, respectively, was applied to the photosplitting of CO_2.[365] Upon visible-light irradiation for 30 min, the catalyst produced 71.7 μmol of CO and H_2 based on the synergetic effects between cobalt and benzimidazolate moieties in ZIF-9. This activity surpassed those of many other MOFs such as Co-MOF-74 (23.8 μmol), Mn-MOF-74 (5.5 μmol), ZIF-8 (5.6 μmol) and NH_2-UiO-66 (4.3 μmol), indicating the unique ability of Co-ZIF-9 to photoreduce CO_2.

3.3.2. MOF composites for photocatalytic CO_2 reduction. Despite the fact that MOFs are appealing for photocatalysis, numerous MOFs have sufficiently large bandgaps such that they only absorb UV light and cannot be directly used for photocatalytic CO_2 reduction when irradiated with visible or longer-wavelength light. To address this challenge, metal

2810 | *Chem. Soc. Rev.*, 2019, 48, 2783–2828

This journal is © The Royal Society of Chemistry 2019

complexes such as $[Ru(bpy)_3]Cl_2 \cdot 6H_2O$ can be added to the catalytic systems to serve as photosensitizers.[365–374] Nevertheless, given the high cost and homogeneous nature of these noble metal complexes, a myriad of solid materials including inorganic semiconductors and metal NPs have been employed to replace them in conventional systems.[375–396] Inorganic semiconductor materials incorporated in MOFs act as photosensitizers and excite the frameworks upon exposure to light.[376–378,385–389] In turn, certain MOFs can effectively suppress the recombination of electron–hole pairs by transferring photoexcited electrons from the semiconductor materials to the MOFs and/or adsorbing the dissolved CO_2 in the reaction system, significantly improving the catalytic efficiencies of the given semiconductor.[375–378,385–398]

A semiconductor–MOF composite was designed for photocatalytic CO_2 reduction by growing ZIF-8 nanoparticles on Zn_2GeO_4 nanorods.[375] The photocatalytic activity of the resultant Zn_2GeO_4/ZIF-8 for CO_2 reduction was investigated in aqueous solution. Under light irradiation for 10 h, evolution of the product (MeOH) was enhanced by 62% in comparison to the pure Zn_2GeO_4. The authors speculated that this was caused by the increased CO_2 capture capacity and light response of the catalyst after the introduction of ZIF-8. By coating of TiO_2 onto the HKUST-1 microcrystals, a core–shell structured hybrid photocatalyst, HKUST-1@TiO_2, was made.[376] Given that TiO_2 is not able to harvest visible light HKUST-1@TiO_2 was illuminated with UV light and exhibited a catalytic efficiency over five times greater than that of TiO_2, with high CH_4 selectivity. Ultrafast spectroscopy demonstrated that the photogenerated electrons were transferred from the TiO_2 shell to the HKUST-1 core. This enhanced the charge-separation efficiency of the semiconductor and supplied adequate electrons to the adsorbed CO_2 molecules. All these factors facilitated highly selective conversion of CO_2 to CH_4 by an eight-electron process. Nanosheets were also incorporated with MOFs in an electrostatic self-assembly approach that integrated positively-charged UiO-66 crystals with negatively-charged nanosized carbon nitride nanosheets (CNNS).[377] The resultant material was a UiO-66/CNNS heterogeneous photocatalyst. The CO evolution rate afforded by UiO-66/CNNS was 9.9 μmol g_{CN}^{-1} h^{-1} under light irradiation for 6 h, over three times greater than that of CNNS (2.9 μmol g_{CN}^{-1} h^{-1}). The authors ascribed the improvement of photocatalytic performance to the electron transfer from the photoexcited CNNS to UiO-66 and effective inhibition of the electron–hole pair recombination in the CNNS, ultimately offering long-lived electrons for CO_2 reduction. More recently, this self-assembly method was applied to the combination of BIF-20 with graphitic carbon nitride (g-C_3N_4) to prepare a BIF-20@g-C_3N_4 nanosheet photocatalyst.[378] When the surface of BIF-20 was loaded with 20% g-C_3N_4, the resultant composite exhibited the highest catalytic performance (CH_4 evolution rate of 15.524 μmol g^{-1} h^{-1} and CO evolution rate of 53.869 μmol g^{-1} h^{-1}), outperforming the g-C_3N_4 nanosheet, bulk g-C_3N_4, and ZIF-8@g-C_3N_4 nanosheet. First-principles simulations indicated that the B–H bonds in BIF-20 functioned not only as electron capture centers to prevent the recombination of electron–hole pairs but also activated the adsorbed CO_2

molecules in BIF-20, greatly facilitating the photoreduction process. More recently, a ternary CdS/UiO-bpy/Co composite was synthesized by combining inorganic semiconductors (CdS) and molecular redox catalysts (Co complex) in a MOF.[379] Under visible light irradiation, the Co complex accepted electrons from the CdS photosensitizer and subsequently photochemically reduced CO_2 to CO. Additionally, in the composites, CdS NPs (∼10 nm) were obtained due to the coordination of bpydc with Cd^{2+}, eventually affording an high CO evolution rate of 235 mmol g^{-1} h^{-1} with a desirable selectivity (>85%). The authors attributed the high catalytic performance to the promoted separation and migration of photo-induced charge carriers, enhanced CO_2 uptake capacity (compared with pure CdS) as well as the abundant active sites for CO_2 reduction.

As a matter of fact, MOFs can also serve as photosensitizers in some semiconductor–MOF composites.[380–382] A prime example is found in a series of $Cd_{0.2}Zn_{0.8}S$@NH_2-UiO-66 composites.[380] Under visible-light irradiation, both $Cd_{0.2}Zn_{0.8}S$ and NH_2-UiO-66 were excited, generating electron–hole pairs. Since the LUMO potential of NH_2-UiO-66 (−0.60 eV vs. NHE) is more negative than the conduction band (CB) potential of $Cd_{0.2}Zn_{0.8}S$ (−0.56 eV vs. NHE), the photogenerated electrons can transfer from the LUMO of NH_2-UiO-66 to the CB of $Cd_{0.2}Zn_{0.8}S$, suppressing the recombination of electron–hole pairs and prolonging the lifetime of photoinduced charge carriers. This ultimately accelerated the photocatalytic conversion of CO_2 up to 6.8 mol h^{-1} g^{-1} under visible-light irradiation, over 3 times higher than that of pure $Cd_{0.2}Zn_{0.8}S$. Since the LUMO potential of NH_2-UiO-66 is more negative than the CB potential of anatase TiO_2 (−0.28 eV vs. NHE), a Type II heterojunction was formed in a TiO_2/NH_2-UiO-66 composite.[381] By transferring photogenerated electrons from NH_2-UiO-66 to TiO_2, the electron–hole separation in NH_2-UiO-66 was promoted and CO_2 was reduced to CO by TiO_2, with a superior CO evolution rate as compared to the pure TiO_2.

Enhanced photocatalytic performance can be realized in MNP–MOF composites along two pathways: visible-light harvesting and electron transfer.[383,384] As an example, Pt nanoparticles were encapsulated in NH_2-MIL-125 using the wetness impregnation method.[383] Although the absorption spectrum of the resultant composite (Pt/NH_2-MIL-125) was not affected by the incorporation of Pt NPs, a 21% increase in the photocatalytic activity (CO_2 to formate) was observed. Electron spin resonance (ESR) studies and DFT calculations demonstrated that the hydrogen spilled over from the doped Pt to Ti–O oxoclusters, generating the active sites (Ti^{3+}) in the material. Recently, Re_3-MOF layers were coated onto pre-synthesized Ag nanocubes (98 nm), resulting in a core–shell photocatalyst (Ag⊂Re_3-MOF) for CO_2-to-CO conversion (Fig. 22).[384] In this system, the strong Ag localized surface plasmon resonance (LSPR) (λ_{max} = 480 nm) overlapped with the absorption range of the Re_3-MOF (400 nm < λ < 550 nm). Therefore, the Ag⊂Re_3-MOF composite inherited the characteristic LSPR properties of the Ag nanocubes and the photoactive Re centers of Re_3-MOF were spatially confined to the intensified near-surface electric fields created at the surface of the Ag core. All of these effects lead to a 7-fold increase in the (visible light)
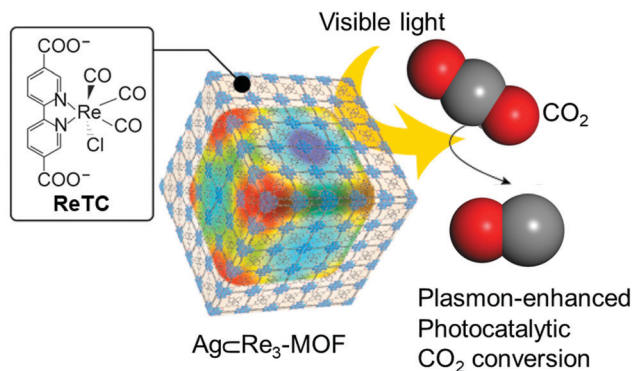
This journal is © The Royal Society of Chemistry 2019

Chem. Soc. Rev., 2019, 48, 2783–2828 | 2811

Fig. 22 Plasmon-enhanced photocatalytic CO_2 reduction to CO using Ag⊂Re$_3$-MOF under visible light irradiation. Adapted from ref. 384 with permission from the American Chemical Society, copyright 2017.

Fig. 23 (left) Sandwich-like ZnIn$_2$S$_4$–In$_2$O$_3$ hierarchical tubular heterostructures and (right) Catalytic CO_2 photoreduction using the ZnIn$_2$S$_4$–In$_2$O$_3$ with double-heterojunction shells under visible light irradiation. Adapted from ref. 401 with permission from the American Chemical Society, copyright 2018.

photocatalytic conversion of CO_2 to CO compared to pristine Re$_3$-MOF, with long-term catalytic stability maintained up to 48 h.

To summarize, conventional strategies applied to make MOF composite photocatalysts include: (1) combination of MOFs with semiconductors such as g-C$_3$N$_4$ or TiO$_2$. The intimate interfacial contact between semiconductors and MOFs results in the formation of heterojunctions, while the MOFs act as cocatalysts. This synergy induces efficient, persistent electron–hole separation and thus improves photocatalytic efficiency. (2) Stabilization of cocatalysts such as Cd$_{0.2}$Zn$_{0.8}$S by MOFs. The conjugated organic linkers in MOFs can behave as molecular antennae to be photoexcited. The photoelectrons then transfer to the cocatalyst for CO_2 reduction. (3) Immobilization of photoactive metal nanoparticles into MOFs. Such components harvest solar energy, exciting and then transferring electrons to active sites in the MOF(s) for subsequent CO_2 reduction.

3.3.3. MOF derivatives for photocatalytic CO_2 reduction. In an analogous fashion to CO_2 capture, MOF pyrolysis can be applied to the synthesis of materials for photocatalytic CO_2 reduction.[399–403] To various extents, these catalysts inherit the pore characteristics of their MOF templates. This not only benefits the adsorption and subsequent concentration of CO_2, but can also create new catalytically active sites.

A MOF-derived TiO$_2$ material was made by directly pyrolyzing NH$_2$-MIL-125 in an oxygen atmosphere and applied to CO_2 photoreduction.[399] When the precursor (NH$_2$-MIL-125) was replaced by NH$_2$-MIL-125 doped with gold NPs (GNPs), a dramatic increase in CH$_4$ yield was observed due to the visible light absorption of gold surface plasmon and/or the electron storage capacities of GNPs, and the minimal GNP/TiO$_2$ lattice defects, which effectively inhibited electron–hole recombination. Additionally, core–shell ZIF-8@ZIF-67 crystals were employed as precursors for the synthesis of a porous ZnO@Co$_3$O$_4$ composite.[400] Interestingly, unlike the unstable CH$_4$ evolution observed in ZIF-8-derived ZnO, the CH$_4$ evolution increased steadily during the entire reaction involving ZnO@ Co$_3$O$_4$. This was attributed to suppressed ZnO photocorrosion after embedding the Co$_3$O$_4$ co-catalyst on the surface.

Some structural features of MOF-derived materials (e.g. hollowness) can reduce bulk-to-surface diffusion length (accelerating
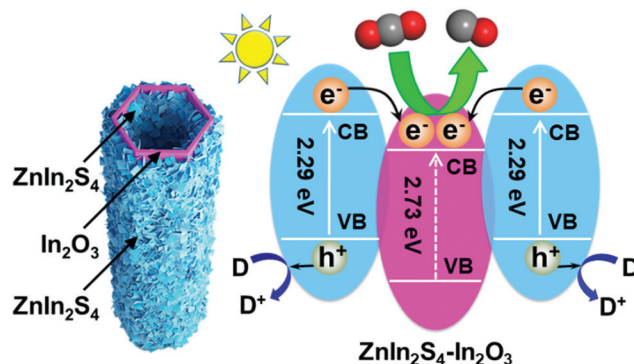
electron–hole separation) and provide high surface area in order to boost CO_2 adsorption and substrate/product transfer.[401–404] These features play significant roles in enhancing a given MOF derivative's photocatalytic CO_2 reduction activity. Using MIL-68(In) as precursor, a series of sandwich-like ZnIn$_2$S$_4$–In$_2$O$_3$ photocatalysts with hierarchical tubular heterostructures were generated by growing ZnIn$_2$S$_4$ on both surfaces of the In$_2$O$_3$ microtubes (Fig. 23).[401] The highest CO evolution rate of ZnIn$_2$S$_4$–In$_2$O$_3$ was 3075 μmol h^{-1} g^{-1}, which was further confirmed by repeated experiments. The authors attributed this to the promoted transport of photoinduced charges and accelerated electron–hole separation from the double-heterojunction formed by the sandwich-like structure.

Again, MOF derivatives do not have to be synthesized by high-temperature pyrolysis. Indeed, the same team demonstrated the construction of hierarchical In$_2$S$_3$-CdIn$_2$S$_4$ nanotubes by converting MIL-68(In) to hierarchical In$_2$S$_3$ nanotubes through a liquid phase sulfidation process with subsequent cation exchange.[404] The hierarchical heterostructured tubes were capable of separating and migrating photoinduced charge carriers, improving the material's CO_2 adsorption capacity, and providing abundant catalytically active sites. The resultant material exhibited a decent CO production rate (825 μmol h^{-1} g^{-1}) in the presence of Co(bpy)$_3^{2+}$ and TEOA, approximately 12 times higher than that of pure In$_2$S$_3$.

3.4. Electrocatalytic CO_2 reduction

Electrochemical carbon dioxide reduction reactions (CO$_2$RR) can be accomplished under mild conditions, putting them in stark contrast with many other transformations. Furthermore, the energy utilized to carry out these reactions can be obtained from renewable energy sources. Generally, electrochemical CO_2 reduction occurs by proton abstraction from solvent molecule(s), yielding various fuels and value-added chemicals.

3.4.1. MOFs for electrocatalytic CO_2 reduction. Extensive efforts have been devoted to the development of homogeneous and heterogeneous catalysts for CO$_2$RR. Outstanding challenges remain, such as low catalytic efficiency, undesirable selectivity,

and poor long-term stability. Fortunately, MOFs can incorporate redox-active sites, concentrate CO_2, and even facilitate uniform proton transport to catalytic sites. In this section we give examples of how these properties allow MOFs to improve upon previous attempts to affect CO_2RR reactions.

Inspired by the unique catalytic properties of metallic Cu for electrochemical CO_2 reduction, select proton-conductive, Cu-based, MOFs have been applied as electrochemical CO_2RR catalysts.[405–410] As an example, a copper rubeanate MOF was used for highly selective conversion of CO_2 to HCOOH.[405] Since HCOOH is easily produced at relatively weak CO_2 adsorption, the final selectivity of HCOOH using this MOF was 98%, significantly greater than that of metallic Cu ($\sim$38%), with a current efficiency of 30% from -1.6 to -1.2 V *vs.* SHE, due to its weak CO_2 adsorption behavior. Current efficiency (also called faradaic efficiency) which refers to the percentage of charge from an electrochemical process that is used to generate a specific product is a critical parameter used to evaluate the applicability of a given electrode. As a typical copper-based MOF, HKUST-1 has been deposited on different electrodes to serve as an electrocatalyst.[406–409] In these reports, oxalic acid, alcohols, and hydrocarbons have been produced. More recently, the paddle-wheel Cu dimer SBUs of HKUST-1 were desymmetrized to target multiple-carbon product generation (Fig. 24).[409] By simply heating the material to 250 °C, adjacent benzene-1,3,5-tricarboxylate (BTC) moieties were separated from the Cu dimer, decreasing the Cu–Cu coordination number (CN) in HKUST-1 as confirmed by extended X-ray absorption fine structure (EXAFS) spectroscopy. When the calcination time was increased to 3 h, the Cu–Cu CN reduced to 9.5 ± 0.9 while the framework maintained its structural integrity and crystallinity. The C_2H_4 faradaic efficiency (FE) in this distorted HKUST-1 variant was 45% with a current density of 262 mA cm^{-2} at -1.07 V *vs.* RHE, whereas the best C_2H_4 FE was only $\sim$10% in pristine HKUST-1, yielding a range of products. The experiment were reproducible with small data deviation, indicating the reliability.

To produce another MOF-based electrocatalyst, Zn-MOFs were deposited on carbon paper (CP), yielding Zn-MOF/CP electrodes by an electrophoretic deposition (EPD) method.
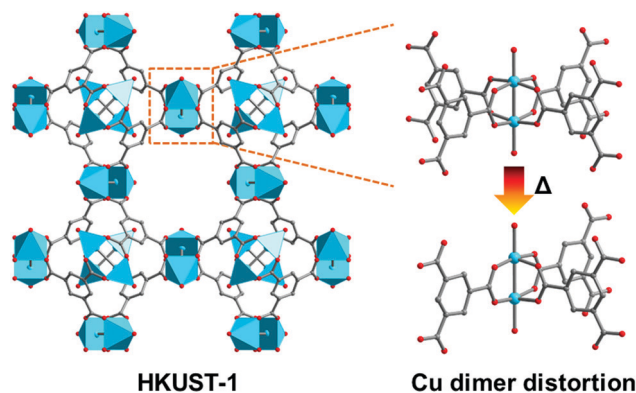
These electrodes were used to convert CO_2 to CH_4 using ionic liquid (IL) electrolytes.[411] Fluorine-containing, imidazolium-based ILs can not only absorb and activate CO_2 molecules but also promote the transformation of CO_2 to a $CO_2^{\bullet-}$ intermediate. The highest electrochemical activity ($80.1 \pm 6.6\%$ of CH_4 FE) was obtained with a current density of 3.1 ± 0.5 mA cm^{-2} at an applied potential of -2.2 V *vs.* Ag/Ag^+ over 2 h based on the combination of Zn-MOF/CP cathode and the IL ($BmimBF_4$). Four zinc-based ZIFs, including ZIF-7, ZIF-8, ZIF-108, and SIM-1 were studied for CO_2RR activity in an aqueous electrolyte.[412] In a CO_2-saturated 0.25 M K_2SO_4 solution (pH = 4.2), the best CO faradaic efficiency was 81.0% at -1.1 V *vs.* RHE over ZIF-8, and ZIF-108 manifested the highest CO current density (12.8 mA cm^{-2} at -1.3 V *vs.* RHE). Imidazolate ligands coordinated with the Zn(II) center was proved to be the active sites in ZIFs for CO_2RR by *in situ* X-ray absorption near edge structure (XANES) spectra and DFT calculations.

Incorporating redox-active organic linkers into MOFs can also yield materials with enhanced catalytic CO_2RR performance.[413–416] A thin film MOF electrode was made by depositing alumina (5 nm thickness) onto conductive carbon disk electrodes using atomic-layer deposition (ALD) and subsequently converting the alumina films to Al-TCPP-Co (Fig. 25a).[413] A CO selectivity over 76% was achieved by the resultant electrode with a per-site TON of 1400 and extremely small deviations were found upon repetitions of the experiment. The catalyst remained stable for up to 7 h. *In situ* spectroelectrochemical measurements demonstrated that the porphyrinic Co(II) were reduced to Co(I) during electrocatalysis. Liquid-phase epitaxy has also been demonstrated
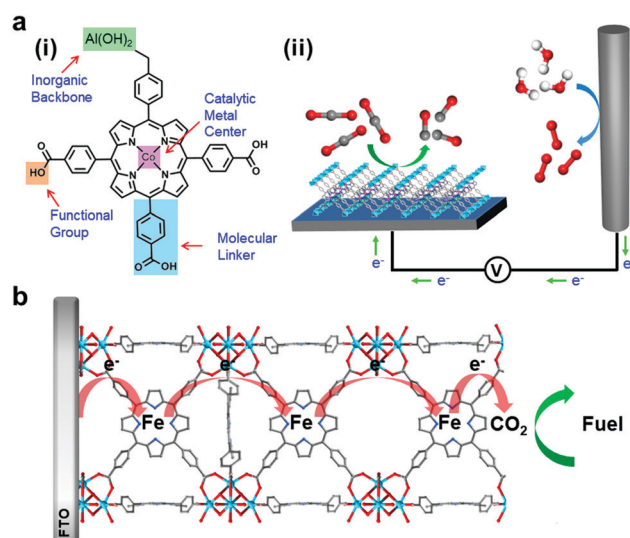

Fig. 24 Desymmetrization of the Cu dimers in HKUST-1 during calcination at 250 °C. Color code: C, gray; O, red; and Cu, cyan. H atoms are omitted for clarity.

Fig. 25 (a) $Al_2(OH)_2TCPP$-Co serves as an electrocatalytic CO_2 reduction catalyst (i) molecular-level view of $Al_2(OH)_2TCPP$-Co catalyst highlighting the modular nature of the metal centers, organic linkers, and additional functional groups; (ii) the MOF is integrated with a conductive substrate yielding the functional CO_2 electrochemical reduction system. (b) CO_2 photoreduction in Fe-porphyrin-based MOF-525/FTO thin films. In the system, the functionalized Fe-porphyrins act as catalytically competent, redox-conductive linkers. Color code: C, gray; O, red; N, blue; and Al/Zr, cyan. H atoms are omitted for clarity.

to be a valid approach for fabricating homogeneous and highly oriented MOF thin films of controllable thicknesses. For example, highly oriented surface grafted MOF (SURMOF) thin films were grown on fluorine doped tin oxide (FTO) glass electrodes using a liquid-phase epitaxy process.[414] The Re(CO)$_3$(bpydc)Cl linkers in the SURMOF electrocatalytically reduced CO_2 to CO with a FE up to $93 \pm 5\%$ at a -1.6 V vs. NHE potential, far exceeding that of the homogeneous Re(CO)$_3$(bpydc)Cl catalyst. Using a post-synthetically metalated Fe-porphyrin-based MOF-525 thin film electrode on FTO glass, CO_2 was reduced to CO (Fig. 25b).[415] Controlled potential electrolysis (CPE) experiments (at -1.3 V vs. NHE) showed that the current density increased to 5.9 mA cm^{-2} and the FEs of CO and H$_2$ were 41 ± 8 and $60 \pm 4\%$, respectively, after $\sim$4 h of electrolysis, which implied that the total faradaic efficiency (CO + H$_2$) of this catalytic system was $\sim$100%.

All of the abovementioned cases demonstrate that MOFs are a superb platform to immobilize redox-active moieties, yielding heterogeneous catalysts for effective and selective CO_2RR. However, due to the poor electrical conductivities of most MOFs, at this stage, working electrodes for CO_2RR must be fabricated by the deposition of MOF nanocrystals on various conductive substrates such as CP, FTO glass, gas diffusion electrodes, etc.[405–419]

3.4.2. Carbon materials derived from MOFs for electrocatalytic CO_2 reduction. MOFs can also be used to form carbon-based MOF derivatives for CO_2RR. These compounds usually possess excellent stabilities and high electrical conductivities, making them powerful electrocatalysts. Moreover, the well-dispersed active sites are confined in the resultant carbon matrix. This can dramatically improve the catalytic activities and selectivities of the associated reactions. Additionally, the resultant porous structures provide a means of CO_2 enrichment, greatly affecting CO_2 chemical transformations by increasing local concentrations.

As an example, the CO_2 electrochemical conversion capabilities of oxide-derived Cu/carbons (OD Cu/C) fabricated by carbonization of HKUST-1 were evaluated.[420] The highest methanol yield was obtained using the catalyst OD Cu/C-1000, which produced 12.4 mg L^{-1} h^{-1} at -0.3 V vs. RHE. Additionally, and the maximum ethanol production rate (13.4 mg L^{-1} h^{-1}) was observed at -0.7 V vs. RHE. This was attributed to synergistic effects between the highly dispersed Cu and porous carbon matrix. Recently, ZIF-8 was also utilized as a precursor in the preparation of nitrogen-doped porous carbons.[421] The resultant materials exhibited excellent electrocatalytic CO_2 to CO reduction with a CO FE of $\sim$78% at -0.93 V vs. RHE on account of the presence of abundant pyridinic-N and quaternary-N species. Both the pyridinic-N and quaternary-N species in the carbon matrix can promote the transfer of proton–electron pairs to CO_2, lowering the energy barrier for the production of the intermediate (COOH*) for CO formation. A series of nitrogen-doped carbons containing atomically dispersed Co sites was synthesized by annealing bimetallic Co/Zn ZIFs at different temperatures (Fig. 26).[422] Interestingly, the N coordination number of Co sites could be controlled by varying the temperature at which the pyrolysis was performed. The catalyst containing Co–N$_2$ active sites was more capable of activating CO_2, leading to the
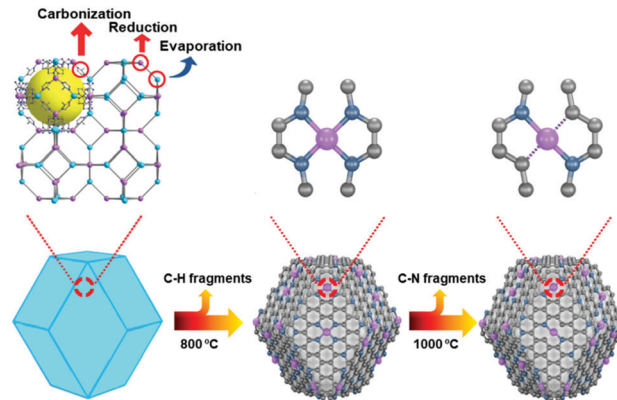

Fig. 26 The formation of Co–N$_4$ (upper middle) and Co–N$_2$ (upper right) via pyrolysis of bimetallic Co/Zn zeolitic imidazolate frameworks (upper left and bottom left) at 800 °C and 1000 °C, respectively. Color code: C, gray; N, gray-blue; Zn, cyan; and Co, purple. Adapted from ref. 422 with permission from Wiley-VCH, copyright 2018.

generation of the $CO_2^{\bullet-}$ intermediate. Therefore, this catalyst exhibited the highest electrocatalytic performance with a CO FE and current density of 94% and 18.1 mA cm^{-2}, respectively, at an overpotential of 520 mV, among the investigated samples. Notably, the CO TOF over this Co catalyst with the lowest N coordination number was up to 182 000 h^{-1}, outperforming most reported metal-based catalysts under comparable conditions. Two atomically dispersed Fe and Co catalysts (Fe–N–C and Co–N–C), were synthesized using bimetallic Fe/Zn and Co/Zn ZIFs, separately, as precursors.[423] In comparison to the optimized catalytic activity of Co–C–N (CO FE of 45% at an overpotential of 0.48 V), Fe–N–C displayed a higher CO FE of $>$93% with a current density of -2.8 mA cm^{-2} at a low overpotential of 0.47 V. The first principle calculations indicated that the edge-hosted M–N$_{2+2}$–C$_8$ moieties bridged by two adjacent armchair-like graphitic layers were more active than the bulk-hosted M–N$_4$–C$_{10}$ moieties embedded in the graphitic layers with respect to CO_2RR. Particularly, CO_2RR is more favorable than hydrogen evolution on the Fe–N$_{2+2}$–C$_8$ sites of the Fe–N–C catalyst, leading to the reported remarkable CO FE.

In contrast to the direct thermal decomposition of MOFs, a ZIF-assisted strategy was employed to synthesize Ni single atoms distributed in a nitrogen-doped porous carbon (Ni SAs/N–C) matrix. This was accomplished by exchanging ions between the Zn SBUs and the adsorbed Ni salts in the pores of ZIF-8.[424] Compared with Ni NPs and Ni foam, the obtained Ni SAs/N–C catalyst was able to selectively reduce CO_2 with an excellent current density and CO FE of 10.48 mA cm^{-2} and 71.9%, respectively, at an overpotential of 0.89 V, indicative of the superiority of single atom catalysts for CO_2RR. Furthermore, no obvious decline of CO FE and current density was observed during 60 h of CO_2 electroreduction at a potential of -1.0 V vs. RHE, demonstrating the high electrocatalytic stability of this single-atom catalyst. The surface of ZIF-8 was functionalized by taking advantage of the coordination interactions between Zn nodes and ammonium ferric citrate (AFC).[425] Upon pyrolysis, isolated iron–nitrogen (Fe–N) sites were formed on the surface

of the resulting carbon matrix. These highly exposed Fe–N sites endowed the resultant catalyst (C-AFC©ZIF-8) with an optimal faradaic efficiency for CO production of 93.0% at an overpotential of −0.43 V.

In order to further improve the electrocatalytic performance of carbon materials derived from MOFs for CO_2RR, a hybrid material, composed of ZIFs and multi-walled carbon nanotubes (MWCNTs) loaded with furfuryl alcohol (FA) was used as a precursor, to fabricate a pyrolyzed ZIFs supported on carbon nanotube networks.[426] The MWCNT support was capable of enhancing the CO_2 mass transport and electron transport in the resultant hybrid catalyst, resulting in a fantastic CO faradaic efficiency ($\sim$100%) and a high current density of 7.7 mA cm^{-2} at a low overpotential of 740 mV. When the hybrid catalyst was doped with Fe, the overpotential was as low as 440 mV with a desirable CO FE and current density of 97% and 2 mA cm^{-2}, respectively. Given the decent electrocatalytic activities of transition-metal phosphides, MoP NPs supported on In-doped porous carbon (In-PC) were made using MIL-68(In) as a carbon precursor.[427] The hybrid structure, strong interactions, and cooperative effects between the nano-MoP (4 nm) and In-PC support of the resultant catalyst (MoP@In-PC) ensured more active sites and space for efficient CO_2 adsorption and electrolyte diffusion to the electrode. Additionally, these features allowed for faster electron transfer to the adsorbed CO_2 to form $CO_2^{\bullet-}$ intermediates than in the bulk MoP. Accordingly, MoP@In-PC exhibited excellent catalytic performance for CO_2RR to formic acid with an outstanding faradaic efficiency and current density of 96.5% and 43.8 mA cm^{-2}, respectively, by choosing ionic liquid 1-butyl-3-methylimidazolium hexafluorophosphate as the electrolyte.

4. The relationship between CO_2 capture capacity of MOF-based materials and their catalytic performance for CO_2 conversion

After over two decades of investigation, MOFs that outperform other porous materials with respect to CO_2 adsorption capacity have been developed. Additionally, catalytic CO_2 conversion in MOF-based materials has also been well studied. In this context, an understanding of how the CO_2 capture capabilities of MOF-based materials affect their catalytic conversion efficiencies is paramount. Such an understanding will guide the development of efficient catalysts for CO_2 conversion.

The relationship between the CO_2 capacity of a given MOF-based material and its catalytic CO_2 conversion efficiency is clear. This relationship is governed by the following phenomena: (1) MOF-based materials can increase the local CO_2 concentration around materials' catalytically active sites by CO_2 adsorption. In this context, MOF pores serve as "microreactors", providing favorable environments for reactions between CO_2 and substrates. This has led to the observation of high reaction yields and selectivities in MOF-based materials; (2) some functional

groups in MOFs enhance their CO_2 uptake and activate CO_2 molecules and/or other reactants, further improving MOFs' catalytic efficiencies;[428] (3) the high CO_2 adsorption selectivities of MOF-based materials can guarantee high catalytic performance even in mixed-gas environments with low CO_2 concentrations.[109,286,313,367,369,374]

To demonstrate the culmination of these phenomena, we will present a couple of examples. One is found in a UiO-67–Ru^{II} composite (UiO-67/RuCO). This material was prepared by incorporating a photoactive Ru^{II}–CO complex ([Ru^{II}(bpy)(terpy)(CO)][PF$_6$)$_2$]) into UiO-67 using a facile PSE method (Fig. 27a).[369] Although the total TON produced by the homogeneous Ru^{II}–CO complex catalyst was slightly higher than that of the composite, the photocatalytic activity of the molecular catalyst was drastically reduced as the partial pressure of CO_2 decreased (Fig. 27b). This indicated that catalysis was heavily dependent on the concentration of CO_2 in the reaction mixture. In stark contrast, UiO-67/RuCO displayed almost the same catalytic performance even under a 5% CO_2 atmosphere. This surpassed both the homogeneous catalyst and a physical mixture of UiO-67 and the Ru^{II}–CO complex, and the results demonstrated that the UiO-67/RuCO composite could enrich gas mixtures containing CO_2 and take advantage of synergy between the adsorptive sites and the catalysts' active sites. Similarly, the catalytic performance of an IL-MOF composite (polyILs@MIL-101) for cycloaddition of CO_2 with ECH was maintained in a wide CO_2 pressure range from 0.5–1.5 bar, whereas the catalytic activity of the pure IL significantly declined once the CO_2 pressure was reduced to 0.5 bar.[313] More recently, three isostructural MOFs (MAF-X27-Cl, MAF-X27-OH
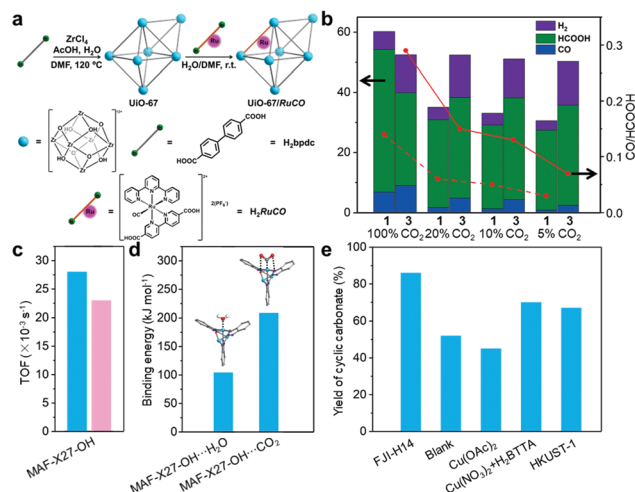

Fig. 27 (a) Synthesis of UiO-67 from ZrCl$_4$ and H$_2$bpdc, and UiO-67/RuCO by post-synthetic exchange of H$_2$RuCO with H$_2$bpdc. Both UiO-67 and UiO-67/RuCO are composed of Zr clusters (cyan balls) and organic linkers (gray and/or orange lines). (b) Photochemical reduction of CO_2 with Ru^{II}–CO complex and UiO-67/RuCO: left y-axis, catalytic activity (bar graph); right y-axis, product selectivity (line graph). (c) Comparison of the TOF values for the photocatalytic reduction of CO_2 to CO under 1.0 atm (blue) and 0.1 atm (pink); (d) comparison of the CO_2 and H$_2$O binding structures and energies of reduced MAF-X27-OH. Color code: C, gray; O, red; N, blue; Co, cyan; and H, white. (e) Catalytic conversion of CO_2 cycloaddition with styrene oxide over different catalysts.[109]

and MOF-74-Co) were used for photocatalytic CO_2 reduction.[367] Interestingly, when the CO_2 partial pressure was reduced to 0.1 atm, only MAF-X27-OH exhibited a high CO TOF of 23×10^{-3} s^{-1} with an unaltered CO selectivity (97.2%) compared to the TOF at 1 atm CO_2 (28×10^{-3} s^{-1}) (Fig. 27c). Periodic density functional theory (PDFT) simulations revealed that the μ-OH coordinated on the open Co sites of MAF-X27-OH stabilized the Co-CO_2 adduct by strong hydrogen bonding and promoted CO_2 reduction. Furthermore, it was observed that MAF-X27-OH bound CO_2 more strongly than H_2O (Fig. 27d). This suppressed H_2 (the byproduct) production and ensured high CO selectivity. A similar phenomenon was observed in monolayers of a Ni metal–organic framework (Ni MOLs).[374] In simulated flue-gas (10% CO_2), the photocatalytic activity and selectivity of Ni MOLs was nearly equivalent to those obtained in pure CO_2 due to the stronger adsorption energy of CO_2 (−200.11 kJ mol^{-1}) on Ni MOLs than H_2O (−62.47 kJ mol^{-1}). As a final example, a Cu(II)-MOF with high density of LASs and LBSs exhibited remarkable CO_2 volumetric uptake (171 cm^3 cm^{-3} at 298 K and 1 atm) and excellent CO_2/N_2 selectivity (51 for the 15/85 v/v mixture at 1 atm) due to the cooperation of multiple active sites.[109] The MOF, FJI-H14, was then employed to catalyze CO_2 cycloaddition reactions using 1 atm simulated post-combustion flue gas ($CO_2 : N_2 = 15 : 85$) as a feedstock. The material exhibited a desirable product yield (86%), outperforming the copper salt ($Cu(OAc)_2$), the physical mixture of the copper salt ($Cu(NO_3)_2$) and the H_2BTTa linker, as well as a typical Cu(II)-based MOF (HKUST-1) (Fig. 27e), again providing evidence for the synergistic effects between LASs and LBSs.

5. Conclusions and perspectives

The development of MOF-based materials has opened a door leading to a new set of promising adsorbents and catalysts for CO_2 capture and conversion. Keys to the successful implementation of MOFs as CO_2 adsorbents lie in their chemical tunabilities that improve interactions with the gaseous molecule and even other substrates. These interactions are mostly between CO_2 and open metal sites, Lewis basic sites, polar functional groups, and/or micropores. Exploration of these interactions has precipitated magnificent adsorption capacities and selective CO_2 capture in the presence of N_2, CH_4, and H_2O, among other gases. Furthermore, given the challenges involved with the introduction of certain functional groups into MOFs by *de novo* syntheses, various post-synthetic strategies, such as post-synthetic modification and the construction of MOF composites, have been developed. Large-scale application of MOFs to CO_2 capture remains subject to research to address further improvements of selectivity in the presence of water or acidic gases. It is incumbent upon researchers to choose the appropriate MOFs for the desired performance.

Many classes of reactions for CO_2 conversion have been explored over MOFs, mainly including CO_2 organic transformation, CO_2 hydrogenation, photocatalytic CO_2 reduction, and electrocatalytic CO_2 reduction. Beyond that, MOFs can be combined with other materials or used as precursors to synthesize MOF composites and MOF derivatives, respectively. Generally, the catalytic efficiencies of MOF-based materials are favorable. This can be attributed to the following factors: (a) the relatively high surface areas and porous structures stabilize the catalytically active moieties and prevent deactivation while guaranteeing mass transfer and electron migration; (b) the synergetic effects from multiple functionalities can activate CO_2 and/or substrate molecules, facilitating CO_2 conversion; (c) based on their specific compositions, MOF composites and derivatives exhibit enhanced electrical conductivities, visible-light absorbance, and/or stabilities further expanding potential applications of catalysts.

These MOF-based materials would not be efficient catalysts, however, if it were not for their high CO_2 capture capacities. Thus, the relationship between the CO_2 capture capacity of MOF-based materials and their catalytic CO_2 conversion performance is critical. In this review, we have highlighted this importance in three manners: (a) in contrast to homogeneous catalysts, the local CO_2 concentration at catalytically active sites can be vastly increased by the CO_2 capture capabilities of MOF-based materials, boosting reaction yields and selectivities; (b) certain functional groups in MOFs not only improve the CO_2 uptake capacities but also activate CO_2 molecules and/or other reactants, further enhancing the catalytic efficiencies of MOF-based materials; (c) the high CO_2 adsorption selectivities of MOF-based materials can endow them with high catalytic activities and selectivities even in mixed gas environments with low CO_2 concentrations or partial pressures. Therefore, in the future, the synthesis of MOF-based materials with outstanding CO_2 uptake capacities and selectivities must be tied in with the development of catalytic CO_2 conversion.

Although dramatic advances have been made in the last ten years, this field is still in its infancy. This is especially true in regards to CO_2 hydrogenation, photocatalytic CO_2 reduction, and electrocatalytic CO_2 reduction. Many open issues remain that should be addressed as MOF-based CO_2 conversion catalysts undergo further development. First, a plethora of reported catalytic CO_2 conversion reactions are carried out under harsh conditions. For example, some organic transformations and CO_2 photoreduction reactions are performed in alkaline environments,[3] and CO_2 hydrogenation is mainly carried out at high temperatures. Fortunately, great progress on this topic has been achieved in recent years. Also, as we have demonstrated, most MOF-based catalytic systems still require the presence of co-catalysts or electron sacrificial agents. Although these compounds significantly boost the performance of MOF-based catalysts, they can also serve to pollute the environment or consume/sacrifice active sites, making the materials less efficient. Therefore, it is important that future studies focus on integrating these active species into the frameworks or mitigating the need for additional reagents whatsoever. Unfortunately, the catalytic efficiencies of many MOF-based materials featuring mainly micropores are restricted by mass transfer. To address this issue, 2D MOFs and hierarchically porous MOFs might be worthy of further investigation. As for the stability of materials, cycling performance tests might not be sufficient to prove that the catalysts are permanently stable.

2816 | Chem. Soc. Rev., 2019, 48, 2783–2828

This journal is © The Royal Society of Chemistry 2019

As the field moves toward the industrial application phase, the reproducibility of reported catalytic activities and long-term stability of MOF-based catalysts should be evaluated more thoroughly. Finally, while MOFs with well-defined structures are beneficial when it comes to mechanistic understanding, advanced characterization and multi-dimensional *in operando* reactions are still important. Therefore, in order to understand the reaction mechanisms involved with CO_2 conversion in MOF-based catalysts and further push to practical application in the future, it is likely that this ongoing research will require collaboration between scientists from different disciplines including theoretical, synthetic, and physical chemistry, chemical engineering, and physics.

MOF-based materials are already showing great promise as the next-generation of CO_2 capture and conversion systems. That is evidenced not only by the examples we detailed in this review, but also in the speed with which the field is advancing. We foresee additional rapid growth as there are numerous opportunities to design, synthesize, characterize, and utilize MOF-based materials for this set of critical applications.

List of acronyms and abbreviations

abtc	(*E*)-5,5′-(Diazene-1,2-diyl)diisophthalate
ad	Adenine
atz	(1*H*-1,2,4-Triazol-3-yl)amide
AzDC	4,4′-Azobenzenedicarboxylate
bbta	1*H*,5*H*-Benzo-(1,2-*d*:4,5-*d*′)bistriazole
BDC	1,4-Benzenedicarboxylate
BDC-allyl	2-Allylterephthalate
BDPO	5,5′-((1,3,5-Triazine-2,4-diyl)bis(azanediyl))-bis(4-hydroxyisophthalate)
bIM	Benzimidazolate
BPDC	Biphenyl-1,4-dicarboxylate
4,4′-BPE	*trans*-Bis(4-pyridyl)ethylene
BPT	Biphenyl-3,4′,5-tricarboxylate
bpta	3,6-Di(4-pyridyl)-1,2,4,5-tetrazine
bpy	2,2′-Bipyridine
4,4′-bpy	4,4′-Bipyridine
bpydc	(2,2′-Bipyridine)-5,5′-dicarboxylate
BPZNO₂	5-Nitro-[4,4′-bipyrazole]-1,1′-diide
BTB	1,3,5-Benzenetribenzoate
btc	Benzene-1,3,5-tricarboxylate
btei	4,4′,4″-(Benzene-1,3,5-triyltris(ethyne-2,1-diyl))tribenzoate
btm	Bis(5-methyl-1*H*-1,2,4-triazol-3-yl)methane
1,2,4,5-BTMS	1,2,4,5-Benzenetetramethanesulfonate
bptc	3,3′,5,5′-Biphenyltetracarboxylate
BTT	1,3,5-Benzenetristetrazolate
BTTA	2,5-Di(1*H*-1,2,4-triazol-1-yl)terephthalate
catbdc	2,3-Dihydroxyterephthalate
γ-CD	γ-Cyclodextrin
CEB	4-(2-Carboxylatoethyl)benzoate
CVB	(*E*)-4-(2-Carboxylatovinyl)benzoate
dabco	1,4-Diazabicyclo[2.2.2]octane
dcbpy	2,2′-Bipyridine-4,4′-dicarboxylate
DCDPS	4,4′-Dicarboxydiphenyl sulfone
dhbdc	2,5-Dihydroxybenzene-1,4-dicarboxylate
DH₃PhDC	3,3″-Dihydroxy-2′,5′-dimethyl-[1,1′:4′,1″-terphenyl]-4,4″-dicarboxylate
dobdc	2,5-Dihydroxyterephthalate
dobpdc	4,4′-Dioxido-3,3′-biphenyldicarboxylate
dondc	1,5-Dioxido-2,6-naphthalenedicarboxyliate
dotpdc	4,4″-Dioxido-[1,1′:4′,1″-terphenyl]-3,3″-dicarboxylate
dpe	1,2-Di(4-pyridyl)ethylene
dpt24	3-(2-Pyridyl)-5-(4-pyridyl)-1,2,4-triazolate
dtp	2,3-Di-1*H*-tetrazol-5-ylpyrazine
EDS	1,2-Ethanedisulfonate
FMA	Fumarate
H₄cit	Citric acid
H₆CPB	1′,2′,3′,4′,5′,6′-Hexakis-(4-carboxyphenyl)benzene
H₁₀TBCPPP	Tetrakis-3,5-bis[(4-carboxy)phenyl]phenyl porphine
Im-BDC	2-(1*H*-Imidazol-1-yl)terephthalate
L1	3,3′-(Perfluoropropane-2,2-diyl)dibenzoate
L2	5-Carbamoyl-4-(iminooxidomethyl)-2-methylimidazol-1-ide
L3	2,5-Bis(2-methoxyethoxy)isophthalate
L4	2-(2-Methoxyethoxy)isophthalate
L-Pro	L-proline
L-Ru	Bis(2,2′-bipyridine)[5,5′-di(4-carboxyl-phenyl)-2,2′-bipyridine]ruthenium(II) dichloride
mdpt24	3-(3-Methyl-2-pyridyl)-5-(4-pyridyl)-1,2,4-triazolate
MeIM	2-Methylimidazole
nbIm	5-Nitro benzimidazole
NDC	2,6-Naphthalenedicarboxylate
1,4-ndc	Naphthalene-1,4-dicarboxylate
NH₂-BDC	2-Amino-1,4-benzene dicarboxylate
NH₂-BPY	NH₂-Bipyridine
nIm	2-Nitroimidazole
ntei	4,4′,4″-((Nitrilotris(benzene-4,1-diyl))-tris(ethyne-2,1-diyl))tribenzoate
OBB	4,4′-Oxybis(benzoate)
pbdc	5-Phosphonatoisophthalate
PhIM	Benzimidazole
ppy	2-Phenylpyridine
ptei	4,4′-((5′-(4-((4-Carboxylatophenyl)-ethynyl)phenyl)-[1,1′:3′,1″-terphenyl]-4,4″-diyl)bis(ethyne-2,1-diyl))-dibenzoate
4Pyc	4-Pyridylcarboxylate
rctt-tpcb	*region-cis*, *trans*, *trans*-tetrakis(4-pyridyl)cyclo-butane
Sbpdc	Dibenzo[*b,d*]thiophene-3,7-dicarboxylate 5,5-dioxide
(*S,S*)-methox	Bis[(*S*)-methionine]oxalyl diamide
tactmb	1,4,7,10-Tetrazazcyclododecane-*N*,*N*′,*N*″,*N*′′′-tetra-*p*-methylbenzoate

TBAPy	4,4′,4″,4‴-(Pyrene-1,3,6,8-tetrayl)tetrabenzoate	MAF-23	[Zn$_2$(btm)$_2$]
$^{t\text{Bu}}$PNP	2,6-Bis((di-*tert*-butylphosphino)methyl)pyridine	MAF-25	[Co(dpt24)$_2$]
		MAF-26	[Co(mdpt24)$_2$]
TCDC	2,3,5,6-Tetrachloroterephthalate	MAF-66	[Zn(atz)$_2$]
TCPBDA	4,4′,4″,4‴-([1,1′-Biphenyl]-4,4′-diylbis(azanetriyl))tetrabenzoate	MAF-X27-Cl	[Co$_2$(μ-Cl)$_2$(bbta)]
		MAF-X27-OH	[Co$_2$(μ-OH)$_2$(bbta)]
TCPE	4,4′,4″,4‴-(Ethene-1,1,2,2-tetrayl)tetrabenzoate	MIL-68(In)	In(OH)(BDC)
		MIL-100(Fe)	Fe$_3$O(H$_2$O)$_2$F{C$_6$H$_3$(CO$_2$)$_3$}$_2$·nH$_2$O ($n \approx$ 14.5)
TCPP	Tetrakis(4-carboxyphenyl)porphyrin	MIL-101	Cr$_3$F(H$_2$O)$_2$O(BDC)$_3$·nH$_2$O ($n \approx$ 25)
TCPP-Co	Tetrakis(4-carboxyphenyl)porphyrin-Co	MIL-101(Fe)	Fe$_3$F(H$_2$O)$_2$O(BDC)$_3$
TDPAT	5,5′,5″-((1,3,5-Triazine-2,4,6-triyl)tris(azanediyl))triisophthalate	MIL-102	Cr$_6^{\text{III}}$O$_2${H$_2$O}$_4$F$_2${C$_{10}$H$_4$(CO$_2$)$_4$}$_3$
		MMCF-2	[Cu$_2$(Cu-tactmb)(H$_2$O)$_3$(NO$_3$)$_2$]
terpy	2,2′:6′,2″-Terpyridine	M-MOF-74	[M$_2$(dobdc)(H$_2$O)$_2$] (M = M = Mg^{2+}, Ni^{2+}, Co^{2+}, Zn^{2+})
THPP-Co	5,10,15,20-Tetrakis(3,4,5-trihydroxyphenyl)porphyrin-Co		
		MOF-5	[Zn$_4$O(BDC)$_3$]
THPP-Fe	5,10,15,20-Tetrakis(3,4,5-trihydroxyphenyl)porphyrin-Fe	MOF-74-Co	[Co$_2$(dobdc)]
		MOF-177	[Zn$_4$O(BTB)$_2$]
TMPyP	*meso*-Tetra(*N*-methyl-4-pyridyl) porphine tetratosylate	MOF-253	[Al(OH)(bpydc)]
		MOF-505	[Cu$_2$(bptc)(H$_2$O)$_2$(DMF)$_3$(H$_2$O)]
tpt	2,4,6-Tri(4-pyridyl)-1,3,5-triazine	MOF-525	Zr$_6$O$_4$(OH)$_8$(TCPP)$_2$
Tz	3,5-Bis(trifluoromethyl)-1,2,4-triazolate	MOF-525-Co	Zr$_6$O$_4$(OH)$_8$(TCPP-Co)$_2$
Tz-Bz	4-(1*H*-1,2,4-Triazol-1-yl)benzoic acid	MOF-525(Fe)	Zr$_6$O$_4$(OH)$_8$(TCPP-Fe)$_2$
Al-TCPP-Co	[Al$_2$(OH)$_2$TCPP-Co]	MOF-892	[Zr$_6$O$_4$(OH)$_4$(H$_2$CPB)$_{1.5}$(CH$_3$CO$_2$)$_6$]
BIF-20	Zn$_2$(BH(MeIM)$_3$)$_2$(OBB)	NH$_2$-MIL-53	[Al(OH)(NH$_2$-BDC)]$_n$
BiO-MOF-1	Zn$_8$(ad)$_4$(BPDC)$_6$O·2Me$_2$NH$_2$	NH$_2$-MIL-53(Fe)	Fe(OH)(NH$_2$-BDC)
bio-MOF-11	Co$_2$(ad)$_2$(CO$_2$CH$_3$)$_2$·2DMF·0.5H$_2$O	NH$_2$-MIL-88B(Fe)	Fe$_3$O(solvent)$_3$Cl(NH$_2$-BDC)$_3$(solvent)$_m$
CAU-1	Al$_4$(OH)$_2$(OCH$_3$)$_4$(NH$_2$-BDC)$_3$	NH$_2$-MIL-101(Fe)	Fe$_3$F(H$_2$O)$_2$O(NH$_2$-BDC)$_3$
CD-MOF-2	[(C$_{48}$H$_{80}$O$_{40}$)(RbOH)$_2$]	NH$_2$-MIL-125	[Ti$_8$O$_8$(OH)$_4$(NH$_2$-BDC)$_6$]
CPF	Zn(HBTT)	NH$_2$-UiO-66	[Zr$_6$O$_4$(OH)$_4$(NH$_2$-BDC)$_6$]
CPM-5	[(CH$_3$)$_2$NH$_2$][In$_3$O(BTC)$_2$(H$_2$O)$_3$]$_2$-[In$_3$(BTC)$_4$]·7DMF·23H$_2$O	Ni-4PyC	Ni$_9$(m-H$_2$O)4(H$_2$O)$_2$(C$_6$H$_4$O$_2$)$_{18}$
		NOT-140	[Cu$_4$L(H$_2$O)$_4$]·10DMF·C$_4$H$_8$O$_2$·8H$_2$O (L = 4′,4‴,4‴″,4‴″″-methanetetrayltetrakis(([1,1′-biphenyl]-4-carboxylate)))
CPM-33a	Ni$_3$OH(bdc)$_3$tpt		
CPM-33b	Ni$_3$OH(dhbdc)$_3$tpt		
CPM-33c	Ni$_3$OH(NH$_2$-BDC)$_3$tpt		
CPM-33d	Ni$_3$OH(1,4-ndc)$_3$tpt	NOTT-202	(Me$_2$NH$_2$)$_{1.75}$[In(L)]$_{1.75}$(DMF)$_{12}$(H$_2$O)$_{10}$ (H$_4$L = biphenyl-3,3′,5,5′-tetra-(phenyl-4-carboxylic acid))
Cu-TDPAT	[Cu$_3$(TDPAT)(H$_2$O)$_3$]·10H$_2$O5DMA		
ELM-11	[Cu(4,4′-bpy)$_2$(BF$_4$)$_2$]		
Fe-BTT	Fe$_3$[(Fe$_4$Cl)$_3$(BTT)$_8$]$_2$	NU-1000	[Zr$_6$(μ$_3$-O)$_4$(μ$_3$-OH)$_4$]$_2$(TBAPy)$_6$
FJI-H14	[Cu(BTTA)]$_n$	PCN-61	Cu$_3$(H$_2$O)$_3$(btei)
FMOF-1	{Ag$_2$[Ag$_4$Tz$_6$]}	PCN-66	Cu$_3$(H$_2$O)$_3$(ntei)
Hf-NU-1000	[Hf$_6$(μ$_3$-O)$_4$(μ$_3$-OH)$_4$]$_2$(TBAPy)$_6$	PCN-68	Cu$_3$(H$_2$O)$_3$(ptei)
Hf$_{12}$–Ru	Hf$_{12}$(μ$_3$-O)$_8$(μ$_3$-OH)$_8$(μ$_2$-OH)$_6$(TFA)$_6$(L-Ru)$_6$	PCN-123	[Zn$_4$O(L)$_3$] (L = 2-(phenyldiazenyl)terephthalate)
HKUST-1	[Cu$_3$(btc)$_2$(H$_2$O)$_3$]		
IFMC-1	[Zn(HL)] (H$_3$L = 4,5-di(1*H*-tetrazol-5-yl)-2*H*-1,2,3-triazole)	PCN-222	Zr$_6$(μ$_3$-OH)$_8$(OH)$_8$-(TCPP)$_2$
		PCN-900(Eu)	[(CH$_3$)$_2$NH$_2$]$_2$[Eu$_6$(μ$_3$-OH)$_8$(TCPP)$_{1.5}$(DCDPS)$_3$]·(solvent)$_x$
IISERP-MOF4	Mg(Tz-Bz)(CH$_3$COO)		
Im-UiO-66	[Zr$_6$O$_4$(OH)$_4$(Im-BDC)$_6$]	PCN-900(Eu)-BPYDC	
Ir-CP	Y[Ir(ppy)$_2$(dcbpy)]$_2$[OH]		[(CH$_3$)$_2$NH$_2$]$_2$[Eu$_6$(μ$_3$-OH)$_8$](TCPP)$_{1.5}$(BPYDC)$_3$
IRMOF-3	[Zn$_4$O(NH$_2$-BDC)$_3$]	PCN-900(Eu)-CoTCPP	
IRMOF-74-III	[Mg$_2$(DH$_3$PhDC)]		[(CH$_3$)$_2$NH$_2$]$_2$[Eu$_6$(μ$_3$-OH)$_8$](CoTCPP)$_{1.5}$-(DCDPS)$_3$
JUC-1000	[Cu$_{24}$(BDPO)$_{12}$(H$_2$O)$_{12}$]·30DMF·14H$_2$O		
LIFM-26	Fe$_3$(TCDC)$_3$(H$_2$O)$_3$	PCN-900(Eu)-CoTCPP-CoBPYDC	
LIFM-28	[Zr$_6$(μ$_3$-O)$_8$-(H$_2$O)$_8$(L^1)$_4$] (L^1 = 2,2′-bis(trifluoromethyl)-4,4′-biphenyldicarboxylate)		[(CH$_3$)$_2$NH$_2$]$_2$[Eu$_6$(μ$_3$-OH)$_8$](CoTCPP)$_{1.5}$-(CoBPYDC)$_3$
		porph@MOM-11	[Cd$_4$(BPT)$_4$]·[Cd(TMPYP)]
		Re$_3$-MOF	Zr$_6$O$_4$(OH)$_4$[Re(CO)$_3$(bpydc)Cl]$_{0.72}$(BPDC)$_{5.28}$
		SHF-61	(Me$_2$NH$_2$)[In(NH$_2$-BDC)$_2$]

2818 | *Chem. Soc. Rev.*, 2019, **48**, 2783–2828

This journal is © The Royal Society of Chemistry 2019

SNU-5	$\{Cu_2(abtc)\}_3$
SNU-30	$\{[Zn_2(TCPBDA)-(H_2O)_2]\cdot30DMF\cdot6H_2O\}_n$
SNU-31	$\{[Zn_2-(TCPBDA)(bpta)]\cdot23DMF\cdot4H_2O\}_n$
SNU-70	$[Zn_4O-(CVB)_3]\cdot13DEF\cdot2H_2O$
SNU-71	$[Zn_4O-(CEB)_3]\cdot6DEF\cdot H_2O$
SUMOF-2	$[Zn_4O(BDC)_3]\cdot(ZnO)_{0.125}$
SUMOF-3	$[Zn_4O(NDC)_3]$
SUMOF-4	$[Zn_4O(BDC)_2(BPDC)(H_2O)]$
TMOF-1	$[Cu(4,4'-bpy)_2(EDS)]_n$
TMOF-3	$[Cu(bpy)_2(1,2,4,5-BTMS)_{0.5}(H_2O)_{0.5}]_n$
UiO-66	$[Zr_6O_4(OH)_4(BDC)_6]$
UiO-66-allyl	$[Zr_6O_4(OH)_4(BDC-allyl)_6]$
UiO-67	$[Zr_6O_4(OH)_4(BPDC)_6]$
UiO-bpy	$Zr6(\mu_3-O)_4(\mu_3-OH)_4(\mu_1-OH)(H_2O)-(bpydc)_5(HCO_2)$
USTC-253	$[Al(OH)(Sbpdc)]$
UTSA-16	$[K(H_2O)_2Co_3(cit)(Hcit)]$
ZIF-7	$Zn(bIM)_2$
ZIF-8	$Zn(MeIM)_2$
ZIF-9	$Co(PhIM)_2$
ZIF-67	$Co(MeIM)_2$
ZIF-78	$Zn(nbIm)(nIm)$
ZIF-108	ZIF-8: $Zn(nIm)_2$
ZJNU-40	$[Cu_2L(H_2O)_2]$ (L = 5,5'-(benzo[c][1,2,5]thiadiazole-4,7-diyl)diisophthalate)
ZJNU-43	$[Cu_2L_1(H_2O)_2]\cdot3DMF\cdot2EtOH\cdot4H_2O$ (L_1 = 5,5'-(quinoline-5,8-diyl)-diisophthalate)
ZJNU-44	$([Cu_2L_2(H_2O)_2]\cdot3DMF\cdot3CH_3CN\cdot3H_2O)$ (L_2 = 5,5'-(isoquinoline-5,8-diyl)-diisophthalate)
ZJNU-45	$([Cu_2L_3(H_2O)_2]\cdot3DMF\cdot3MeOH\cdot3H_2O)$ (L_3 = 5,5'-(quinoxaline-5,8-diyl)-diisophthalate)
ZnGlu	$\{[Zn(H_2O)(C_5H_7NO_4)]\cdot H_2O\}_n$
ZnPC-2	$\{[Zn_3(pbdc)_2]_2H_3O\}_n$
ZrPP-1-Co	$[Zr_2(THPP-Co)]_n$
ZTF-1	$[Zn(CN_5H_2)_2]$

Conflicts of interest

There are no conflicts to declare.

Acknowledgements

References

1 Q. Wang, J. Luo, Z. Zhong and A. Borgna, *Energy Environ. Sci.*, 2011, **4**, 42–55.

2 E. S. Sanz-Pérez, C. R. Murdock, S. A. Didas and C. W. Jones, *Chem. Rev.*, 2016, **116**, 11840–11876.

3 M. Mikkelsen, M. Jørgensen and F. C. Krebs, *Energy Environ. Sci.*, 2010, **3**, 43–81.

4 L. Zhang, Z.-J. Zhao and J. Gong, *Angew. Chem., Int. Ed.*, 2017, **56**, 11326–11353.

5 Carbon dioxide: projected emissions and concentrations, 2014, http://ipcc-data.org/observ/ddc_co2.html.

6 D. M. D'Alessandro, B. Smit and J. R. Long, *Angew. Chem., Int. Ed.*, 2010, **49**, 6058–6082.

7 J. Wang, L. Huang, R. Yang, Z. Zhang, J. Wu, Y. Gao, Q. Wang, D. O'Hare and Z. Zhong, *Energy Environ. Sci.*, 2014, **7**, 3478–3518.

8 G. Sneddon, A. Greenaway and H. H. P. Yiu, *Adv. Energy Mater.*, 2014, **4**, 1301873.

9 G. Cui, J. Wang and S. Zhang, *Chem. Soc. Rev.*, 2016, **45**, 4307–4339.

10 Y. Zhang and J. Y. G. Chan, *Energy Environ. Sci.*, 2010, **3**, 408–417.

11 Y. Li, L. Li and J. Yu, *Chem*, 2017, **3**, 928–949.

12 Y. Xie, T.-T. Wang, X.-H. Liu, K. Zou and W.-Q. Deng, *Nat. Commun.*, 2013, **4**, 1960.

13 X. Feng, X. Ding and D. Jiang, *Chem. Soc. Rev.*, 2012, **41**, 6010–6022.

14 A. Schoedel, Z. Ji and O. M. Yaghi, *Nat. Energy*, 2016, **1**, 16034.

15 C. A. Trickett, A. Helal, B. A. Al-Maythalony, Z. H. Yamani, K. E. Cordova and O. M. Yaghi, *Nat. Rev. Mater.*, 2017, **2**, 17045.

16 S. Wang and X. Wang, *Angew. Chem., Int. Ed.*, 2016, **55**, 2308–2320.

17 J. R. Long and O. M. Yaghi, *Chem. Soc. Rev.*, 2009, **38**, 1213–1214.

18 H.-C. Zhou, J. R. Long and O. M. Yaghi, *Chem. Rev.*, 2012, **112**, 673–674.

19 H.-C. Zhou and S. Kitagawa, *Chem. Soc. Rev.*, 2014, **43**, 5415–5418.

20 M. Eddaoudi, D. B. Moler, H. Li, B. Chen, T. M. Reineke, M. O'Keeffe and O. M. Yaghi, *Acc. Chem. Res.*, 2001, **34**, 319–330.

21 W. Lu, Z. Wei, Z.-Y. Gu, T.-F. Liu, J. Park, J. Park, J. Tian, M. Zhang, Q. Zhang, T. Gentle, M. Bosch and H.-C. Zhou, *Chem. Soc. Rev.*, 2014, **43**, 5561–5593.

22 J. S. Seo, D. Whang, H. Lee, S. I. Jun, J. Oh, Y. J. Jeon and K. Kim, *Nature*, 2000, **404**, 982–986.

23 L. Jiao, J. Y. R. Seow, W. S. Skinner, Z. U. Wang and H.-L. Jiang, *Mater. Today*, 2019, DOI: 10.1016/j.mattod.2018.10.038.

24 B. Li, H.-M. Wen, Y. Cui, W. Zhou, G. Qian and B. Chen, *Adv. Mater.*, 2016, **28**, 8819–8860.

25 A. Kirchon, L. Feng, H. F. Drake, E. A. Joseph and H.-C. Zhou, *Chem. Soc. Rev.*, 2018, **47**, 8611–8638.

26 H. Kitagawa, *Nat. Chem.*, 2009, **1**, 689–690.

27 S. Kitagawa, R. Kitaura and S.-I. Noro, *Angew. Chem., Int. Ed.*, 2004, **43**, 2334–2375.

This journal is © The Royal Society of Chemistry 2019

Chem. Soc. Rev., 2019, **48**, 2783–2828 | **2819**

28 B. Chen, S. Xiang and G. Qian, *Acc. Chem. Res.*, 2010, **43**, 1115–1124.

29 A. Corma, H. García and F. X. Llabrés i Xamena, *Chem. Rev.*, 2010, **110**, 4606–4655.

30 S. Ma and H.-C. Zhou, *Chem. Commun.*, 2010, **46**, 44–53.

31 H.-L. Jiang and Q. Xu, *Chem. Commun.*, 2011, **47**, 3351–3370.

32 Z.-G. Gu, C. Zhan, J. Zhang and X. Bu, *Chem. Soc. Rev.*, 2016, **45**, 3122–3144.

33 P. Horcajada, R. Gref, T. Baati, P. K. Allan, G. Maurin, P. Couvreur, G. Férey, R. E. Morris and C. Serre, *Chem. Rev.*, 2012, **112**, 1232–1268.

34 A. J. Howarth, Y. Liu, P. Li, Z. Li, T. C. Wang, J. T. Hupp and O. K. Farha, *Nat. Rev. Mater.*, 2016, **1**, 15018.

35 J.-R. Li, J. Sculley and H.-C. Zhou, *Chem. Rev.*, 2012, **112**, 869–932.

36 M. P. Suh, H. J. Park, T. K. Prasad and D.-W. Lim, *Chem. Rev.*, 2012, **112**, 782–835.

37 K. Sumida, D. L. Rogow, J. A. Mason, T. M. McDonald, E. D. Bloch, Z. R. Herm, T.-H. Bae and J. R. Long, *Chem. Rev.*, 2012, **112**, 724–781.

38 A. Schneemann, V. Bon, I. Schwedler, I. Senkovska, S. Kaskel and R. A. Fischer, *Chem. Soc. Rev.*, 2014, **43**, 6062–6096.

39 L. Sun, M. G. Campbell and M. Dincă, *Angew. Chem., Int. Ed.*, 2016, **55**, 3566–3579.

40 H. Furukawa, K. E. Cordova, M. O'Keeffe and O. M. Yaghi, *Science*, 2013, **341**, 1230444.

41 S. Dissegna, K. Epp, W. R. Heinz, G. Kieslich and R. A. Fischer, *Adv. Mater.*, 2018, 1704501.

42 Y. Cui, J. Zhang, H. He and G. Qian, *Chem. Soc. Rev.*, 2018, **47**, 5740–5785.

43 P. Nugent, Y. Belmabkhout, S. D. Burd, A. J. Cairns, R. Luebke, K. Forrest, T. Pham, S. Ma, B. Space, L. Wojtas, M. Eddaoudi and M. J. Zaworotko, *Nature*, 2013, **495**, 80–84.

44 J. Gascon, A. Corma, F. Kapteijn and F. X. Llabrés i Xamena, *ACS Catal.*, 2014, **4**, 361–378.

45 A. Dhakshinamoorthy, A. M. Asiri and H. García, *Angew. Chem., Int. Ed.*, 2016, **55**, 5414–5445.

46 C. Wang, Z. Xie, K. E. deKrafft and W. Lin, *J. Am. Chem. Soc.*, 2011, **133**, 13445–13454.

47 Z. Zhang, Z.-Z. Yao, S. Xiang and B. Chen, *Energy Environ. Sci.*, 2014, **7**, 2868–2899.

48 Z. Hu, B. J. Deibert and J. Li, *Chem. Soc. Rev.*, 2014, **43**, 5815–5840.

49 J. Liu, L. Chen, H. Cui, J. Zhang, L. Zhang and C.-Y. Su, *Chem. Soc. Rev.*, 2014, **43**, 6011–6061.

50 P. Ramaswamy, N. E. Wong and G. K. H. Shimizu, *Chem. Soc. Rev.*, 2014, **43**, 5913–5932.

51 M. Zhang, G. Feng, Z. Song, Y.-P. Zhou, H.-Y. Chao, D. Yuan, T. T. Y. Tan, Z. Guo, Z. Hu, B. Z. Tang, B. Liu and D. Zhao, *J. Am. Chem. Soc.*, 2014, **136**, 7241–7244.

52 T. Zhang and W. Lin, *Chem. Soc. Rev.*, 2014, **43**, 5982–5993.

53 W.-Y. Gao, H. Wu, K. Leng, Y. Sun and S. Ma, *Angew. Chem., Int. Ed.*, 2016, **55**, 5472–5476.

54 Q.-L. Zhu and Q. Xu, *Chem. Soc. Rev.*, 2014, **43**, 5468–5512.

55 S. S. Nagarkar, B. Joarder, A. K. Chaudhari, S. Mukherjee and S. K. Ghosh, *Angew. Chem., Int. Ed.*, 2013, **52**, 2881–2885.

56 Z. Lei, Y. Xue, W. Chen, W. Qiu, Y. Zhang, S. Horike and L. Tang, *Adv. Energy Mater.*, 2018, 1801587.

57 B. Van de Voorde, B. Bueken, J. Denayer and D. De Vos, *Chem. Soc. Rev.*, 2014, **43**, 5766–5788.

58 L. Wang, Y. Han, X. Feng, J. Zhou, P. Qi and B. Wang, *Coord. Chem. Rev.*, 2016, **307**, 361–381.

59 P. Hu, J. V. Morabito and C.-K. Tsung, *ACS Catal.*, 2014, **4**, 4409–4419.

60 P. Falcaro, R. Ricco, A. Yazdi, I. Imaz, S. Furukawa, D. Maspoch, R. Ameloot, J. D. Evans and C. J. Doonan, *Coord. Chem. Rev.*, 2016, **307**, 237–254.

61 C. M. Doherty, D. Buso, A. J. Hill, S. Furukawa, S. Kitagawa and P. Falcaro, *Acc. Chem. Res.*, 2014, **47**, 396–405.

62 J.-R. Li, Y. Ma, M. C. McCarthy, J. Sculle, J. Yu, H.-K. Jeong, P. B. Balbuena and H.-C. Zhou, *Coord. Chem. Rev.*, 2011, **255**, 1791–1823.

63 R. Li, W. Zhang and K. Zhou, *Adv. Mater.*, 2018, 1705512.

64 Z. Liang, C. Qu, D. Xia, R. Zou and Q. Xu, *Angew. Chem., Int. Ed.*, 2018, **57**, 9604–9633.

65 M. H. Beyzavi, C. J. Stephenson, Y. Liu, O. Karagiaridi, J. T. Hupp and O. K. Farha, *Front. Energy Res.*, 2015, **2**, 63.

66 H. He, J. A. Perman, G. Zhu and S. Ma, *Small*, 2016, **12**, 6309–6324.

67 J. W. Maina, C. Pozo-Gonzalo, L. Kong, J. Schütz, M. Hill and L. F. Dumée, *Mater. Horiz.*, 2017, **4**, 345–361.

68 J. Liang, Y.-B. Huang and R. Cao, *Coord. Chem. Rev.*, 2019, **378**, 32–65.

69 Q. Yang, Q. Xu and H.-L. Jiang, *Chem. Soc. Rev.*, 2017, **46**, 4774–4808.

70 L. Jiao, Y. Wang, H.-L. Jiang and Q. Xu, *Adv. Mater.*, 2018, **30**, 1703663.

71 L. Zhu, X.-Q. Liu, H.-L. Jiang and L.-B. Sun, *Chem. Rev.*, 2017, **117**, 8129–8176.

72 A. Dhakshinamoorthy, Z. Li and H. Garcia, *Chem. Soc. Rev.*, 2018, **47**, 8134–8172.

73 H. Zhang, J. Nai, L. Yu and X. W. Lou, *Joule*, 2017, **1**, 77–107.

74 B. Seoane, J. Coronas, I. Gascon, M. E. Benavides, O. Karvan, J. Caro, F. Kapteijn and J. Gascon, *Chem. Soc. Rev.*, 2015, **44**, 2421–2454.

75 J.-R. Li, R. J. Kuppler and H.-C. Zhou, *Chem. Soc. Rev.*, 2009, **38**, 1477–1504.

76 B. Li, M. Chrzanowski, Y. Zhang and S. Ma, *Coord. Chem. Rev.*, 2016, **307**, 106–129.

77 Z. Zhang, Y. Zhao, Q. Gong, Z. Li and J. Li, *Chem. Commun.*, 2013, **49**, 653–661.

78 J. Liu, P. K. Thallapally, B. P. McGrail, D. R. Brown and J. Liu, *Chem. Soc. Rev.*, 2012, **41**, 2308–2322.

79 Q.-G. Zhai, X. Bu, X. Zhao, D.-S. Li and P. Feng, *Acc. Chem. Res.*, 2017, **50**, 407–417.

80 J. Yu, L.-H. Xie, J.-R. Li, Y. Ma, J. M. Seminario and P. B. Balbuena, *Chem. Rev.*, 2017, **117**, 9674–9754.

81 M. S. Denny, J. C. Moreton, L. Benz and S. M. Cohen, *Nat. Rev. Mater.*, 2016, **1**, 16078.

82 T. Kitao, Y. Zhang, S. Kitagawa, B. Wang and T. Uemura, *Chem. Soc. Rev.*, 2017, **46**, 3108–3133.

83 J. Yao and H. Wang, *Chem. Soc. Rev.*, 2014, **43**, 4470–4493.

84 A. Aijaz, N. Fujiwara and Q. Xu, *J. Am. Chem. Soc.*, 2014, **136**, 6790–6793.

85 S. Gadipelli, W. Travis, W. Zhou and Z. Guo, *Energy Environ. Sci.*, 2014, **7**, 2232–2238.

86 S. Wang and X. Wang, *Small*, 2015, **11**, 3097–3112.

87 A. Mahmood, W. Guo, H. Tabassum and R. Zou, *Adv. Energy Mater.*, 2016, **6**, 1600423.

88 Y.-Z. Chen, R. Zhang, L. Jiao and H.-L. Jiang, *Coord. Chem. Rev.*, 2018, **362**, 1–23.

89 C. Wang, B. An and W. Lin, *ACS Catal.*, 2019, **9**, 130–146.

90 J.-D. Xiao and H.-L. Jiang, *Acc. Chem. Res.*, 2019, **52**, 356–366.

91 F.-Y. Yi, R. Zhang, H. Wang, L.-F. Chen, L. Han, H.-L. Jiang and Q. Xu, *Small Methods*, 2017, **1**, 1700187.

92 J.-D. Xiao and H.-L. Jiang, *Small*, 2017, **13**, 1700632.

93 H. Li, M. Eddaoudi, T. L. Groy and O. M. Yaghi, *J. Am. Chem. Soc.*, 1998, **120**, 8571–8572.

94 H. Li, M. Eddaoudi, M. O'Keeffe and O. M. Yaghi, *Nature*, 1999, **402**, 276–279.

95 M. Eddaoudi, H. Li and O. M. Yaghi, *J. Am. Chem. Soc.*, 2000, **122**, 1391–1397.

96 H. Li, C. E. Davis, T. L. Groy, D. G. Kelley and O. M. Yaghi, *J. Am. Chem. Soc.*, 1998, **120**, 2186–2187.

97 B. Chen, M. Eddaoudi, T. M. Reineke, J. W. Kampf, M. O'Keeffe and O. M. Yaghi, *J. Am. Chem. Soc.*, 2000, **122**, 11559–11560.

98 A. R. Millward and O. M. Yaghi, *J. Am. Chem. Soc.*, 2005, **127**, 17998–17999.

99 T. M. McDonald, W. R. Lee, J. A. Mason, B. M. Wiers, C. S. Hong and J. R. Long, *J. Am. Chem. Soc.*, 2012, **134**, 7056–7065.

100 O. K. Farha, A. Özgür Yazaydın, I. Eryazici, C. D. Malliakas, B. G. Hauser, M. G. Kanatzidis, S. T. Nguyen, R. Q. Snurr and J. T. Hupp, *Nat. Chem.*, 2010, **2**, 944–948.

101 D. Yuan, D. Zhao, D. Sun and H.-C. Zhou, *Angew. Chem., Int. Ed.*, 2010, **49**, 5357–5361.

102 T. Loiseau, L. Lecroq, C. Volkringer, J. Marrot, G. Férey, M. Haouas, F. Taulelle, S. Bourrelly, P. L. Llewellyn and M. Latroche, *J. Am. Chem. Soc.*, 2006, **128**, 10223–10230.

103 Y.-G. Lee, H. R. Moon, Y. E. Cheon and M. P. Suh, *Angew. Chem., Int. Ed.*, 2008, **47**, 7741–7745.

104 Z. Guo, H. Wu, G. Srinivas, Y. Zhou, S. Xiang, Z. Chen, Y. Yang, W. Zhou, M. O'Keeffe and B. Chen, *Angew. Chem., Int. Ed.*, 2011, **50**, 3178–3181.

105 S. Surblé, F. Millange, C. Serre, T. Düren, M. Latroche, S. Bourrelly, P. L. Llewellyn and G. Férey, *J. Am. Chem. Soc.*, 2006, **128**, 14889–14896.

106 A. Demessence, D. M. D'Alessandro, M. L. Foo and J. R. Long, *J. Am. Chem. Soc.*, 2009, **131**, 8784–8786.

107 K. Sumida, S. Horike, S. S. Kaye, Z. R. Herm, W. L. Queen, C. M. Brown, F. Grandjean, G. J. Long, A. Dailly and J. R. Long, *Chem. Sci.*, 2010, **1**, 184–191.

108 J. R. Li, J. Yu, W. Lu, L. B. Sun, J. Sculley, P. B. Balbuena and H. C. Zhou, *Nat. Commun.*, 2013, **4**, 1538.

109 L. Liang, C. Liu, F. Jiang, Q. Chen, L. Zhang, H. Xue, H.-L. Jiang, J. Qian, D. Yuan and M. Hong, *Nat. Commun.*, 2017, **8**, 1233.

110 W. L. Queen, M. R. Hudson, E. D. Bloch, J. A. Mason, M. I. Gonzalez, J. S. Lee, D. Gygi, J. D. Howe, K. Lee, T. A. Darwish, M. James, V. K. Peterson, S. J. Teat, B. Smit, J. B. Neaton, J. R. Long and C. M. Brown, *Chem. Sci.*, 2014, **5**, 4569–4581.

111 C. Tan, S. Yang, N. R. Champness, X. Lin, A. J. Blake, W. Lewis and M. Schroder, *Chem. Commun.*, 2011, **47**, 4487–4489.

112 B. Mu, F. Li and K. S. Walton, *Chem. Commun.*, 2009, 2493–2495.

113 L. Hou, W.-J. Shi, Y.-Y. Wang, Y. Guo, C. Jin and Q.-Z. Shi, *Chem. Commun.*, 2011, **47**, 5464–5466.

114 Z. Zhang, S. Xiang, X. Rao, Q. Zheng, F. R. Fronczek, G. Qian and B. Chen, *Chem. Commun.*, 2010, **46**, 7205–7207.

115 Y.-X. Tan, Y.-P. He and J. Zhang, *Chem. Commun.*, 2011, **47**, 10647–10649.

116 A. Mallick, S. Saha, P. Pachfule, S. Roy and R. Banerjee, *J. Mater. Chem.*, 2010, **20**, 9073–9080.

117 Y. W. Li, J. R. Li, L. F. Wang, B. Y. Zhou, Q. Chen and X. H. Bu, *J. Mater. Chem. A*, 2013, **1**, 495–499.

118 P. D. C. Dietzel, V. Besikiotis and R. Blom, *J. Mater. Chem.*, 2009, **19**, 7362–7370.

119 X. Kong, E. Scott, W. Ding, J. A. Mason, J. R. Long and J. A. Reimer, *J. Am. Chem. Soc.*, 2012, **134**, 14341–14344.

120 S. R. Caskey, A. G. Wong-Foy and A. J. Matzger, *J. Am. Chem. Soc.*, 2008, **130**, 10870–10871.

121 H. Wu, J. M. Simmons, G. Srinivas, W. Zhou and T. Yildirim, *J. Phys. Chem. Lett.*, 2010, **1**, 1946–1951.

122 W. L. Queen, C. M. Brown, D. K. Britt, P. Zajdel, M. R. Hudson and O. M. Yaghi, *J. Phys. Chem. C*, 2011, **115**, 24915–24919.

123 P. D. C. Dietzel, R. E. Johnsen, H. Fjellvåg, S. Bordiga, E. Groppo, S. Chavan and R. Blom, *Chem. Commun.*, 2008, 5125–5127.

124 J. A. Mason, K. Sumida, Z. R. Herm, R. Krishna and J. R. Long, *Energy Environ. Sci.*, 2011, **4**, 3030–3040.

125 Z. R. Herm, J. A. Swisher, B. Smit, R. Krishna and J. R. Long, *J. Am. Chem. Soc.*, 2011, **133**, 5664–5667.

126 G. T. Rochelle, *Science*, 2009, **325**, 1652–1654.

127 N. MacDowell, N. Florin, A. Buchard, J. Hallett, A. Galindo, G. Jackson, C. S. Adjiman, C. K. Williams, N. Shah and P. Fennell, *Energy Environ. Sci.*, 2010, **3**, 1645–1669.

128 S. Couck, J. F. M. Denayer, G. V. Baron, T. Rémy, J. Gascon and F. Kapteijn, *J. Am. Chem. Soc.*, 2009, **131**, 6326–6327.

129 Q. Yang, A. D. Wiersum, P. L. Llewellyn, V. Guillerm, C. Serre and G. Maurin, *Chem. Commun.*, 2011, **47**, 9603–9605.

130 S.-N. Kim, J. Kim, H.-Y. Kim, H.-Y. Cho and W.-S. Ahn, *Catal. Today*, 2013, **204**, 85–93.

131 X. Si, C. Jiao, F. Li, J. Zhang, S. Wang, S. Liu, Z. Li, L. Sun, F. Xu, Z. Gabelica and C. Schick, *Energy Environ. Sci.*, 2011, **4**, 4522–4527.

This journal is © The Royal Society of Chemistry 2019

Chem. Soc. Rev., 2019, **48**, 2783–2828 | 2821

132 R. W. Flaig, T. M. O. Popp, A. M. Fracaroli, E. A. Kapustin, M. J. Kalmutzki, R. M. Altamimi, F. Fathieh, J. A. Reimer and O. M. Yaghi, *J. Am. Chem. Soc.*, 2017, **139**, 12125–12128.

133 A. M. Fracaroli, H. Furukawa, M. Suzuki, M. Dodd, S. Okajima, F. Gándara, J. A. Reimer and O. M. Yaghi, *J. Am. Chem. Soc.*, 2014, **136**, 8863–8866.

134 J. An, S. J. Geib and N. L. Rosi, *J. Am. Chem. Soc.*, 2010, **132**, 38–39.

135 B. Li, Z. Zhang, Y. Li, K. Yao, Y. Zhu, Z. Deng, F. Yang, X. Zhou, G. Li, H. Wu, N. Nijem, Y. J. Chabal, Z. Lai, Y. Han, Z. Shi, S. Feng and J. Li, *Angew. Chem., Int. Ed.*, 2012, **51**, 1412–1415.

136 T. M. McDonald, D. M. D'Alessandro, R. Krishna and J. R. Long, *Chem. Sci.*, 2011, **2**, 2022–2028.

137 R. Vaidhyanathan, S. S. Iremonger, G. K. H. Shimizu, P. G. Boyd, S. Alavi and T. K. Woo, *Science*, 2010, **330**, 650–653.

138 J.-B. Lin, J.-P. Zhang and X.-M. Chen, *J. Am. Chem. Soc.*, 2010, **132**, 6654–6656.

139 R. Vaidhyanathan, S. S. Iremonger, G. K. H. Shimizu, P. G. Boyd, S. Alavi and T. K. Woo, *Angew. Chem., Int. Ed.*, 2012, **51**, 1826–1829.

140 J.-S. Qin, D.-Y. Du, W.-L. Li, J.-P. Zhang, S.-L. Li, Z.-M. Su, X.-L. Wang, Q. Xu, K.-Z. Shao and Y.-Q. Lan, *Chem. Sci.*, 2012, **3**, 2114–2118.

141 P. Q. Liao, D. D. Zhou, A. X. Zhu, L. Jiang, R. B. Lin, J. P. Zhang and X. M. Chen, *J. Am. Chem. Soc.*, 2012, **134**, 17380–17383.

142 Q. Lin, T. Wu, S.-T. Zheng, X. Bu and P. Feng, *J. Am. Chem. Soc.*, 2012, **134**, 784–787.

143 C. Song, J. Hu, Y. Ling, Y. Feng, R. Krishna, D.-L. Chen and Y. He, *J. Mater. Chem. A*, 2015, **3**, 19417–19426.

144 R.-B. Lin, D. Chen, Y.-Y. Lin, J.-P. Zhang and X.-M. Chen, *Inorg. Chem.*, 2012, **51**, 9950–9955.

145 T. Panda, P. Pachfule, Y. Chen, J. Jiang and R. Banerjee, *Chem. Commun.*, 2011, **47**, 2011–2013.

146 R. Vaidhyanathan, S. S. Iremonger, K. W. Dawson and G. K. H. Shimizu, *Chem. Commun.*, 2009, 5230–5232.

147 J.-R. Li, Y. Tao, Q. Yu, X.-H. Bu, H. Sakamoto and S. Kitagawa, *Chem. – Eur. J.*, 2008, **14**, 2771–2776.

148 Y. Chen, H. Wang, J. Li and J. V. Lockard, *J. Mater. Chem. A*, 2015, **3**, 4945–4953.

149 J. J. Gassensmith, H. Furukawa, R. A. Smaldone, R. S. Forgan, Y. Y. Botros, O. M. Yaghi and J. F. Stoddart, *J. Am. Chem. Soc.*, 2011, **133**, 15312–15315.

150 G. Zhang, G. Wei, Z. Liu, S. R. J. Oliver and H. Fei, *Chem. Mater.*, 2016, **28**, 6276–6281.

151 F. Debatin, A. Thomas, A. Kelling, N. Hedin, Z. Bacsik, I. Senkovska, S. Kaskel, M. Junginger, H. Müller, U. Schilde, C. Jäger, A. Friedrich and H.-J. Holdt, *Angew. Chem., Int. Ed.*, 2010, **49**, 1258–1262.

152 N. Mosca, R. Vismara, J. A. Fernandes, G. Tuci, C. Di Nicola, K. V. Domasevitch, C. Giacobbe, G. Giambastiani, C. Pettinari, M. Aragones-Anglada, P. Z. Moghadam, D. Fairen-Jimenez, A. Rossin and S. Galli, *Chem. – Eur. J.*, 2018, **24**, 13170–13180.

153 R. A. Smaldone, R. S. Forgan, H. Furukawa, J. J. Gassensmith, A. M. Z. Slawin, O. M. Yaghi and J. F. Stoddart, *Angew. Chem., Int. Ed.*, 2010, **49**, 8630–8634.

154 R. Banerjee, H. Furukawa, D. Britt, C. Knobler, M. O'Keeffe and O. M. Yaghi, *J. Am. Chem. Soc.*, 2009, **131**, 3875–3876.

155 Z.-R. Jiang, H. Wang, Y. Hu, J. Lu and H.-L. Jiang, *ChemSusChem*, 2015, **8**, 878–885.

156 Y. Zhao, H. Wu, T. J. Emge, Q. Gong, N. Nijem, Y. J. Chabal, L. Kong, D. C. Langreth, H. Liu, H. Zeng and J. Li, *Chem. – Eur. J.*, 2011, **17**, 5101–5109.

157 H. Amrouche, S. Aguado, J. Perez-Pellitero, C. Chizallet, F. Siperstein, D. Farrusseng, N. Bats and C. Nieto-Draghi, *J. Phys. Chem. C*, 2011, **115**, 16425–16432.

158 Q. Yang, S. Vaesen, F. Ragon, A. D. Wiersum, D. Wu, A. Lago, T. Devic, C. Martineau, F. Taulelle, P. L. Llewellyn, H. Jobic, C. Zhong, C. Serre, G. D. Weireld and G. Maurin, *Angew. Chem., Int. Ed.*, 2013, **52**, 10316–10320.

159 C.-X. Chen, S.-P. Zheng, Z.-W. Wei, C.-C. Cao, H.-P. Wang, D. Wang, J.-J. Jiang, D. Fenske and C.-Y. Su, *Chem. – Eur. J.*, 2017, **23**, 4060–4064.

160 C. Song, Y. He, B. Li, Y. Ling, H. Wang, Y. Feng, R. Krishna and B. Chen, *Chem. Commun.*, 2014, **50**, 12105–12108.

161 H.-L. Jiang, D. Feng, T.-F. Liu, J.-R. Li and H.-C. Zhou, *J. Am. Chem. Soc.*, 2012, **134**, 14690–14693.

162 M. Eddaoudi, J. Kim, N. Rosi, D. Vodak, J. Wachter, M. O'Keeffe and O. M. Yaghi, *Science*, 2002, **295**, 469–472.

163 H. Deng, S. Grunder, K. E. Cordova, C. Valente, H. Furukawa, M. Hmadeh, F. Gándara, A. C. Whalley, Z. Liu, S. Asahina, H. Kazumori, M. O'Keeffe, O. Terasaki, J. F. Stoddart and O. M. Yaghi, *Science*, 2012, **336**, 1018–1023.

164 S. Nandi, P. D. Luna, T. D. Daff, J. Rother, M. Liu, W. Buchanan, A. I. Hawari, T. K. Woo and R. Vaidhyanathan, *Sci. Adv.*, 2015, **1**, e1500421.

165 S. Xiang, Y. He, Z. Zhang, H. Wu, W. Zhou, R. Krishna and B. Chen, *Nat. Commun.*, 2012, **3**, 954.

166 H.-L. Jiang, T. A. Makal and H.-C. Zhou, *Coord. Chem. Rev.*, 2013, **257**, 2232–2249.

167 S. S. Han, D.-H. Jung and J. Heo, *J. Phys. Chem. C*, 2013, **117**, 71–77.

168 B. Chen, S. Ma, F. Zapata, F. R. Fronczek, E. B. Lobkovsky and H. C. Zhou, *Inorg. Chem.*, 2007, **46**, 1233–1236.

169 T. K. Prasad and M. P. Suh, *Chem. – Eur. J.*, 2012, **18**, 8673–8680.

170 Q. Yao, J. Su, O. Cheung, Q. Liu, N. Hedin and X. Zou, *J. Mater. Chem.*, 2012, **22**, 10345–10351.

171 S. Yang, X. Lin, W. Lewis, M. Suyetin, E. Bichoutskaia, J. E. Parker, C. C. Tang, D. R. Allan, P. J. Rizkallah, P. Hubberstey, N. R. Champness, K. M. Thomas, A. J. Blake and M. Schröder, *Nat. Mater.*, 2012, **11**, 710–716.

172 Y. Ling, M. Deng, Z. Chen, B. Xia, X. Liu, Y. Yang, Y. Zhou and L. Weng, *Chem. Commun.*, 2013, **49**, 78–80.

173 S. Chen, J. Zhang, T. Wu, P. Feng and X. Bu, *J. Am. Chem. Soc.*, 2009, **131**, 16027–16029.

174 S.-T. Zheng, J. T. Bu, Y. Li, T. Wu, F. Zuo, P. Feng and X. Bu, *J. Am. Chem. Soc.*, 2010, **132**, 17062–17064.

175 X. Zhao, X. Bu, Q.-G. Zhai, H. Tran and P. Feng, *J. Am. Chem. Soc.*, 2015, **137**, 1396–1399.

176 S. Horike, S. Shimomura and S. Kitagawa, *Nat. Chem.*, 2009, **1**, 695–704.

2822 | *Chem. Soc. Rev.*, 2019, **48**, 2783–2828

This journal is © The Royal Society of Chemistry 2019

177 F. Salles, H. Jobic, A. Ghoufi, P. L. Llewellyn, C. Serre, S. Bourrelly, G. Férey and G. Maurin, *Angew. Chem., Int. Ed.*, 2009, **48**, 8335–8339.

178 P. K. Thallapally, J. Tian, M. R. Kishan, C. A. Fernandez, S. J. Dalgarno, P. B. McGrail, J. E. Warren and J. L. Atwood, *J. Am. Chem. Soc.*, 2008, **130**, 16842–16843.

179 S. Henke, A. Schneemann, A. Wütscher and R. A. Fischer, *J. Am. Chem. Soc.*, 2012, **134**, 9464–9474.

180 E. J. Carrington, C. A. McAnally, A. J. Fletcher, S. P. Thompson, M. Warren and L. Brammer, *Nat. Chem.*, 2017, **9**, 882–889.

181 S. Hiraide, H. Tanaka, N. Ishikawa and M. T. Miyahara, *ACS Appl. Mater. Interfaces*, 2017, **9**, 41066–41077.

182 J. Park, D. Yuan, K. T. Pham, J.-R. Li, A. Yakovenko and H.-C. Zhou, *J. Am. Chem. Soc.*, 2012, **134**, 99–102.

183 R. Lyndon, K. Konstas, B. P. Ladewig, P. D. Southon, C. J. Kepert and M. R. Hill, *Angew. Chem., Int. Ed.*, 2013, **52**, 3695–3698.

184 N. Nijem, P. Thissen, Y. Yao, R. C. Longo, K. Roodenko, H. Wu, Y. Zhao, K. Cho, J. Li, D. C. Langreth and Y. J. Chabal, *J. Am. Chem. Soc.*, 2011, **133**, 12849–12857.

185 S. Henke and R. A. Fischer, *J. Am. Chem. Soc.*, 2011, **133**, 2064–2067.

186 C. Wang, L. Li, J. G. Bell, X. Lv, S. Tang, X. Zhao and K. M. Thomas, *Chem. Mater.*, 2015, **27**, 1502–1516.

187 M. L. Foo, R. Matsuda, Y. Hijikata, R. Krishna, H. Sato, S. Horike, A. Hori, J. Duan, Y. Sato, Y. Kubota, M. Takata and S. Kitagawa, *J. Am. Chem. Soc.*, 2016, **138**, 3022–3030.

188 S. Henke, R. Schmid, J.-D. Grunwaldt and R. A. Fischer, *Chem. – Eur. J.*, 2010, **16**, 14296–14306.

189 H.-S. Choi and M. P. Suh, *Angew. Chem., Int. Ed.*, 2009, **48**, 6865–6869.

190 D. Dybtsev, H. Chun and K. Kim, *Angew. Chem., Int. Ed.*, 2004, **43**, 5033–5036.

191 N. T. T. Nguyen, H. Furukawa, F. Gándara, H. T. Nguyen, K. E. Cordova and O. M. Yaghi, *Angew. Chem., Int. Ed.*, 2014, **53**, 10645–10648.

192 P. Z. Moghadam, J. F. Ivy, R. K. Arvapally, A. M. D. Santos, J. C. Pearson, L. Zhang, E. Tylianakis, P. Ghosh, I. W. H. Oswald, U. Kaipa, X. Wang, A. K. Wilson, R. Q. Snurr and M. A. Omary, *Chem. Sci.*, 2017, **8**, 3989–4000.

193 S. Nandi, S. Haldar, D. Chakraborty and R. Vaidhyanathan, *J. Mater. Chem. A*, 2017, **5**, 535–543.

194 S. M. Cohen, *Chem. Rev.*, 2012, **112**, 970–1000.

195 Y. Hu, W. M. Verdegaal, S.-H. Yu and H.-L. Jiang, *Chem-SusChem*, 2014, **7**, 734–737.

196 T. M. McDonald, J. A. Mason, X. Kong, E. D. Bloch, D. Gygi, A. Dani, V. Crocellà, F. Giordanino, S. O. Odoh, W. S. Drisdell, B. Vlaisavljevich, A. L. Dzubak, R. Poloni, S. K. Schnell, N. Planas, K. Lee, T. Pascal, L. F. Wan, D. Prendergast, J. B. Neaton, B. Smit, J. B. Kortright, L. Gagliardi, S. Bordiga, J. A. Reimer and J. R. Long, *Nature*, 2015, **519**, 303–308.

197 R. L. Siegelman, T. M. McDonald, M. I. Gonzalez, J. D. Martell, P. J. Milner, J. A. Mason, A. H. Berger, A. S. Bhown and J. R. Long, *J. Am. Chem. Soc.*, 2017, **139**, 10526–10538.

198 P. J. Milner, J. D. Martell, R. L. Siegelman, D. Gygi, S. C. Weston and J. R. Long, *Chem. Sci.*, 2018, **9**, 160–174.

199 P.-Q. Liao, X.-W. Chen, S.-Y. Liu, X.-Y. Li, Y.-T. Xu, M. Tang, Z. Rui, H. Ji, J.-P. Zhang and X.-M. Chen, *Chem. Sci.*, 2016, **7**, 6528–6533.

200 D. Andirova, Y. Lei, X. Zhao and S. Choi, *ChemSusChem*, 2015, **8**, 3405–3409.

201 J. S. Yeon, W. R. Lee, N. W. Kim, H. Jo, H. Lee, J. H. Song, K. S. Lim, D. W. Kang, J. G. Seo, D. Moon, B. Wiers and C. S. Hong, *J. Mater. Chem. A*, 2015, **3**, 19177–19185.

202 W. R. Lee, H. Jo, L.-M. Yang, H. Lee, D. W. Ryu, K. S. Lim, J. H. Song, D. Y. Min, S. S. Han, J. G. Seo, Y. K. Park, D. Moone and C. S. Hong, *Chem. Sci.*, 2015, **6**, 3697–3705.

203 D. Wu, T. M. McDonald, Z. Quan, S. V. Ushakov, P. Zhang, J. R. Long and A. Navrotsky, *J. Mater. Chem. A*, 2015, **3**, 4248–4254.

204 N. Planas, A. L. Dzubak, R. Poloni, L.-C. Lin, A. McManus, T. M. McDonald, J. B. Neaton, J. R. Long, B. Smit and L. Gagliardi, *J. Am. Chem. Soc.*, 2013, **135**(20), 7402–7405.

205 P. Deria, J. E. Mondloch, E. Tylianakis, P. Ghosh, W. Bury, R. Q. Snurr, J. T. Hupp and O. K. Farha, *J. Am. Chem. Soc.*, 2013, **135**, 16801–16804.

206 C. H. Lau, R. Babarao and M. R. Hill, *Chem. Commun.*, 2013, **49**, 3634–3636.

207 Z. Zhang, W.-Y. Gao, L. Wojtas, S. Ma, M. Eddaoudi and M. J. Zaworotko, *Angew. Chem., Int. Ed.*, 2012, **51**, 9330–9334.

208 H. Li, K. Wang, D. Feng, Y.-P. Chen, W. Verdegaal and H.-C. Zhou, *ChemSusChem*, 2016, **9**, 2832–2840.

209 A. Kronast, S. Eckstein, P. T. Altenbuchner, K. Hindelang, S. I. Vagin and B. Rieger, *Chem. – Eur. J.*, 2016, **22**, 12800–12807.

210 Z. Hu, K. Zhang, M. Zhang, Z. Guo, J. Jiang and D. Zhao, *ChemSusChem*, 2014, **7**, 2791–2795.

211 H. J. Park, Y. E. Cheon and M. P. Suh, *Chem. – Eur. J.*, 2010, **16**, 11662–11669.

212 C.-X. Chen, Z. Wei, J.-J. Jiang, Y.-Z. Fan, S.-P. Zheng, C.-C. Cao, Y.-H. Li, D. Fenske and C.-Y. Su, *Angew. Chem., Int. Ed.*, 2016, **55**, 9932–9936.

213 D. H. Hong and M. P. Suh, *Chem. – Eur. J.*, 2014, **20**, 426–434.

214 Z. Hu, S. Faucher, Y. Zhuo, Y. Sun, S. Wang and D. Zhao, *Chem. – Eur. J.*, 2015, **21**, 17246–17255.

215 J. Sánchez-Laínez, A. Veiga, B. Zornoza1, S. R. G. Balestra, S. Hamad, A. R. Ruiz-Salvador, S. Calero, C. Téllez and J. Coronas, *J. Mater. Chem. A*, 2017, **5**, 25601–25608.

216 J. An and N. L. Rosi, *J. Am. Chem. Soc.*, 2010, **132**, 5578–5579.

217 T. Li and N. L. Rosi, *Chem. Commun.*, 2013, **49**, 11385–11387.

218 B. Liu, R. Zhang, C.-Y. Pan and H.-L. Jiang, *Inorg. Chem.*, 2017, **56**, 4263–4266.

219 H. J. Park and M. P. Suh, *Chem. Sci.*, 2013, **4**, 685–690.

220 F. P. Kinik, C. Altintas, V. Balci, B. Koyuturk, A. Uzun and S. Keskin, *ACS Appl. Mater. Interfaces*, 2016, **8**, 30992–31005.

221 I. Cota and F. F. Martinez, *Coord. Chem. Rev.*, 2017, **351**, 189–204.

222 K. B. Sezginel, S. Keskin and A. Uzun, *Langmuir*, 2016, **32**, 1139–1147.

This journal is © The Royal Society of Chemistry 2019

Chem. Soc. Rev., 2019, **48**, 2783–2828 | 2823

223 Y. Lin, Q. Yan, C. Kong and L. Chen, *Sci. Rep.*, 2013, **3**, 1859.

224 Y. Lin, H. Lin, H. Wang, Y. Suo, B. Li, C. Kong and L. Chen, *J. Mater. Chem. A*, 2014, **2**, 14658–14665.

225 N. Ding, H. Li, X. Feng, Q. Wang, S. Wang, L. Ma, J. Zhou and B. Wang, *J. Am. Chem. Soc.*, 2016, **138**, 10100–10103.

226 L. A. Darunte, A. D. Oetomo, K. S. Walton, D. S. Sholl and C. W. Jones, *ACS Sustainable Chem. Eng.*, 2016, **4**, 5761–5768.

227 R. Kumar, D. Raut, U. Ramamurty and C. N. R. Rao, *Angew. Chem., Int. Ed.*, 2016, **55**, 7857–7861.

228 S. Liu, L. Sun, F. Xu, J. Zhang, C. Jiao, F. Li, Z. Li, S. Wang, Z. Wang, X. Jiang, H. Zhou, L. Yang and C. Schick, *Energy Environ. Sci.*, 2013, **6**, 818–823.

229 A. Chakraborty, A. Achari, M. Eswaramoorthy and T. K. Maji, *Chem. Commun.*, 2016, **52**, 11378–11381.

230 Y. Zhao, M. Seredych, Q. Zhong and T. J. Bandosz, *ACS Appl. Mater. Interfaces*, 2013, **5**, 4951–4959.

231 A. Policicchio, Y. Zhao, Q. Zhong, R. G. Agostino and T. J. Bandosz, *ACS Appl. Mater. Interfaces*, 2014, **6**, 101–108.

232 Z. Bian, X. Zhu, T. Jin, J. Gao, J. Hu and H. Liu, *Microporous Mesoporous Mater.*, 2014, **200**, 159–164.

233 S. Pourebrahimi, M. Kazemeini, E. G. Babakhani and A. Taheri, *Microporous Mesoporous Mater.*, 2015, **218**, 144–152.

234 A. Chakraborty, S. Roy, M. Eswaramoorthy and T. K. Maji, *J. Mater. Chem. A*, 2017, **5**, 8423–8430.

235 D. Qian, C. Lei, G.-P. Hao, W.-C. Li and A.-H. Lu, *ACS Appl. Mater. Interfaces*, 2012, **4**, 6125–6132.

236 N. E. Tari, A. Tadjarodi, J. Tamnanloo and S. Fatemi, *Microporous Mesoporous Mater.*, 2016, **231**, 154–162.

237 F. Gao, Y. Li, Z. Bian, J. Hu and H. Liu, *J. Mater. Chem. A*, 2015, **3**, 8091–8097.

238 K. M. Gupta, Y. Chen and J. Jiang, *J. Phys. Chem. C*, 2013, **117**, 5792–5799.

239 J. M. Vicent-Luna, J. J. Gutiérrez-Sevillano, J. A. Anta and S. Calero, *J. Phys. Chem. C*, 2013, **117**, 20762–20768.

240 Z. Xiang, Z. Hu, D. Cao, W. Yang, J. Lu, B. Han and W. Wang, *Angew. Chem., Int. Ed.*, 2011, **50**, 491–494.

241 Y. Yang, L. Ge, V. Rudolph and Z. Zhu, *Dalton Trans.*, 2014, **43**, 7028–7036.

242 H. Furukawa, F. Gándara, Y.-B. Zhang, J. Jiang, W. L. Queen, M. R. Hudson and O. M. Yaghi, *J. Am. Chem. Soc.*, 2014, **136**, 4369–4381.

243 S. Yuan, L. Feng, K. Wang, J. Pang, M. Bosch, C. Lollar, Y. Sun, J. Qin, X. Yang, P. Zhang, Q. Wang, L. Zou, Y. Zhang, L. Zhang, Y. Fang, J. Li and H.-C. Zhou, *Adv. Mater.*, 2018, 1704303.

244 W. Zhang, Y. Hu, J. Ge, H.-L. Jiang and S.-H. Yu, *J. Am. Chem. Soc.*, 2014, **136**, 16978–16981.

245 J. G. Nguyen and S. M. Cohen, *J. Am. Chem. Soc.*, 2010, **132**, 4560–4561.

246 S. J. Yang and C. R. Park, *Adv. Mater.*, 2012, **24**, 4010–4013.

247 C. M. Miralda, E. E. Macias, M. Zhu, P. Ratnasamy and M. A. Carreon, *ACS Catal.*, 2012, **2**, 180–183.

248 D.-A. Yang, H.-Y. Cho, J. Kim, S.-T. Yang and W.-S. Ahn, *Energy Environ. Sci.*, 2012, **5**, 6465–6473.

249 X. Zhou, Y. Zhang, X. Yang, L. Zhao and G. Wang, *J. Mol. Catal. A: Chem.*, 2012, **361–362**, 12–16.

250 X. Huang, Y. Chen, Z. Lin, X. Ren, Y. Song, Z. Xu, X. Dong, X. Li, C. Hu and B. Wang, *Chem. Commun.*, 2014, **50**, 2624–2627.

251 D. Ma, B. Li, K. Liu, X. Zhang, W. Zou, Y. Yang, G. Li, Z. Shi and S. Feng, *J. Mater. Chem. A*, 2015, **3**, 23136–23142.

252 R. R. Kuruppathparambil, T. Jose, R. Babu, G.-Y. Hwang, A. C. Kathalikkattil, D.-W. Kim and D.-W. Park, *Appl. Catal., B*, 2016, **182**, 562–569.

253 J. Tharun, K.-M. Bhin, R. Roshan, D. W. Kim, A. C. Kathalikkattil, R. Babu, H. Y. Ahn, Y. S. Won and D.-W. Park, *Green Chem.*, 2016, **18**, 2479–2487.

254 J. Liang, R.-P. Chen, X.-Y. Wang, T.-T. Liu, X.-S. Wang, Y.-B. Huang and R. Cao, *Chem. Sci.*, 2017, **8**, 1570–1575.

255 J. Liang, Y.-Q. Xie, X.-S. Wang, Q. Wang, T.-T. Liu, Y.-B. Huang and R. Cao, *Chem. Commun.*, 2018, **54**, 342–345.

256 R. Zou, P.-Z. Li, Y.-F. Zeng, J. Liu, R. Zhao, H. Duan, Z. Luo, J.-G. Wang, R. Zou and Y. Zhao, *Small*, 2016, **12**, 2334–2343.

257 M. H. Beyzavi, R. C. Klet, S. Tussupbayev, J. Borycz, N. A. Vermeulen, C. J. Cramer, J. F. Stoddart, J. T. Hupp and O. K. Farha, *J. Am. Chem. Soc.*, 2014, **136**, 15861–15864.

258 W.-Y. Gao, Y. Chen, Y. Niu, K. Williams, L. Cash, P. J. Perez, L. Wojtas, J. Cai, Y.-S. Chen and S. Ma, *Angew. Chem., Int. Ed.*, 2014, **53**, 2615–2619.

259 D. Feng, W.-C. Chung, Z. Wei, Z.-Y. Gu, H.-L. Jiang, Y.-P. Chen, D. J. Darensbourg and H.-C. Zhou, *J. Am. Chem. Soc.*, 2013, **135**, 17105–17110.

260 W.-Y. Gao, L. Wojtas and S. Ma, *Chem. Commun.*, 2014, **50**, 5316–5318.

261 L. Zhang, S. Yuan, L. Feng, B. Guo, J.-S. Qin, B. Xu, C. Lollar, D. Sun and H.-C. Zhou, *Angew. Chem., Int. Ed.*, 2018, **57**, 5095–5099.

262 B.-B. Lu, W. Jiang, J. Yang, Y.-Y. Liu and J.-F. Ma, *ACS Appl. Mater. Interfaces*, 2017, **9**, 39441–39449.

263 H.-F. Zhou, B. Liu, L. Hou, W.-Y. Zhang and Y.-Y. Wang, *Chem. Commun.*, 2018, **54**, 456–459.

264 A. C. Kathalikkattil, D.-W. Kim, J. Tharun, H.-G. Soek, R. Roshan and D.-W. Park, *Green Chem.*, 2014, **16**, 1607–1616.

265 L. Liu, S.-M. Wang, Z.-B. Han, M. Ding, D.-Q. Yuan and H.-L. Jiang, *Inorg. Chem.*, 2016, **55**, 3558–3565.

266 N. Wei, Y. Zhang, L. Liu, Z.-B. Han and D.-Q. Yuan, *Appl. Catal., B*, 2017, **219**, 603–610.

267 H.-H. Wang, L. Hou, Y.-Z. Li, C.-Y. Jiang, Y.-Y. Wang and Z. Zhu, *ACS Appl. Mater. Interfaces*, 2017, **9**, 17969–17976.

268 C.-Y. Gao, J. Ai, H.-R. Tian, D. Wu and Z.-M. Sun, *Chem. Commun.*, 2017, **53**, 1293–1296.

269 J. Zhu, P. M. Usov, W. Xu, P. J. Celis-Salazar, S. Lin, M. C. Kessinger, C. Landaverde-Alvarado, M. Cai, A. M. May, C. Slebodnick, D. Zhu, S. D. Senanayake and A. J. Morris, *J. Am. Chem. Soc.*, 2018, **140**, 993–1003.

270 H. He, Q. Sun, W. Gao, J. A. Perman, F. Sun, G. Zhu, B. Aguila, K. Forrest, B. Space and S. Ma, *Angew. Chem., Int. Ed.*, 2018, **57**, 4657–4662.

271 Z. Zhou, C. He, J. Xiu, L. Yang and C. Duan, *J. Am. Chem. Soc.*, 2015, **137**, 15066–15069.

272 A. C. Kathalikkattil, R. Roshan, J. Tharun, R. Babu, G.-S. Jeong, D.-W. Kim, S. J. Choc and D.-W. Park, *Chem. Commun.*, 2016, **52**, 280–283.

2824 | *Chem. Soc. Rev.*, 2019, **48**, 2783–2828

This journal is © The Royal Society of Chemistry 2019

273 J. Song, Z. Zhang, S. Hu, T. Wu, T. Jiang and B. Han, *Green Chem.*, 2009, **11**, 1031–1036.

274 V. Guillerm, Ł. J. Weseliński, Y. Belmabkhout, A. J. Cairns, V. D'Elia, Ł. Wojtas, K. Adil and M. Eddaoudi, *Nat. Chem.*, 2014, **6**, 673–680.

275 F. Liu, Y. Xu, L. Zhao, L. Zhang, W. Guo, R. Wang and D. Sun, *J. Mater. Chem. A*, 2015, **3**, 21545–21552.

276 A. C. Kathalikkattil, R. Babu, R. K. Roshan, H. Lee, H. Kim, J. Tharun, E. Suresh and D.-W. Park, *J. Mater. Chem. A*, 2015, **3**, 22636–22647.

277 R. Babu, R. Roshan, A. C. Kathalikkattil, D. W. Kim and D.-W. Park, *ACS Appl. Mater. Interfaces*, 2016, **8**, 33723–33731.

278 W. Jiang, J. Yang, Y.-Y. Liu, S.-Y. Song and J.-F. Ma, *Chem. – Eur. J.*, 2016, **22**, 16991–16997.

279 R. Babu, A. C. Kathalikkattil, R. Roshan, J. Tharun, D.-W. Kim and D.-W. Park, *Green Chem.*, 2016, **18**, 232–242.

280 Y.-H. Han, Z.-Y. Zhou, C.-B. Tian and S.-W. Du, *Green Chem.*, 2016, **18**, 4086–4091.

281 P.-Z. Li, X.-J. Wang, J. Liu, J. S. Lim, R. Zou and Y. Zhao, *J. Am. Chem. Soc.*, 2016, **138**, 2142–2145.

282 X.-Y. Li, Y.-Z. Li, Y. Yang, L. Hou, Y.-Y. Wang and Z. Zhu, *Chem. Commun.*, 2017, **53**, 12970–12973.

283 B.-J. Yao, L.-G. Ding, F. Li, J.-T. Li, Q.-J. Fu, Y. Ban, A. Guo and Y.-B. Dong, *ACS Appl. Mater. Interfaces*, 2017, **9**, 38919–38930.

284 N. Wei, R.-X. Zuo, Y.-Y. Zhang, Z.-B. Han and X.-J. Gu, *Chem. Commun.*, 2017, **53**, 3224–3227.

285 X.-Y. Li, L.-N. Ma, Y. Liu, L. Hou, Y.-Y. Wang and Z. Zhu, *ACS Appl. Mater. Interfaces*, 2018, **10**, 10965–10973.

286 J. Liu, Y.-Z. Fan, X. Li, Y.-W. Xu, L. Zhang and C.-Y. Su, *ChemSusChem*, 2018, **11**, 2340–2347.

287 V. Sharma, D. De, R. Saha, R. Das, P. K. Chattaraj and P. K. Bharadwaj, *Chem. Commun.*, 2017, **53**, 13371–13374.

288 X. Guo, Z. Zhou, C. Chen, J. Bai, C. He and C. Duan, *ACS Appl. Mater. Interfaces*, 2016, **8**, 31746–31756.

289 L. Tang, S. Zhang, Q. Wu, X. Wang, H. Wu and Z. Jiang, *J. Mater. Chem. A*, 2018, **6**, 2964–2973.

290 P.-Z. Li, X.-J. Wang, J. Liu, H. S. Phang, Y. Li and Y. Zhao, *Chem. Mater.*, 2017, **29**, 9256–9261.

291 P. T. K. Nguyen, H. T. D. Nguyen, H. N. Nguyen, C. A. Trickett, Q. T. Ton, E. Gutiérrez-Puebla, M. A. Monge, K. E. Cordova and F. Gándara, *ACS Appl. Mater. Interfaces*, 2018, **10**, 733–744.

292 O. V. Zalomaeva, N. V. Maksimchuk, A. M. Chibiryaev, K. A. Kovalenko, V. P. Fedin and B. S. Balzhinimaev, *J. Energy Chem.*, 2013, **22**, 130–135.

293 Q. Han, B. Qi, W. Ren, C. He, J. Niu and C. Duan, *Nat. Commun.*, 2015, **6**, 10007.

294 X. Wang, W.-Y. Gao, Z. Niu, L. Wojtas, J. A. Perman, Y.-S. Chen, Z. Li, B. Aguila and S. Ma, *Chem. Commun.*, 2018, **54**, 1170–1173.

295 H. Xu, X.-F. Liu, C.-S. Cao, B. Zhao, P. Cheng and L.-N. He, *Adv. Sci.*, 2016, **3**, 1600048.

296 N. Sharma, S. S. Dhankhar, S. Kumar, T. J. D. Kumar and C. M. Nagaraja, *Chem. – Eur. J.*, 2018, **24**, 16662–16669.

297 G. Xiong, B. Yu, J. Dong, Y. Shi, B. Zhao and L.-N. He, *Chem. Commun.*, 2017, **53**, 6013–6016.

298 Z. Zhou, C. He, L. Yang, Y. Wang, T. Liu and C. Duan, *ACS Catal.*, 2017, **7**, 2248–2256.

299 G. Zhang, H. Yang and H. Fei, *ACS Catal.*, 2018, **8**, 2519–2525.

300 S.-L. Hou, J. Dong, X.-L. Jiang, Z.-H. Jiao and B. Zhao, *Angew. Chem., Int. Ed.*, 2019, **58**, 577–581.

301 B. Schäffner, F. Schäffner, S. P. Verevkin and A. Börner, *Chem. Rev.*, 2010, **110**, 4554–4581.

302 A. A. Shaikh and S. Sivaram, *Chem. Rev.*, 1996, **96**, 951–976.

303 D.-Y. Yu and Y.-G. Zhang, *Proc. Natl. Acad. Sci. U. S. A.*, 2010, **107**, 20184–20189.

304 F. Manjolinho, M. Arndt, K. Gooßen and L. J. Gooßen, *ACS Catal.*, 2012, **2**, 2014–2021.

305 C. Qiao, Y. Cao and L.-N. He, *Mini-Rev. Org. Chem.*, 2018, **15**, 283–290.

306 X.-H. Liu, J.-G. Ma, Z. Niu, G.-M. Yang and P. Cheng, *Angew. Chem., Int. Ed.*, 2015, **54**, 988–991.

307 N.-N. Zhu, X.-H. Liu, T. Li, J.-G. Ma, P. Cheng and G.-M. Yang, *Inorg. Chem.*, 2017, **56**, 3414–3420.

308 R. A. Molla, K. Ghosh, B. Banerjee, M. A. Iqubal, S. K. Kundu, S. M. Islam and A. Bhaumik, *J. Colloid Interface Sci.*, 2016, **477**, 220–229.

309 M. Trivedi, Bhaskaran, A. Kumar, G. Singh, A. Kumar and N. P. Rath, *New J. Chem.*, 2016, **40**, 3109–3118.

310 L. Sun, Y. Yun, H. Sheng, Y. Du, Y. Ding, P. Wu, P. Li and M. Zhu, *J. Mater. Chem. A*, 2018, **6**, 15371–15376.

311 D. Chen, R. Luo, M. Li, M. Wen, Y. Li, C. Chen and N. Zhang, *Chem. Commun.*, 2017, **53**, 10930–10933.

312 C. Liu, X.-H. Liu, B. Li, L. Zhang, J.-G. Ma and P. Cheng, *J. Energy Chem.*, 2017, **26**, 821–824.

313 M. Ding and H.-L. Jiang, *ACS Catal.*, 2018, **8**, 3194–3201.

314 B. Aguila, Q. Sun, X. Wang, E. O. Rourke, A. M. A. Enizi, A. Nafady and S. Ma, *Angew. Chem., Int. Ed.*, 2018, **57**, 10107–10111.

315 D. Kim, D. W. Kim, O. Buyukcakir, M.-K. Kim, K. Polychronopoulou and A. Coskun, *Adv. Funct. Mater.*, 2017, **27**, 1700706.

316 Q. Yang, C.-C. Yang, C.-H. Lin and H.-L. Jiang, *Angew. Chem., Int. Ed.*, 2019, **58**, 3511–3515.

317 T. Toyao, M. Fujiwaki, K. Miyahara, T.-H. Kim, Y. Horiuchi and M. Matsuoka, *ChemSusChem*, 2015, **8**, 3905–3912.

318 M. Ding, S. Chen, X.-Q. Liu, L.-B. Sun, J. Lu and H.-L. Jiang, *ChemSusChem*, 2017, **10**, 1898–1903.

319 J. Zhu, J. Liu, Y. Machain, B. Bonnett, S. Lin, M. Cai, M. C. Kessinger, P. M. Usov, W. Xu, S. D. Senanayake, D. Troya, A. R. Esker and A. J. Morris, *J. Mater. Chem. A*, 2018, **6**, 22195–22203.

320 W. Meng, Y. Zeng, Z. Liang, W. Guo, C. Zhi, Y. Wu, R. Zhong, C. Qu and R. Zou, *ChemSusChem*, 2018, **11**, 3751–3757.

321 J. Li, Y. Ren, C. Yue, Y. Fan, C. Qi and H. Jiang, *ACS Appl. Mater. Interfaces*, 2018, **10**, 36047–36057.

322 D. Zhao, X.-H. Liu, J.-H. Guo, H.-J. Xu, Y. Zhao, Y. Lu and W.-Y. Sun, *Inorg. Chem.*, 2018, **57**, 2695–2704.

323 D. Zhao, X.-H. Liu, C. Zhu, Y.-S. Kang, P. Wang, Z. Shi, Y. Lu and W.-Y. Sun, *ChemCatChem*, 2017, **9**, 4598–4606.

324 W. Wang, S. Wang, X. Ma and J. Gong, *Chem. Soc. Rev.*, 2011, **40**, 3703–3727.

This journal is © The Royal Society of Chemistry 2019

Chem. Soc. Rev., 2019, **48**, 2783–2828 | 2825

325 P. G. Jessop, F. Joó and C.-C. Tai, *Coord. Chem. Rev.*, 2004, **248**, 2425–2442.

326 A. Goeppert, M. Czaun, J.-P. Jones, G. K. S. Prakash and G. A. Olah, *Chem. Soc. Rev.*, 2014, **43**, 7995–8048.

327 J. Ye and J. K. Johnson, *ACS Catal.*, 2015, **5**, 2921–2928.

328 J. Ye and J. K. Johnson, *ACS Catal.*, 2015, **5**, 6219–6229.

329 J. Ye and J. K. Johnson, *Catal. Sci. Technol.*, 2016, **6**, 8392–8405.

330 B. An, L. Zeng, M. Jia, Z. Li, Z. Lin, Y. Song, Y. Zhou, J. Cheng, C. Wang and W. Lin, *J. Am. Chem. Soc.*, 2017, **139**, 17747–17750.

331 B. Rungtaweevoranit, J. Baek, J. R. Araujo, B. S. Archanjo, K. M. Choi, O. M. Yaghi and G. A. Somorjai, *Nano Lett.*, 2016, **16**, 7645–7649.

332 W. Zhen, F. Gao, B. Tian, P. Ding, Y. Deng, Z. Li, H. Gao and G. Lu, *J. Catal.*, 2017, **348**, 200–211.

333 Z.-W. Zhao, X. Zhou, Y.-N. Liu, C.-C. Shen, C.-Z. Yuan, Y.-F. Jiang, S.-J. Zhao, L.-B. Ma, T.-Y. Cheang and A.-W. Xu, *Catal. Sci. Technol.*, 2018, **8**, 3160–3165.

334 W. Zhen, B. Li, G. Lu and J. Ma, *Chem. Commun.*, 2015, **51**, 1728–1731.

335 W. Zhang, L. Wang, K. Wang, M. U. Khan, M. Wang, H. Li and J. Zeng, *Small*, 2017, **13**, 1602583.

336 X. Zhao, H. Xu, X. Wang, Z. Zheng, Z. Xu and J. Ge, *ACS Appl. Mater. Interfaces*, 2018, **10**, 15096–15103.

337 S. Hu, M. Liu, F. Ding, C. Song, G. Zhang and X. Guo, *J. CO2 Util.*, 2016, **15**, 89–95.

338 B. An, J. Zhang, K. Cheng, P. Ji, C. Wang and W. Lin, *J. Am. Chem. Soc.*, 2017, **139**, 3834–3840.

339 M. Mon, M. A. Rivero-Crespo, J. Ferrando-Soria, A. Vidal-Moya, M. Boronat, A. Leyva-Pérez, A. Corma, J. C. Hernández-Garrido, M. López-Haro, J. J. Calvino, G. Ragazzon, A. Credi, D. Armentano and E. Pardo, *Angew. Chem., Int. Ed.*, 2018, **57**, 6186–6191.

340 Z. Li, T. M. Rayder, L. Luo, J. A. Byers and C.-K. Tsung, *J. Am. Chem. Soc.*, 2018, **140**, 8082–8085.

341 R. Lippi, S. C. Howard, H. Barron, C. D. Easton, I. C. Madsen, L. J. Waddington, C. Vogt, M. R. Hill, C. J. Sumby, C. J. Doonan and D. F. Kennedy, *J. Mater. Chem. A*, 2017, **5**, 12990–12997.

342 Y. Yin, B. Hu, X. Li, X. Zhou, X. Hong and G. Liu, *Appl. Catal., B*, 2018, **234**, 143–152.

343 J. Zhang, B. An, Y. Hong, Y. Meng, X. Hu, C. Wang, J. Lin, W. Lin and Y. Wang, *Mater. Chem. Front.*, 2017, **1**, 2405–2409.

344 H. Zhang, T. Wang, J. Wang, H. Liu, T. D. Dao, M. Li, G. Liu, X. Meng, K. Chang, L. Shi, T. Nagao and J. Ye, *Adv. Mater.*, 2016, **28**, 3703–3710.

345 W. Li, A. Zhang, X. Jiang, C. Chen, Z. Liu, C. Song and X. Guo, *ACS Sustainable Chem. Eng.*, 2017, **5**, 7824–7831.

346 A. Ramirez, L. Gevers, A. Bavykina, S. Ould-Chikh and J. Gascon, *ACS Catal.*, 2018, **8**, 9174–9182.

347 G. Zhan and H. C. Zeng, *ACS Catal.*, 2017, **7**, 7509–7519.

348 Y. Li, X. Cai, S. Chen, H. Zhang, K. H. L. Zhang, J. Hong, B. Chen, D.-H. Kuo and W. Wang, *ChemSusChem*, 2018, **11**, 1040–1047.

349 L. Li, S. Zhang, L. Xu, J. Wang, L.-X. Shi, Z.-N. Chen, M. Hong and J. Luo, *Chem. Sci.*, 2014, **5**, 3808–3813.

350 Y. Liu, Y. Yang, Q. Sun, Z. Wang, B. Huang, Y. Dai, X. Qin and X. Zhang, *ACS Appl. Mater. Interfaces*, 2013, **5**, 7654–7658.

351 E.-X. Chen, M. Qiu, Y.-F. Zhang, Y.-S. Zhu, L.-Y. Liu, Y.-Y. Sun, X. Bu, J. Zhang and Q. Lin, *Adv. Mater.*, 2018, **30**, 1704388.

352 Y. Fu, D. Sun, Y. Chen, R. Huang, Z. Ding, X. Fu and Z. Li, *Angew. Chem., Int. Ed.*, 2012, **51**, 3364–3367.

353 H.-Q. Xu, J. Hu, D. Wang, Z. Li, Q. Zhang, Y. Luo, S.-H. Yu and H.-L. Jiang, *J. Am. Chem. Soc.*, 2015, **137**, 13440–13443.

354 Z.-H. Yan, M.-H. Du, J. Liu, S. Jin, C. Wang, G.-L. Zhuang, X.-J. Kong, L.-S. Long and L.-S. Zheng, *Nat. Commun.*, 2018, **9**, 3353.

355 D. Sun, Y. Fu, W. Liu, L. Ye, D. Wang, L. Yang, X. Fu and Z. Li, *Chem. – Eur. J.*, 2013, **19**, 14279–14285.

356 X. Deng, J. Albero, L. Xu, H. García and Z. Li, *Inorg. Chem.*, 2018, **57**, 8276–8286.

357 D. Sun, Y. Gao, J. Fu, X. Zeng, Z. Chen and Z. Li, *Chem. Commun.*, 2015, **51**, 2645–2648.

358 D. Wang, R. Huang, W. Liu, D. Sun and Z. Li, *ACS Catal.*, 2014, **4**, 4254–4260.

359 D. Chen, H. Xing, C. Wang and Z. Su, *J. Mater. Chem. A*, 2016, **4**, 2657–2662.

360 H. Zhang, J. Wei, J. Dong, G. Liu, L. Shi, P. An, G. Zhao, J. Kong, X. Wang, X. Meng, J. Zhang and J. Ye, *Angew. Chem., Int. Ed.*, 2016, **55**, 14310–14314.

361 Y. Lee, S. Kim, H. Fei, J. K. Kang and S. M. Cohen, *Chem. Commun.*, 2015, **51**, 16549–16552.

362 G. Lan, Z. Li, S. S. Veroneau, Y.-Y. Zhu, Z. Xu, C. Wang and W. Lin, *J. Am. Chem. Soc.*, 2018, **140**, 12369–12373.

363 D. Sun, W. Liu, M. Qiu, Y. Zhang and Z. Li, *Chem. Commun.*, 2015, **51**, 2056–2059.

364 Y. Lee, S. Kim, J. K. Kang and S. M. Cohen, *Chem. Commun.*, 2015, **51**, 5735–5738.

365 S. Wang, W. Yao, J. Lin, Z. Ding and X. Wang, *Angew. Chem., Int. Ed.*, 2014, **53**, 1034–1038.

366 H. Fei, M. D. Sampson, Y. Lee, C. P. Kubiak and S. M. Cohen, *Inorg. Chem.*, 2015, **54**, 6821–6828.

367 Y. Wang, N.-Y. Huang, J.-Q. Shen, P.-Q. Liao, X.-M. Chen and J.-P. Zhang, *J. Am. Chem. Soc.*, 2018, **140**, 38–41.

368 J. Zhao, Q. Wang, C. Sun, T. Zheng, L. Yan, M. Li, K. Shao, X. Wang and Z. Su, *J. Mater. Chem. A*, 2017, **5**, 12498–12505.

369 T. Kajiwara, M. Fujii, M. Tsujimoto, K. Kobayashi, M. Higuchi, K. Tanaka and S. Kitagawa, *Angew. Chem., Int. Ed.*, 2016, **55**, 2697–2700.

370 W.-M. Liao, J.-H. Zhang, Z. Wang, S.-Y. Yin, M. Pan, H.-P. Wang and C.-Y. Su, *J. Mater. Chem. A*, 2018, **6**, 11337–11345.

371 M. Wang, J. Liu, C. Guo, X. Gao, C. Gong, Y. Wang, B. Liu, X. Li, G. G. Gurzadyan and L. Sun, *J. Mater. Chem. A*, 2018, **6**, 4768–4775.

372 J. Qin, S. Wang and X. Wang, *Appl. Catal., B*, 2017, **209**, 476–482.

373 M. B. Chambers, X. Wang, N. Elgrishi, C. H. Hendon, A. Walsh, J. Bonnefoy, J. Canivet, E. A. Quadrelli,

2826 | *Chem. Soc. Rev.*, 2019, **48**, 2783–2828

This journal is © The Royal Society of Chemistry 2019

D. Farrusseng, C. Mellot-Draznieks and M. Fontecave, *ChemSusChem*, 2015, **8**, 603–608.

374 B. Han, X. Ou, Z. Deng, Y. Song, C. Tian, H. Deng, Y.-J. Xu and Z. Lin, *Angew. Chem., Int. Ed.*, 2018, **57**, 16811–16815.

375 Q. Liu, Z.-X. Low, L. Li, A. Razmjou, K. Wang, J. Yao and H. Wang, *J. Mater. Chem. A*, 2013, **1**, 11563–11569.

376 R. Li, J. Hu, M. Deng, H. Wang, X. Wang, Y. Hu, H.-L. Jiang, J. Jiang, Q. Zhang, Y. Xie and Y. Xiong, *Adv. Mater.*, 2014, **26**, 4783–4788.

377 L. Shi, T. Wang, H. Zhang, K. Chang and J. Ye, *Adv. Funct. Mater.*, 2015, **25**, 5360–5367.

378 G. Xu, H. Zhang, J. Wei, H.-X. Zhang, X. Wu, Y. Li, C. Li, J. Zhang and J. Ye, *ACS Nano*, 2018, **12**, 5333–5340.

379 C. Chen, T. Wu, H. Wu, H. Liu, Q. Qian, Z. Liu, G. Yang and B. Han, *Chem. Sci.*, 2018, **9**, 8890–8894.

380 Y. Su, Z. Zhang, H. Liu and Y. Wang, *Appl. Catal., B*, 2017, **200**, 448–457.

381 X. Wang, X. Zhao, D. Zhang, G. Li and H. Li, *Appl. Catal., B*, 2018, **228**, 47–53.

382 A. Crake, K. C. Christoforidis, A. Kafizas, S. Zafeiratos and C. Petit, *Appl. Catal., B*, 2017, **210**, 131–140.

383 D. Sun, W. Liu, Y. Fu, Z. Fang, F. Sun, X. Fu, Y. Zhang and Z. Li, *Chem. – Eur. J.*, 2014, **20**, 4780–4788.

384 K. Min Choi, D. Kim, B. Rungtaweevoranit, C. A. Trickett, J. T. D. Barmanbek, A. S. Alshammari, P. Yang and O. M. Yaghi, *J. Am. Chem. Soc.*, 2017, **139**, 356–362.

385 S. Wang, J. Lin and X. Wang, *Phys. Chem. Chem. Phys.*, 2014, **16**, 14656–14660.

386 S. Wang and X. Wang, *Appl. Catal., B*, 2015, **162**, 494–500.

387 S. Yan, S. Ouyang, H. Xu, M. Zhao, X. Zhang and J. Ye, *J. Mater. Chem. A*, 2016, **4**, 15126–15133.

388 Z. Huang, P. Dong, Y. Zhang, X. Nie, X. Wang and X. Zhang, *J. CO$_2$ Util.*, 2018, **24**, 369–375.

389 X. He and W.-N. Wang, *J. Mater. Chem. A*, 2018, **6**, 932–940.

390 M. Wang, D. Wang and Z. Li, *Appl. Catal., B*, 2016, **183**, 47–52.

391 J. W. Maina, J. A. Schütz, L. Grundy, E. D. Ligneris, Z. Yi, L. Kong, C. Pozo-Gonzalo, M. Ionescu and L. F. Dumée, *ACS Appl. Mater. Interfaces*, 2017, **9**, 35010–35017.

392 X. He, Z. Gan, S. Fisenko, D. Wang, H. M. El-Kaderi and W.-N. Wang, *ACS Appl. Mater. Interfaces*, 2017, **9**, 9688–9698.

393 H. Zhao, X. Wang, J. Feng, Y. Chen, X. Yang, S. Gao and R. Cao, *Catal. Sci. Technol.*, 2018, **8**, 1288–1295.

394 S. Liu, F. Chen, S. Li, X. Peng and Y. Xiong, *Appl. Catal., B*, 2017, **211**, 1–10.

395 H. Zhou, P. Li, J. Liu, Z. Chen, L. Liu, D. Dontsova, R. Yan, T. Fan, D. Zhang and J. Ye, *Nano Energy*, 2016, **25**, 128–135.

396 E. Pipelzadeh, V. Rudolph, G. Hanson, C. Noble and L. Wang, *Appl. Catal., B*, 2017, **218**, 672–678.

397 S.-M. Liu, Z. Zhang, X. Li, H. Jia, M. Ren and S. Liu, *Adv. Mater. Interfaces*, 2018, 1801062.

398 N. Sadeghi, S. Sharifnia and T.-O. Do, *J. Mater. Chem. A*, 2018, **6**, 18031–18035.

399 K. Khaletskaya, A. Pougin, R. Medishetty, C. Rösler, C. Wiktor, J. Strunk and R. A. Fischer, *Chem. Mater.*, 2015, **27**, 7248–7257.

400 T. Wang, L. Shi, J. Tang, V. Malgras, S. Asahina, G. Liu, H. Zhang, X. Meng, K. Chang, J. He, O. Terasaki, Y. Yamauchi and J. Ye, *Nanoscale*, 2016, **8**, 6712–6720.

401 S. Wang, B. Y. Guan and X. W. Lou, *J. Am. Chem. Soc.*, 2018, **140**, 5037–5040.

402 Q. Mu, W. Zhu, G. Yan, Y. Lian, Y. Yao, Q. Li, Y. Tian, P. Zhang, Z. Deng and Y. Peng, *J. Mater. Chem. A*, 2018, **6**, 21110–21119.

403 C.-Y. Hu, J. Zhou, C.-Y. Sun, M.-M. Chen, X.-L. Wang and Z.-M. Su, *Chem. – Eur. J.*, 2018, **25**, 379–385.

404 S. Wang, B. Y. Guan, Y. Lu and X. W. Lou, *J. Am. Chem. Soc.*, 2017, **139**, 17305–17308.

405 R. Hinogami, S. Yotsuhashi, M. Deguchi, Y. Zenitani, H. Hashiba and Y. Yamada, *ECS Electrochem. Lett.*, 2012, **1**, H17–H19.

406 R. S. Kumar, S. S. Kumar and M. A. Kulandainathan, *Electrochem. Commun.*, 2012, **25**, 70–73.

407 J. Albo, D. Vallejo, G. Beobide, O. Castillo, P. Castaño and A. Irabien, *ChemSusChem*, 2017, **10**, 1100–1109.

408 M. Perfecto-Irigaray, J. Albo, G. Beobide, O. Castillo, A. Irabien and S. Pérez-Yáñez, *RSC Adv.*, 2018, **8**, 21092–21099.

409 D.-H. Nam, O. S. Bushuyev, J. Li, P. D. Luna, A. Seifitokaldani, C.-T. Dinh, F. P. G. D. Arquer, Y. Wang, Z. Liang, A. H. Proppe, C. S. Tan, P. Todorovic, O. Shekhah, C. M. Gabardo, J. W. Jo, J. Choi, M.-J. Choi, S. Baek, J. Kim, D. Sinton, S. O. Kelley, M. Eddaoudi and E. H. Sargent, *J. Am. Chem. Soc.*, 2018, **140**, 11378–11386.

410 J.-X. Wu, S.-Z. Hou, X.-D. Zhang, M. Xu, H.-F. Yang, P.-S. Cao and Z. Gu, *Chem. Sci.*, 2019, **10**, 2199–2205.

411 X. Kang, Q. Zhu, X. Sun, J. Hu, J. Zhang, Z. Liu and B. Han, *Chem. Sci.*, 2016, **7**, 266–273.

412 X. Jiang, H. Li, J. Xiao, D. Gao, R. Si, F. Yang, Y. Li, G. Wang and X. Bao, *Nano Energy*, 2018, **52**, 345–350.

413 N. Kornienko, Y. Zhao, C. S. Kley, C. Zhu, D. Kim, S. Lin, C. J. Chang, O. M. Yaghi and P. Yang, *J. Am. Chem. Soc.*, 2015, **137**, 14129–14135.

414 L. Ye, J. Liu, Y. Gao, C. Gong, M. Addicoat, T. Heine, C. Wöll and L. Sun, *J. Mater. Chem. A*, 2016, **4**, 15320–15326.

415 I. Hod, M. D. Sampson, P. Deria, C. P. Kubiak, O. K. Farha and J. T. Hupp, *ACS Catal.*, 2015, **5**, 6302–6309.

416 Y.-R. Wang, Q. Huang, C.-T. He, Y. Chen, J. Liu, F.-C. Shen and Y.-Q. Lan, *Nat. Commun.*, 2018, **9**, 4466.

417 Y.-L. Qiu, H.-X. Zhong, T.-T. Zhang, W.-B. Xu, P.-P. Su, X.-F. Li and H.-M. Zhang, *ACS Appl. Mater. Interfaces*, 2018, **10**, 2480–2489.

418 C.-W. Kung, C. O. Audu, A. W. Peters, H. Noh, O. K. Farha and J. T. Hupp, *ACS Energy Lett.*, 2017, **2**, 2394–2401.

419 B.-X. Dong, S.-L. Qian, F.-Y. Bu, Y.-C. Wu, L.-G. Feng, Y.-L. Teng, W.-L. Liu and Z.-W. Li, *ACS Appl. Energy Mater.*, 2018, **1**, 4662–4669.

420 K. Zhao, Y. Liu, X. Quan, S. Chen and H. Yu, *ACS Appl. Mater. Interfaces*, 2017, **9**, 5302–5311.

421 R. Wang, X. Sun, S. Ould-Chikh, D. Osadchii, F. Bai, F. Kapteijn and J. Gascon, *ACS Appl. Mater. Interfaces*, 2018, **10**, 14751–14758.

This journal is © The Royal Society of Chemistry 2019

Chem. Soc. Rev., 2019, **48**, 2783–2828 | 2827

422 X. Wang, Z. Chen, X. Zhao, T. Yao, W. Chen, R. You, C. Zhao, G. Wu, J. Wang, W. Huang, J. Yang, X. Hong, S. Wei, Y. Wu and Y. Li, *Angew. Chem., Int. Ed.*, 2018, **57**, 1944–1948.

423 F. Pan, H. Zhang, K. Liu, D. Cullen, K. More, M. Wang, Z. Feng, G. Wang, G. Wu and Y. Li, *ACS Catal.*, 2018, **8**, 3116–3122.

424 C. Zhao, X. Dai, T. Yao, W. Chen, X. Wang, J. Wang, J. Yang, S. Wei, Y. Wu and Y. Li, *J. Am. Chem. Soc.*, 2017, **139**, 8078–8081.

425 Y. Ye, F. Cai, H. Li, H. Wu, G. Wang, Y. Li, S. Miao, S. Xie, R. Si, J. Wang and X. Bao, *Nano Energy*, 2017, **38**, 281–289.

426 Y. Guo, H. Yang, X. Zhou, K. Liu, C. Zhang, Z. Zhou, C. Wang and W. Lin, *J. Mater. Chem. A*, 2017, **5**, 24867–24873.

427 X. Sun, L. Lu, Q. Zhu, C. Wu, D. Yang, C. Chen and B. Han, *Angew. Chem., Int. Ed.*, 2018, **57**, 2427–2431.

428 J. Kim, S.-N. Kim, H.-G. Jang, G. Seo and W.-S. Ahn, *Appl. Catal., A*, 2013, **453**, 175–180.